THE FORMATION OF ACOUSTICAL FIELDS IN OCEANIC WAVEGUIDES

RECONSTRUCTION OF INHOMOGENEITIES IN SHALLOW WATER

In two volumes

Volume 1

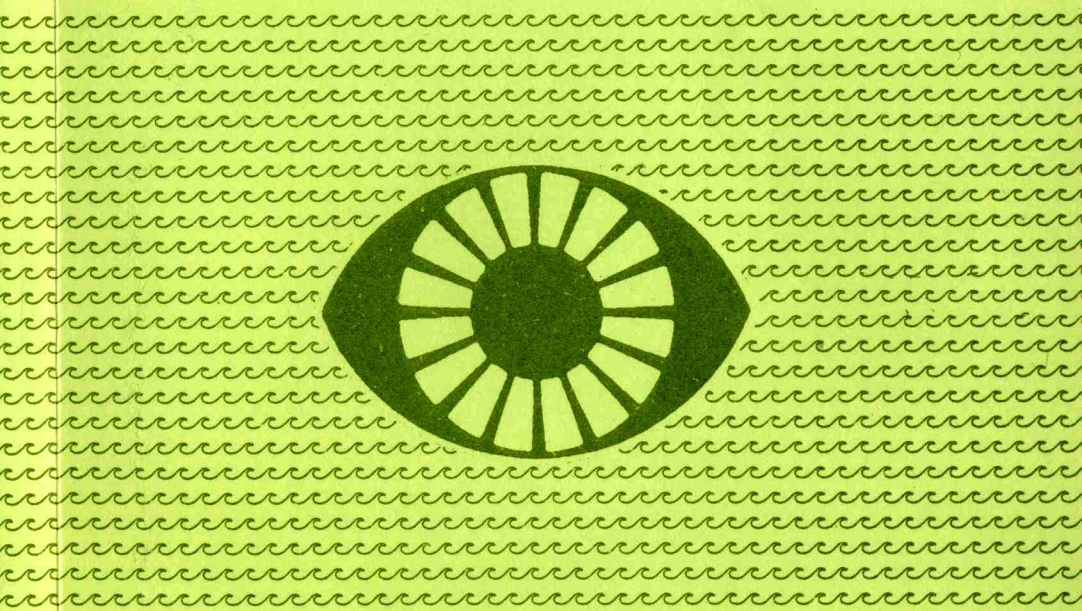

Nizhny Novgorod • 1998

Published on the decision of the Editorial-Board of IAP RAS

The Formation of Acoustical Fields in Oceanic Waveguides. Reconstruction of Inhomogeneities in Shallow Water. Nihzny Novgorod: IAP RAS, 1998. In two volumes. V. 1. 184 p.

State-of-the-art investigations in the field of acoustical probing of different types (including spatially-localized) of oceanic inhomogeneities in shallow water waveguides are presented in this book. The problems associated with reconstruction of parameters of inhomogeneities (bodies or randomly distributed perturbations) in refractive oceanic waveguides in the presence of additive noise reverberation are studied. The optimal tomographical algorithms are discussed for observation of inhomogeneities in shallow water region. Most of investigations are based on analysis of the experimental data. The book can be interesting for researchers and students engaged in the field of hydroacoustics and acoustics of ocean.

Reviewers

Yu.V. Petukhov,
A. I. Saichev

Editor

V. A. Zverev

Co-editor

A. I. Khil'ko

Editorial Group

N. N. Kralina,
V. G. Burdukovskaia

ISBN 5-201-09313-2

CONTENTS

Volume 1

Volume 2

PREFACE

Investigations of the features of synthesis and analysis of hydroacoustical signals, on the one hand, associated with the influence of oceanic waveguide properties, and, on the other hand, taking into account the possibilities of optimization of methods of inhomogeneity characteristics reconstruction are presented in the series of collections in set (from 1991 to 1997 years) of IAP RAS books. The most of investigations in these books were focused on development of fundamnetal researches which can be the scientific base for development of effective schemes of acoustical observation of an oceanic environment condition.

The results of investigations presented in this book can be seen, as some intermediate finish of such investigations, which can show not only additive new understanding of the different details of forming of acoustical fields in oceanic environment, but also to present some of directions for solution of practical problems. In particular, there are the problems of tomographical reconstruction of parameters of spatially-localized inhomogeneities, such as clouds of bubbles and bodies, reconstruction of extruction of characteristics of spatially distributed inhomogeneities of oceanic environment. Another close problem is associated with the receiving and processing of probing acoustical signals. All articles in this book are directed on practice and are based on analysis of experimental data. Some methods were tested in real conditions.

In conclusion of this short preface, we would like to note that it is not difficult to predict the great future for presented in this book direction of investigations because of the activities in the shelf zones of ocean. The methods of shallow water acoustical tomography is the field of great interest of world scientific hydroacoustical community. The example of such interest are the articles of this book which were associated with international collaboration.

This work was supported in part by Spacial Federal Programme «Integratsiya» and by Scientific School of V.A. Zverev.

Vitaly Zverev,
Alexander Khil'ko

ACOUSTIC COHERENCE EFFECTS ON SIGNAL PROCESSING IN SHALLOW WATER CHANNELS

E. Yu. Gorodetskaya, A. I. Malekhanov, A. G. Sazontov, and N. K. Vdovicheva

Introduction

The problem of acoustic coherence and its effects on spatial and temporal signal processing in underwater sound channels is of a great interest in ocean acoustics, mainly, with application to long-range source detection/estimation systems. Recently, considerable effort has been devoted to this problem for the case of large arrays in deep water environments [1–3]. A distinctive feature of this study was incorporating realistic calculations of the signal mutual coherence function (MCF) of space [4–6] to predict the coherence–induced degradation of the array beampattern and gain for several types of linear and quadratic signal processors, optimal ones included. These theoretical results were summarized in the review article by Gorodetskaya *et al.* [7]. It is natural to develop such a scheme of combined consideration of the acoustic coherence and array signal processing in shallow water environments. One of the particular goals here is to formulate recommendations for effective beamformers in realistic shallow water channels.

The research presented also concerns temporal processing of pulsed signals. The previous study [8, 9] was focused on a conventional matched–signal approach and demonstrated a considerable degradation of its performance induced by the MCF of time and frequency in deep water environments. Here, the problem of our particular interest is not only incorporation of realistic shallow–water models of pulse propagation, but also expanding the study of temporal filters to optimal ones. In this context, a general goal is to realize a similar approach to the study of spatial and temporal signal processors, which is focused on realistic predictions of processor performances in underwater channels.

In this paper, we present our results on shallow water acoustic coherence and its effects on large–array beamforming and temporal pulsed signal processing with emphasis on comparative analysis of optimal and suboptimal techniques. A scheme of our study is, in general, the same as was effectively exploited previously [7]. For calculation of the shallow water acoustic MCF in the framework of the modal approach, we develop the method of the

second moment equations, in which an extra absorption term modeling the bottom effects is included. To analyze the optimal signal processors, spatial and temporal ones included, we use the eigenvalue–eigenvector (eigenfunction) decomposition of the signal covariance matrices (signal MCF). Besides, we simulate more simple and traditional techniques, such as plane–wave beamformer (PWBF) and some of its modifications for array processing, and matched filter for temporal processing. The focus here is to estimate and compare the output SNR gain loss for different processors, that is induced by the long-range coherence degradation at the receiving system input.

The body of this paper is organized as follows. In Sec. 1 we introduce a general model of acoustic coupled–mode propagation (the mode–coupling coefficients are random variables resulting from rough surface scattering). We then formulate the second moment equations for the self- and cross-modal coherence functions by assuming that the subbottom attenuation only results in modal–energy loss. In Sec. 2 we give the general description of array beamforming techniques that we use in numerical simulations, including a short discussion of modal approach to their analysis, and in Sec. 3, the basic formulations for temporal processing of pulsed signals. Next, in Sec. 4 we report illustrative results of numerical simulations to show in detail the coherence–induced effects on the performances of both the vertical and horizontal arrays and temporal filters. Finally, in Sec. 5 we discuss the results obtained and summarize the research.

1. Evaluation of the MCF in shallow water

The MCF is of great importance in understanding statistical behavior of underwater acoustic transmission. Most of the activity in this direction has been concentrated on deep–water environments. In such environments with the bottom at abyssal depth, bottom interaction of the acoustic signals can be ignored, and acoustic propagation conserves energy, i.e., there is no attenuation. The application of the general theory of the wave propagation through random media to a deep–water waveguide has been focused on quantitative calculations of the MCF as a function of time and space, on the behavior of pulse propagation, the coherence of intensity, and the probability density of intensity. In this context, it should be noted that the systematic investigations of the sound propagation in a refractive deep oceanic waveguide containing random inhomogeneities have been carried out in a ray oriented approach. The predictions of acoustic coherence from the ray theory and their comparisons with single-receiver measurements are fairly well summarized in the book by Flatte *et al.* [10]. For low-frequency long-range propagation, the ray theory is not adequate and the wave-theoretical

description like the normal-mode method is more suitable. The use of this approach introduces the effect of sound–speed profile in a direct and systematic way. Applied to deep ocean acoustics, the modal treatment was developed in a series of publications and well documented in our review paper [7].

In coastal environments or on the continental shelf, interaction of acoustic signals with the ocean bottom faces the difficulties that are not encountered in deep–water waveguides [11, 12]. The acoustic attenuation resulting from sediment absorption will lead to the decay of the average wavefield intensity and essentially modify the MCF behavior in comparison with the deep–water situation. Efforts have been undertaken to include the presence of the bottom boundary into the consideration by formulating the theory in terms of acoustic normal modes [13–16]. However, the effects caused by sediment absorption have not been included in most studies (exceptions are the works by Creamer [14, 15] who studied only the behavior of the fist and the second moments of the sound intensity). Moreover, the illustrative examples given in Refs. [13–16] do not describe adequately most shallow–water environments (somewhat nonrealistic assumptions are made to simplify the computations).

In the presence of sediment penetration, the modal energies typically decay at different rates, the phenomenon known as mode stripping. On the other hand, the presence of random scattering results in modal coupling with continuous energy exchange between the modes. This "mixing" of energy leads to essential transformation of the modal spectrum of the registered signal and in a nonabsorbing medium the modal intensity distribution approaches a constant at the asymptotic ranges. Hence, the investigation concerning the effects of the competition between mode stripping and random mode coupling on acoustic coherence is of great importance in understanding fluctuation phenomena in a shallow–water channel where bottom interactions are significant. Since bottom effects radically modify the acoustic transmission, any realistic propagation theory in shallow water environments should include them.

In deep ocean channels it is now generally accepted that the random volume scattering in this case is due to the presence of internal waves. For many regions of the world's oceans the internal wave field is well characterized (both experimentally and theoretically) as a stationary, stochastic field, with little geographic variability and the space–time scales of these waves are accurately described by the Garrett–Munk model [17, 18]. This is not correct for most coastal areas and shallow–water regions — the spectrum is not correct while stochastic internal waves are intermittent as a rule.

In the present study we are interested in acoustic coherence in a shallow water environment in which fluctuation phenomena are caused predominantly by fully developed wind seas.

1.1. Formulation of the propagation model

The propagation geometry is exhibited in Fig. 1, where the coordinate system is placed with the z-axis pointing downwards and the x-axis parallel to the boundaries.

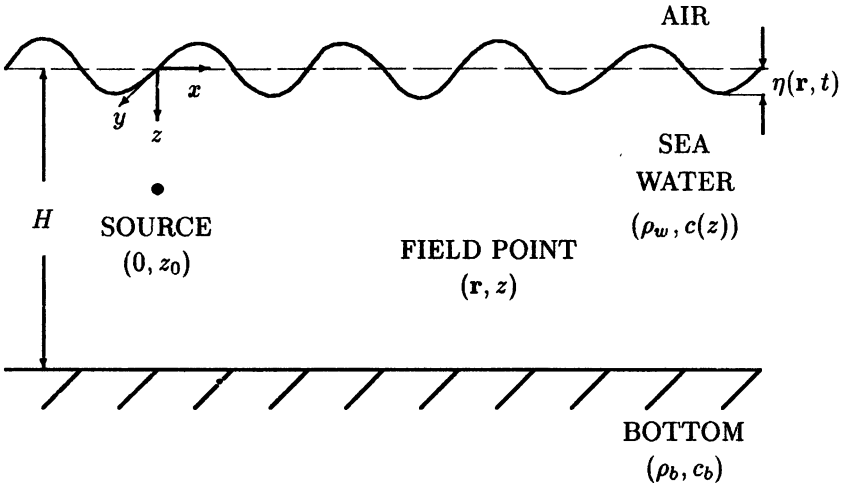

Fig. 1. The geometry of the problem (not shown to scale) presenting shallow–water channel of depth H containing source, field point, and coordinate system

Throughout the paper, the water depth H is assumed to be constant and the background speed of sound $c(z)$ in the fluid is a function of depth z only. The bottom is modelled as a lossy infinite half-space.

Assume that the sound scattering is caused mainly by the statistically rough and acoustically soft boundary $z = \eta(\mathbf{r}, t)$. Here, $\mathbf{r} = (x, y)$ is the horizontal two–dimensional position vector, z is the vertical coordinate, and t is the time. The perturbation η is assumed to be a random Gaussian homogeneous and stationary field with zero mean and can be fully described by its autocorrelation function B_η:

$$B_\eta(\rho, \tau) = <\eta(\mathbf{r}, t)\, \eta(\mathbf{r} + \rho, t + \tau)> .$$

The angular brackets $< \cdots >$ indicate ensemble averaging.

Let a nondirectional acoustic source be located at coordinates $(0, z_0)$ and emit a signal having time dependence $g(t) = s(t)\exp(-i\omega_0 t)$, where $\omega_0 = 2\pi f_0$ denotes the radian carrier frequency, and $s(t)$ specifies the amplitude modulation. This signal passed through a medium with randomly distributed rough surface is registered by the receiver located at coordinates $(\mathbf{r}, z)$. In the subsequent analysis we shall assume that the scale of oceanic inhomogeneities is much greater than acoustic wavelength, the Rayleigh roughness parameter is small, and the characteristic frequencies of B_η are small compared with carrier frequency ω_0.

The complex envelope of the acoustic pressure field $P(\mathbf{r}, z, t)$ in an irregular oceanic channel can be formally represented by

$$P(\mathbf{r}, z, t) = \int_{-\infty}^{\infty} d\omega\, g(\omega)\, e^{-i\omega t}\, P(\mathbf{r}, z, \omega, t). \tag{1}$$

Here, $g(\omega)$ is the frequency spectrum of the transmitted signal and $P(\mathbf{r}, z, \omega, t)$ is the wavefield at angular frequency ω.

The governing equation for the propagation of sound in a channel is

$$\left(\frac{\partial^2}{\partial x^2} + \frac{\partial^2}{\partial y^2} + \frac{\partial^2}{\partial z^2} + k^2 n^2(z)\right) P(\mathbf{r}, z, \omega, t) = 0, \tag{2}$$

where $k = \omega/c_0$, c_0 is chosen to be the minimum of $c(z)$, and $n(z)$ is the refractive index:

$$n(z) = \begin{cases} n_0(z), & 0 \leqslant z \leqslant H; \\ n_\infty\,[1 + i\alpha], & z > H. \end{cases}$$

Here, $n_0(z) = c_0/c(z)$, $n_\infty = c_0/c_b$, c_b is the constant speed of sound in bottom sediment, and α is a measure of the attenuation in the bottom. According to measurements [19] of the acoustic attenuation in different types of sedimentary material, including various sand–silt–clay mixes, the coefficient α is approximately independent of frequency, taking a value in the range 3×10^{-3} to 6×10^{-2}.

In the presence of a soft boundary $z = \eta(\mathbf{r}, t)$, in addition to the wave equation (2), the following condition on the acoustic pressure field is imposed

$$P(\mathbf{r}, \eta(\mathbf{r}, t), \omega, t) = 0. \tag{3}$$

The sound field in the channel obeys also the conditions that the pressure and the normal component of velocity are continuous across the channel

bottom boundary:

$$P(\mathbf{r},z,\omega,t)|_{z=H-0} = P(\mathbf{r},z,\omega,t)|_{z=H+0},$$
$$\frac{1}{\rho_w}\frac{\partial P(\mathbf{r},z,\omega,t)}{\partial z}\bigg|_{z=H-0} = \frac{1}{\rho_b}\frac{\partial P(\mathbf{r},z,\omega,t)}{\partial z}\bigg|_{z=H+0}, \tag{4}$$
$$P(\mathbf{r},z,\omega,t) \to 0 \quad \text{at } z \to \infty,$$

where ρ_w and ρ_b are the density of sea water and the density of bottom sediment, respectively. Equations (2)–(4) define the boundary value problem for the acoustic pressure field.

1.2. Parabolic stochastic coupled mode equations

By applying Green's theorem, the wave equation (2) can be transformed into a boundary integral equation as follows:

$$P(\mathbf{R},\omega,t) = \iint_S \left[P(\mathbf{R}'_s,\omega,t)\frac{\partial G(\mathbf{R},\mathbf{R}'_s)}{\partial n_s} - G(\mathbf{R},\mathbf{R}'_s)\frac{\partial P(\mathbf{R}'_s,\omega,t)}{\partial n_s}\right] dA_s, \tag{5}$$

where $\mathbf{R} = (\mathbf{r},z)$, dA_s is the area element, S is the bounding surface, $\mathbf{n}_s$ is the local outward normal to S, and $G(\mathbf{R},\mathbf{R}')$ is the medium Green's function.

Since the solution has the form of outgoing waves and environment is assumed to be attenuating, as the bounding surface goes to infinity, the integration reduces to integrals on the ocean surface.

For a small Rayleigh parameter, the explicit boundary condition (3) can be expanded at the mean ocean surface $z = 0$ in powers of η to give

$$P(\mathbf{r},0,\omega,t) = -\eta(\mathbf{r},t)\left.\frac{\partial P(\mathbf{r},z,\omega,t)}{\partial z}\right|_{z=0}. \tag{6}$$

The modal solution for $P(\mathbf{r},z,\omega,t)$ in the random oceanic channel far enough from the source can be formally represented by

$$P(\mathbf{r},z,\omega,t) = \sum_{n=1}^{M(\omega)} P_n(\mathbf{r},\omega,t)\,\varphi_n(z,\omega). \tag{7}$$

Here, $\varphi_n(z,\omega)$ denotes the n-th vertical eigenfunction of the deterministic background medium and M is the number of propagation modes. Each

normal mode is modulated by a random amplitude $P_n(\mathbf{r},\omega,t)$ indicating the effect of the surface on acoustic propagation. The normal mode depth functions $\varphi_n(z,\omega)$ satisfy the eigenvalue problem

$$\frac{d^2}{dz^2}\varphi_n(z,\omega) + \left[k^2 n_0^2(z) - \kappa_n^2(\omega)\right]\varphi_n(z,\omega) = 0, \quad n = 1,2,\ldots,M(\omega), \quad (8)$$

together with an orthonormality relation and appropriate boundary conditions

$$\varphi_n(z,\omega)|_{z=H-0} = \varphi_n(z,\omega)|_{z=H+0},$$

$$\frac{1}{\rho_w}\frac{\partial\varphi_n(z,\omega)}{\partial z}\bigg|_{z=H-0} = \frac{1}{\rho_b}\frac{\partial\varphi_n(z,\omega)}{\partial z}\bigg|_{z=H+0},$$

$$\varphi_n(0,\omega) = 0, \quad \varphi_n(z,\omega) \to 0 \quad \text{at } z \to \infty.$$

The eigenvalue corresponding to the n-th modal function is designated by $\kappa_n^2(\omega)$.

The medium Green's function which satisfies the inhomogeneous wave equation and the boundary conditions for the unperturbed (flat pressure release surface) system is [20]:

$$G(\mathbf{R},\mathbf{R}') = -\frac{i}{4}\sum_{m=1}^{M(\omega)}\varphi_m(z,\omega)\varphi_m(z',\omega)\,H_0^{(1)}(\kappa_m(\omega)\,|\mathbf{r}-\mathbf{r}'|), \quad (9)$$

where $H_0^{(1)}$ is the cylindrical Hankel function of the first kind of order 0. Since G evaluated at $z = 0$ vanishes, the integral of Eq. (5) can be rewritten as

$$P(\mathbf{R},\omega,t) = \iint_{z=0} P(\mathbf{R}_s',\omega,t)\,\frac{\partial G(\mathbf{R},\mathbf{R}_s')}{\partial n_s}\,dA_s. \quad (10)$$

The combination of Eqs. (6), (7), and (9) with Eq. (10) yields:

$$P_n(\mathbf{r},\omega,t) = \frac{i}{4}\iint_{z=0}\eta(\mathbf{r}_s',t)\sum_{m=1}^{M(\omega)}P_m(\mathbf{r}_s',\omega,t)H_0^{(1)}(\kappa_n(\omega)\,|\mathbf{r}-\mathbf{r}_s'|)\times \quad (11)$$

$$\times\varphi_n'(0,\omega)\varphi_m'(0,\omega)\,dA_s,$$

where the prime denotes differentiation with respect to depth z. In obtaining (11) the modal orthonormality has been exploited. By applying the

operator $\left(\frac{\partial^2}{\partial x^2}+\frac{\partial^2}{\partial y^2}+\kappa_n^2(\omega)\right)$ to both sides of Eq. (11) and making use of the fact that

$$\left(\frac{\partial^2}{\partial x^2}+\frac{\partial^2}{\partial y^2}+\kappa_n^2(\omega)\right) H_0^{(1)}(\kappa_n(\omega)\,|\mathbf{r}-\mathbf{r}'|) = 4i\delta(\mathbf{r}-\mathbf{r}'),$$

one obtains the following set of coupled mode equations:

$$\left(\frac{\partial^2}{\partial x^2}+\frac{\partial^2}{\partial y^2}+\kappa_n^2(\omega)\right) P_n(\mathbf{r},\omega,t) = -\sum_{m=1}^{M(\omega)} \eta_{nm}(\mathbf{r},\omega,t) P_m(\mathbf{r},\omega,t), \quad (12)$$

where

$$\eta_{nm}(\mathbf{r},\omega,t) = \varphi_n'(0,\omega)\varphi_m'(0,\omega)\,\eta(\mathbf{r},t).$$

In what follows, where the forward scattering is assumed to be essential, we shall use the spatial coordinate system with the x-axis taken in the main direction of wave propagation.

For forward propagation, letting

$$P_n(\mathbf{r},\omega,t) = \frac{1}{\sqrt{\kappa_n(\omega)}}\, p_n(\mathbf{r},\omega,t)$$

one obtains from Eq. (12) the parabolic coupled mode equations for the modal coefficients $p_n(\mathbf{r},\omega,t)$:

$$\left(\frac{\partial}{\partial x} - i\kappa_n(\omega) - \frac{i}{2\kappa_n(\omega)}\frac{\partial^2}{\partial y^2}\right) p_n(\mathbf{r},\omega,t) = i\sum_{m=1}^{M(\omega)} V_{nm}(\mathbf{r},\omega,t)\, p_m(\mathbf{r},\omega,t), \quad (13)$$

where the complex horizontal wavenumber is

$$\kappa_n(\omega) = æ_n(\omega) + i\alpha_n(\omega),$$

with the ordinary acoustic wavenumber $æ_n(\omega)$ and $\alpha_n(\omega)$ the modal attenuation parameter, given by (see, e.g. [12]):

$$\alpha_n(\omega) = \frac{\rho_w}{\rho_b}\,\frac{k^2 n_\infty^2 |\varphi_n(H,\omega)|^2}{2æ_n(\omega)\sqrt{æ_n^2(\omega)-k^2n_\infty^2}}\,\alpha. \quad (14)$$

The mode–coupling term is

$$V_{nm}(\mathbf{r},\omega,t) = \frac{\eta_{nm}(\mathbf{r},\omega,t)}{2\sqrt{\kappa_n(\omega)\kappa_m(\omega)}} \equiv \frac{\varphi_n'(0,\omega)\varphi_m'(0,\omega)}{2\sqrt{\kappa_n(\omega)\kappa_m(\omega)}}\,\eta(\mathbf{r},t). \quad (15)$$

The quantity V_{nm} that is similar in form to Eq. (15) was derived by Bass and Fuks [21]. Equation (13) is the starting equation for the subsequent statistical analysis.

1.3. Second moment equations for the multimodal MCF

The quantity of ultimate interest is the second moment of the complex pressure:

$$B_p(\mathbf{r_1}, z_1, t_1|\mathbf{r_2}, z_2, t_2) = < P(\mathbf{r_1}, z_1, t_1)\, P^*(\mathbf{r_2}, z_2, t_2) > . \qquad (16)$$

Substituting Eqs. (1), (7) into Eq. (16), one finds that

$$B_p(\mathbf{r_1}, z_1, t_1|\mathbf{r_2}, z_2, t_2) = \int_{-\infty}^{\infty} d\omega_1 \int_{-\infty}^{\infty} d\omega_2\, g(\omega_1) g^*(\omega_2) \Gamma(\cdot|\cdot) e^{-i\omega_1 t_1 + i\omega_2 t_2}, \qquad (17)$$

where $\Gamma(\mathbf{r_1}, z_1, \omega_1, t_1|\mathbf{r_2}, z_2, \omega_2, t_2)$ is the total MCF defined as

$$\Gamma(\mathbf{r_1}, z_1, \omega_1, t_1|\mathbf{r_2}, z_2, \omega_2, t_2) = \sum_{n,m} \frac{\varphi_n(z_1, \omega_1)\varphi_m(z_2, \omega_2)}{\sqrt{\varkappa_n(\omega_1)\varkappa_m(\omega_2)}}\, \Gamma_{nm}(1,2); \qquad (18)$$

$$\Gamma_{nm}(1,2) = < p_n(1)\, p_m^*(2) > .$$

The labels 1 and 2 refer to two different horizontal position points, times and frequencies. In Eq. (18) we see that the total MCF is expressed as the weighted sum of the self-modal coherences $\Gamma_{nn}(1,2)$ and cross-modal coherences $\Gamma_{nm}(1,2)$ $(n \neq m)$. Thus, the problem of finding a result for B_p in an irregular oceanic waveguide channel now reduces to evaluating the self-modal and cross-modal coherence functions.

The equations governing the change of $\Gamma_{nm}(1,2)$ as a result of random surface scattering can be derived from (13) under the Markov approximation (see, e.g., [7] and the corresponding references presented there). A considerable simplification occurs for the waveguides having a nonequidistant spectrum of wavenumbers $æ_n$ [22]. In this case, the diagonal elements of the matrix $\Gamma_{nm}(1,2)$ decouple from the off-diagonal elements. As a consequence, for $\Gamma_{nn}(1,2)$ the final equation is

$$\left[\frac{\partial}{\partial x} - i\left(æ_n(\omega_1) - æ_n(\omega_2)\right) - \frac{i}{2}\left(\frac{1}{æ_n(\omega_1)}\frac{\partial^2}{\partial y_1^2} - \frac{1}{æ_n(\omega_2)}\frac{\partial^2}{\partial y_2^2}\right)\right]\Gamma_{nn}(1,2) =$$
$$= -\frac{1}{2}\left[\sigma_n(\omega_1) + \sigma_n(\omega_2)\right]\Gamma_{nn}(1,2) + \sum_m A_{nm}^{nm}(1,2)\,\Gamma_{mm}(1,2). \qquad (19)$$

Here, $\sigma_n(\omega)$ is the total modal attenuating parameter

$$\sigma_n(\omega) = \sigma_n^a(\omega) + \sigma_n^s(\omega),$$

where $\sigma_n^a(\omega)$ is the absorption coefficient: $\sigma_n^a(\omega) = 2\alpha_n(\omega)$ with $\alpha_n(\omega)$ specified in Eq. (14), and $\sigma_n^s(\omega)$ is the scattering coefficient:

$$\sigma_n^s(1) = \sum_{m=1}^{M} A_{nm}^{nm}(1,1).$$

The coupling matrix $A_{nm}^{nm}(1,2)$ is given by the expression

$$A_{nm}^{nm}(1,2) = \frac{\pi}{2} \frac{\left[\varphi_n'(0,\omega_1)\varphi_m'(0,\omega_1)\varphi_n'(0,\omega_2)\varphi_m'(0,\omega_2)\right]}{\left[æ_n(\omega_1)æ_m(\omega_1)æ_n(\omega_2)æ_m(\omega_2)\right]^{1/2}} \times$$

$$\times \int_{-\infty}^{\infty} d\Omega\, e^{-i\Omega\tau} \int_{-\infty}^{\infty} dæ_y\, e^{iæ_y\rho}\, F_\eta(æ_{nn}^+ - æ_{mm}^+, æ_y, \Omega),$$

where $F_\eta(æ, \Omega)$ is the Fourier transform of the surface autocorrelation with respect to ρ and τ and $æ_{nn}^+ = 0.5\,(æ_n(\omega_1) + æ_n(\omega_2))$.

At $\omega_1 = \omega_2$, an equation similar to Eq. (19), but without transverse y dependence and subbottom attenuation, was derived by Beilis and Tappert [23] using a parabolic approximation.

The equation for the cross–modes is

$$\left[\frac{\partial}{\partial x} - i\,(æ_n(\omega_1) - æ_m(\omega_2)) - \frac{i}{2}\left(\frac{1}{æ_n(\omega_1)}\frac{\partial^2}{\partial y_1^2} - \frac{1}{æ_m(\omega_2)}\frac{\partial^2}{\partial y_2^2}\right)\right]\Gamma_{nm}(1,2) =$$

$$= \left[-\frac{1}{2}\left(\sigma_n(\omega_1) + \sigma_m(\omega_2)\right) + A_{nn}^{mm}(1,2)\right]\Gamma_{nm}(1,2), \tag{20}$$

where

$$A_{nn}^{mm}(1,2) = \frac{\pi\left[\varphi_n'(0,\omega_1)\varphi_m'(0,\omega_2)\right]^2}{2\kappa_n(\omega_1)\kappa_m(\omega_2)} \int_{-\infty}^{\infty} d\Omega e^{-i\Omega\tau} \int_{-\infty}^{\infty} dæ_y\, e^{iæ_y\rho} F_\eta(0, æ_y, \Omega).$$

As a consequence of (20), we obtain the following representation [9]:

$$\Gamma_{nm}(1,2) = <p_n(1)><p_m^*(2)>\, T_{nm}(1,2), \quad n \neq m, \tag{21}$$

where

$$<\mathrm{p}_n(\mathbf{r},\omega,t)> = \frac{-i\varphi_n(z_0,\omega)}{\sqrt{8\pi x}} \exp\left[\left(iæ_n(\omega) - \frac{1}{2}\dot{\sigma}_n(\omega)\right)|\mathbf{r}| - i\frac{\pi}{4}\right] \tag{22}$$

is the coherent field of the n-th mode and the explicit expression for T_{nm} is given in Ref. [9].

For most oceanic applications the characteristic correlation length l_η of surface irregularities is much less than the typical mode cycle distance, i.e., $l_\eta \ll \Lambda_n$. In this case, elementary acts of scattering occur at statistically independent ensembles of the surface, and the formula (21) reduces to a simpler form [24]:

$$\Gamma_{nm}(1,2) = <p_n(1)><p_m^*(2)>, \quad n \neq m.$$

Thus, under the assumption made, the second moment of the modal coefficients $\Gamma_{nm}(1,2)$ appearing in Eq. (18) becomes

$$\Gamma_{nm}(1,2) = <p_n(1)><p_m^*(2)> + [\Gamma_{nn}(1,2) - <p_n(1)><p_n^*(2)>]\delta_{nm}. \tag{23}$$

The relations (18) and (23) together with Eqs. (19), (22) allow for estimation of the key correlation characteristics of the acoustic signal in a shallow water channel where the rough surface scattering effects are important.

2. Array beamforming techniques

In this section, we consider array signal processing of the Fourier–transformed sensor data at an arbitrary frequency. The main attempts are focused on the case of coherence–degraded signal, which was shown to be the inherent case of shallow water sound propagation as the result of multiple sound scattering on random wind waves. Our particular interest concerns the array gain defined directly from the small–signal deflection, or the generalized SNR, for several types of linear and quadratic beamformers, and a multimode model for the discrete spectrum signals.

2.1. Array gain

We follow here the general formulations for the array signal processors exploited in the previous study [1, 3, 7].

Assume that the acoustic signals at an N–element array are N–dimensional data vectors, the signal of interest (vector s) and the noise background (vector n) are both zero–mean and mutually uncorrelated random processes, and the noise vector is a Gaussian process. The spatial covariance matrices are defined as $\mathbf{\Gamma}_x = <\mathbf{x}\mathbf{x}^+>$ ($\mathbf{x} = \mathbf{s}$ or $\mathbf{n}$, respectively; the superscript $^+$ denotes complex conjugate transpose). The signal matrix $\mathbf{\Gamma}_s$ is obtained from the calculations of the MCF of space for a given set of source and environmental parameters, and the noise matrix $\mathbf{\Gamma}_n$ is calculated directly by using the well–known model of surface–generated modal noise [25].

The array gain G is defined as the output SNR q normalized to the input SNR q_0:

$$G = \frac{q}{q_0}, \qquad q_0 = \frac{\mathrm{Tr}(\mathbf{\Gamma}_s)}{\mathrm{Tr}(\mathbf{\Gamma}_n)}, \tag{24}$$

where the symbol $\mathrm{Tr}(\cdot)$ denotes the matrix trace. For the output SNR we use the deflection which is given by

$$q = \frac{<d(\mathbf{s}+\mathbf{n})> - <d(\mathbf{n})>}{\{<d^2(\mathbf{n})> - <d(\mathbf{n})>^2\}^{1/2}}, \tag{25}$$

where $d(\cdot)$ is the detection statistic [26–28].

2.2. Linear beamformers

According to the general definition, we refer to a linear beamformer (LBF) as to a device which weights the outputs of each array element and then sums the weighted outputs. This is a conventional choice for array signal processing with numerous applications in radar and sonar [29, 30]. The general structure of LBF (a weight–sum–square scheme) is shown in Fig. 2.

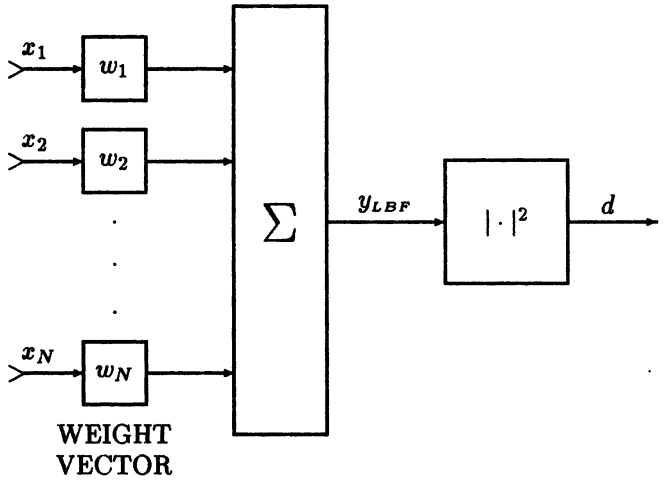

Fig. 2. The general structure of linear beamformer

The LBF output y_{LBF} is obtained as a *linear* function of the input vector $\mathbf{x}$, and the detection statistic d as a squared y_{LBF}:

$$y_{LBF} = \mathbf{w}^T\mathbf{x}, \qquad d = \left|\mathbf{w}^T\mathbf{x}\right|^2, \tag{26}$$

where the superscript ^{T} denotes the operation of vector transposition.

The vector $\mathbf{w}$ is an arbitrary $(N \times 1)$ weight vector of the array elements, the choice of which gives the output array performances.

The output SNR q_{LBF} is given by the ratio of the corresponding quadratic forms:

$$q_{LBF} = \frac{\mathbf{w}^T \mathbf{\Gamma}_s \mathbf{w}^*}{\mathbf{w}^T \mathbf{\Gamma}_n \mathbf{w}^*}. \tag{27}$$

In this paper, we compare the SNR gain performance for the same three LBFs which were compared in detail in deep water environments [7].

Plane-wave beamformer

The first one is a conventional PWBF given by

$$w_{PW}(j) = \exp[-ikd(j-1)\sin\beta], \quad j = 1, 2, \ldots, N, \tag{28}$$

where β is an arbitrary steering angle.

Adaptive plane-wave beamformer

The second one is a plane-wave beamformer with noise interference prewhitening, or adaptive PWBF (APW) [29, 30]. Its weight vector $\mathbf{w}_{APW}$ is given by

$$\mathbf{w}_{APW} = \mathbf{\Gamma}_n^{-1} \mathbf{w}_{PW}. \tag{29}$$

Optimal linear beamformer

The third one is an optimal LBF which is of particular interest in the case of partially coherent signal. Its weight vector $\mathbf{w}_{LBF}$ is given by the following eigenvalue–eigenvector problem:

$$q_p \mathbf{v}_p = \mathbf{\Gamma}_n^{-1} \mathbf{\Gamma}_s \mathbf{v}_p, \qquad p = 1, 2, \ldots, r = \operatorname{rank}(\mathbf{\Gamma}_s), \tag{30}$$

where the eigenvalues q_p are assumed to be ordered as

$$q_1 \geqslant q_2 \geqslant \ldots q_r > 0.$$

The largest eigenvalue q_1 is the maximum SNR among all LBFs, and the corresponding eigenvector $\mathbf{v}_1$ is the optimal weight vector: $q_{LBF} = q_1$, $\mathbf{w}_{LBF}^* = \mathbf{v}_1$.

2.3. Quadratic beamformers

In comparison with LBF, a more complicated quadratic beamformer (QBF) is a weight–square–sum scheme consisting of a matrix filter $\mathbf{W}$ followed by an R–channel quadratic processor [26, 27, 30]. The general structure of QBF is shown in Fig. 3.

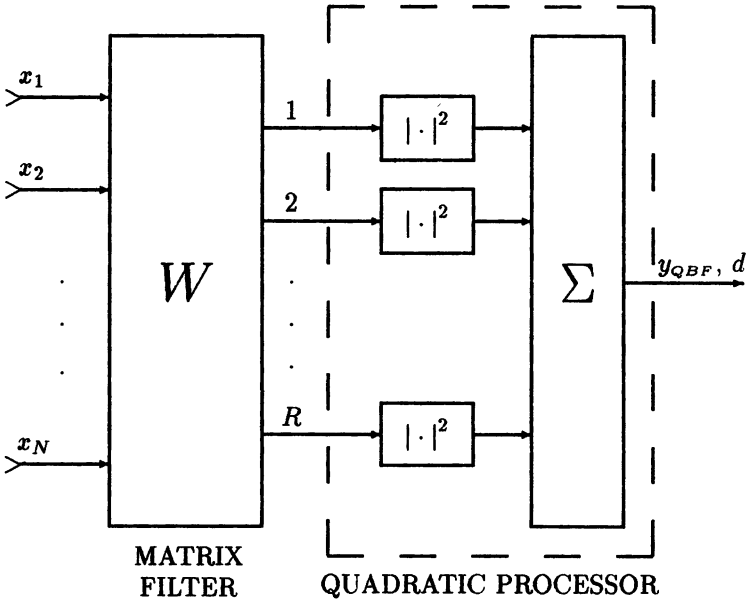

Fig. 3. The general structure of quadratic beamformer

The QBF output y_{QBF} is obtained as a *quadratic* function of the input vector $\mathbf{x}$ in the form

$$y_{QBF} = \mathbf{x}^T \mathbf{A} \mathbf{x}^* = |\mathbf{W}^T \mathbf{x}|^2. \tag{31}$$

Here, the matrix $\mathbf{A}$ is an arbitrary Hermitian $(N \times N)$ processing matrix factorized as $\mathbf{A} = \mathbf{W}^* \mathbf{W}^T$ by using an $(N \times R)$ weight matrix $\mathbf{W}$ $(1 \leqslant R \leqslant N)$.

The output SNR q_{QBF} is given by the following ratio:

$$q_{QBF} = \frac{\mathrm{Tr}\,(\mathbf{W}^* \mathbf{W}^T \mathbf{\Gamma}_s)}{[\mathrm{Tr}(\mathbf{W}^* \mathbf{W}^T \mathbf{\Gamma}_n)^2]^{1/2}}. \tag{32}$$

As is clearly seen from Figs. 2, 3 and directly follows from Eqs. (26), (31), the QBF scheme is a squared combination of R partial LBFs which are characterized by the corresponding weight row-vectors $\mathbf{w}_p$ $(p = 1, 2, \ldots, R)$. This scheme allows, generally, for both coherent and incoherent signal processing. Note that QBF reduces to LBF in the specific case of $R = 1$.

Similarly to the LBF scheme, the choice of the weight matrix $\mathbf{W}$ and, respectively, the matrix $\mathbf{A}$ of QBF determines the output array performance for given signal and noise inputs. One of attractive strategies is to optimally process the partially coherent (random) signal against the noise background and to maximize the array SNR and gain. In practical situations, however, this strategy can require a considerable increase in the processor complexity, consequently, the suboptimal schemes are of particular interest.

In this paper, we compare the SNR gain performance for three QBFs. The first of them is the optimal QBF which maximizes the output SNR (25) and realizes the upper limit of the array gain [26–28], and the other two are suboptimal beamformers.

Optimal quadratic beamformer

The optimal QBF which maximizes the output SNR (25) and realizes the upper limit of the array gain, namely in the case of partially coherent signal, is given by

$$\mathbf{A}_{opt} = \mathbf{\Gamma}_n^{-1}\mathbf{\Gamma}_s\mathbf{\Gamma}_n^{-1}, \qquad \mathbf{w}_p^* = \lambda_p^{1/2}\mathbf{\Gamma}_n^{-1}\mathbf{m}_p. \tag{33}$$

Here, λ_p and $\mathbf{m}_p$ are the eigenvalues and eigenvectors of the signal matrix $\mathbf{\Gamma}_s$, respectively, which are given by

$$\lambda_p\mathbf{m}_p = \mathbf{\Gamma}_s\mathbf{m}_p, \qquad p = 1, 2, \ldots, r = \operatorname{rank}(\mathbf{\Gamma}_s). \tag{34}$$

The eigenvalues λ_p are assumed to be ordered and normalized by

$$\lambda_1 \geqslant \lambda_2 \geqslant \ldots \lambda_r > 0, \qquad \sum_{p=1}^{N}\lambda_p = 1. \tag{35}$$

The maximum SNR results from direct substitution of Eq. (33) into Eq. (32) and is given by

$$q_{QBF} = \left[\operatorname{Tr}\left(\mathbf{\Gamma}_n^{-1}\mathbf{\Gamma}_s\right)^2\right]^{1/2} = \left\{\sum_{p=1}^{r} q_p^2\right\}^{1/2}, \tag{36}$$

where q_p are the eigenvalues from Eq. (30).

As follows from these equations, the number R of partial linear channels in the full–optimal QBF is equal to the signal rank, $R = r$. Because the rank r increases monotonically with the ratio of the array length N to the signal coherence length N_c, the performance/complexity of optimal beamformer is a function of this key parameter. As is clearly seen from Eq. (36), only the largest eigenvalues q_p are of real importance for calculation of the quadratic array gain. In turn, their number is upper limited by an "effective" signal rank r_{eff} which is defined as a number of the largest signal eigenvalues λ_p (35).

Subarray beamformer

One of practical approaches to large–array processing of partially coherent signals (for the $N/N_c \gtrsim 2$ ratio) is based on an heuristic idea of incoherent combining the outputs of a number of subarray LBFs, the lengths of which are about N_c. This scheme is not a full–optimal choice, but does have two essential features. First, the computational requirements are much lower; second, the details of the signal coherence need not to be known precisely, implying robustness of the processor to the coherence variations in nonstationary conditions.

Formally, the subarray approach can be described by the general equations (31), (32) with a block–diagonal weight matrix

$$\mathbf{W}_{SA} = \mathrm{diag}\,(\mathbf{w}_1, \mathbf{w}_2, \ldots \mathbf{w}_R)\,, \tag{37}$$

where each subarray weight vector $\mathbf{w}_p$, $p = 1, 2, \ldots, R$, is formed as for a conventional PWBF (28) (in the case of white noise) or adaptive PWBF (29) (in the case of ambient modal noise). For example, the simplest first case is

$$w_p(j) = \exp\left[-ikd(j-1)\sin\beta_p\right], \qquad (p-1)N_{SA} + 1 \leqslant j \leqslant pN_{SA}, \tag{38}$$

and $w_p(j) = 0$ for all the other element numbers j. Generally, the steering angles β_p can be chosen to be different for each subarray to match this scheme to multipath propagation. A special case $R = 1$ leads to the simplest PWBF (28).

The subarray beamformer (SABF) was previously analyzed by several authors with the focus on the coherence degradation [26, 28] and the multipath signal reception [31]. An important issue here is, however, the case of partial signal coherence characterized by residual spatial correlations across a large array. We emphasize in this connection, that this case is a typical practice for horizontal and vertical arrays in underwater channels (both deep–water and shallow–water ones).

Incoherent modal beamformer

Another approach to suboptimal array beamforming, which is motivated directly by multimode/multipath propagation of the signal and ambient noise fields in underwater channels, is incoherent mode filtering [32].

Generally, this technique exploits the same heuristic idea of squared combination of the partial filter outputs (as for SABF), but each partial filter is formed to be matched to some normal mode of the signal. Contrary to SABF, the partial weight vectors $\mathbf{w}_p$, $p = 1, 2, \ldots, R$, are expanded at full array length. Following such an approach, the weight matrix $\mathbf{W}_{IMF}$ and weight vectors (its rows) $\mathbf{w}_p$ are easily given by

$$\mathbf{w}_p = \mathbf{u}^*_{m(p)}, \qquad \mathbf{W}_{IMF} = \mathbf{U}^* \operatorname{diag}(\delta_{m,m(p)}), \tag{39}$$

where $\mathbf{u}_m$ are the vectors of modal shapes over the full array, or the modal vectors, with the numbers $m = 1, 2, \ldots, M$; M is the total number of the signal–carrying modes; $\mathbf{U}$ is the $(N \times M)$ matrix consisting of the row–vectors $\mathbf{u}_m$, or the modal matrix (see also the next subsection); the numbers $m(p)$ indicate the "reference" modes which the p–partial filter is matched to; $\delta_{m,m(p)}$ is the Krönecker symbol.

For $R > 1$ this approach leads to quadratic beamforming, and for $R = 1$, to a linear scheme of matched–mode filtering. Taking a general analogy with multibeam phased arrays, we will refer to such a beamformer as to incoherent modal beamformer (IMBF).

2.4. Modal approach to large–array beamforming

As was shown in Refs. [27, 33, 34] on the basis of a general model representing the multimode signal and noise fields with arbitrary amplitude covariances, the array beamforming techniques can be re-formulated in mode space to realize a complete scheme of normal mode treatment of the signal processing problem. The modal approach to examination of the coherence effects on array beamforming is a useful tool that enables us to interpret the results of full–wave simulations from the spatial MCF in the mode space and to propose effective suboptimal beamforming techniques. For a particular case of long-range sound propagation in shallow–water channels, the analysis of beamforming in mode space is quite reasonable because of the intrinsic features of the problem. The first feature is a relatively small number of the discrete spectrum modes. The second one is a specific shallow–water evolution of the signal modal spectrum over long distances due to strong effects of cross–modal interaction and bottom–induced modal stripping.

To analyze the schemes of the multimode signal array processing we use here the array beampattern in mode space, or modal pattern [27], defined

as

$$\mathbf{g} = \mathbf{U}^T \mathbf{w}, \qquad g_m = \sum_{j=1}^{N} u_m(j) w(j). \tag{40}$$

Taking an analogy with conventional beampattern, the modal pattern shows the modes which give the maximum response in the array beamformer output. It is important that the modal pattern may be obtained directly from the M–dimensional matrix equations containing the matrices of the modal covariances (instead of the spatial ones) of the signal and ambient noise and the matrix of the modal orthogonality factors [27, 34, 35].

In this subsection we restrict ourselves only to two short comments concerned with a physical interpretation of optimal beamforming, which is based on modal approach. These comments are important for further discussion of numerical results.

First, for the case of coherent signal in ambient noise, when adaptive PWBF (29) is the optimal processor, its modal pattern $\mathbf{g}_{APW}$ is formed in such a way that the most noised signal–carrying modes are in deep nulls of the pattern [27, 35]. Because the ambient sea noise is usually multimodal and covers some modal band, the corresponding modal bandwidth is cut off in the pattern. This leads to a considerable rejection of the signal, if its spectrum is filled in part by the noised modes.

Second, for the case of decorrelated signal modes, when the optimal QBF (33) should be used to enhance the array gain, the partial modal patterns $\mathbf{g}_p$ are formed to match the partial filters $\mathbf{w}_p$ to the modes of the most intensive signal eigencomponents [33, 34]. In comparison, the modal pattern of the optimal LBF (30) matches one eigencomponent with the maximum intensity. Therefore, if the signal–carrying modes are decorrelated and the array length is sufficient for their spatial resolution (orthogonality), the optimal QBF is a substantially complicated scheme at a cost of forming additional modal filters. Note also that the modal patterns are determined in this case only by the modal orthogonality factors and modal intensities of the signal and ambient noise.

Returning to the IMBF scheme we note that in a general case of multimode signal in multimode noise background, IMBF is essentially different from the optimal QBF. It is clear, however, that IMBF is a suboptimal processor when the signal consists of several uncorrelated and resolvable (orthogonal) modes, and their modal SNRs are similar to each other [32]. An effective choice for the reference modes (for the numbers $m(p)$) is, therefore, the modes with maximum values of modal SNR. The latter values, in turn, depend on the modal spectra of both the signal and ambient noise, so

they may be essentially different for various sound frequencies, signal source depths, and underwater environments.

Thus, the modal approach to array beamforming gives us an effective scheme to select the modes from the point of view of their partial contributions to the array processor performance/complexity.

3. Temporal processing of narrow–band acoustic pulses

Until now, we have discussed the coherence effects on the large–array processor performance in application to CW transmission. In this section, we focus on temporal processing of partially coherent nonstationary radiation, namely, temporal filtering of narrow–band acoustic pulses in a shallow water waveguide, where rough scattering processes are important. This problem is considered to be of a great interest in various applications concerned with underwater detection, communication, and the ocean acoustic tomography.

The starting point in designing a temporal receiver is statistical analysis of the temporal stability of the registered wavefield. In this context it should be noted that the theoretical studies of the temporal pulse structure have been carried out with deep–water application in mind (see, e.g. [10] and the corresponding references presented there). A distinctive feature of the current consideration is incorporating realistic calculations of the quantity of interest to predict the combined effects of random scattering and bottom interactions on the quality of the temporal performance.

Note also that the methods presented in our previous section may be adapted directly to the construction of temporal processors, optimal one included, since the general techniques of signal processing are well known to be similar for spatial and temporal domains.

3.1. Pulse temporal structure and governing equations

The important correlation properties of a pulsed wave, that has traversed a random oceanic waveguide, are described by the second moment of the acoustic pressure field, Eq. (17). In what follows we will be interested in the temporal behavior of the correlation function with no simultaneous space separation.

For a narrow transmitted pulse, when $\omega_d = \omega_1 - \omega_2 \ll \omega_0$, $0.5(\omega_1 + \omega_2) \approx \omega_0$, we can put $\varphi_n(z, \omega_{1,2}) \approx \varphi_n(z, \omega_0)$ and expand $\kappa_n(\omega_{1,2})$ in the Taylor series: $\kappa_n(\omega_{1,2}) = \kappa_n(\omega_0) + 1/v_n\,(\omega_{1,2} - \omega_0) + \cdots$, where v_n

is the group velocity of the n-th mode. Then, the quantity B_p may be simplified and in the case considered Eq. (17) taken at $\mathbf{r}_1 = \mathbf{r}_2 = \mathbf{r}$ and $z_1 = z_2 = z$ is replaced by

$$B_p(t_1, t_2) = B_p^c(t_1, t_2) + B_p^i(t_1, t_2). \tag{41}$$

At this stage, the dependence of B_p on spatial coordinates has been omitted for notational convenience. Here, $B_p^c(t_1, t_2)$ is the coherent part of the temporal correlation function that is determined by the expression

$$B_p^c(t_1, t_2) = \sum_{n,m} \frac{1}{\sqrt{\kappa_n \kappa_m}} < p_n(\mathbf{r}, t_1) > < p_m^*(\mathbf{r}, t_2) > \varphi_n(z)\varphi_m(z), \tag{42}$$

with

$$< p_n(\mathbf{r}, t) >= \frac{1}{\sqrt{8\pi x}} s(t - t_n)\, \varphi_n(z_0)\, e^{\left(i\kappa_n - \frac{1}{2}\sigma_n\right) x},$$

(where we have dropped the argument ω_0 for brevity), and $B_p^i(t_1, t_2)$ is the incoherent component:

$$B_p^i(t_1, t_2) = \sum_{n=1}^{M} \frac{1}{\kappa_n} \Gamma_{nn}^i(x, t_1, t_2)\, \varphi_n^2(z), \tag{43}$$

where

$$\Gamma_{nn}^i(x, t_1, t_2) = \int_{-\infty}^{\infty} d\omega_d \chi(\tau, \omega_d) \Gamma_{nn}(x, \tau, \omega_d) e^{-i\omega_d t} -$$

$$- \frac{\varphi_n^2(z_0)}{8\pi x} s(t_1 - t_n) s^*(t_2 - t_n) e^{-\frac{1}{2}\sigma_n x}.$$

In writing Eqs. (42), (43) we use the following notation: $\tau = t_1 - t_2$, $t = 0.5(t_1 + t_2)$, $t_n = x/v_n$, and

$$\chi(\tau, \omega_d) = \frac{1}{2\pi} \int_{-\infty}^{\infty} dt\, s(t + \frac{1}{2}\tau)\, s^*(t - \frac{1}{2}\tau)\, e^{i\omega_d t}$$

is the ambiguity function of the transmitted pulse. Thus, the estimation of the pulse temporal structure requires the knowledge of the self-modal MCF of time and frequency separations.

Equation (41) together with Eqs. (43), (42) are the main equations in this section.

3.2. Temporal performance analysis

Detailed treatments of the detection problem for partially coherent Gaussian signals against a Gaussian noise background can be found in Ref. [36] as well as elsewhere in the literature. For most practical applications, the registered signal is non–Gaussian due to complicated conditions of ocean sound propagation. For weak signals, however, the performance of the temporal receiver can be evaluated in terms of the deflection ratio for arbitrary signal statistics. Here, we apply such a consideration to shallow water acoustics for the construction of temporal processors, optimal one included.

Assume that a received waveform portion $x(t)$ on the interval of the observation $t \in [T_i, T_f]$ consists of a random background noise $n(t)$ which may or may not include the signal of interest $p(t)$. In what follows, for simplicity we let $n(t)$ be bandlimited white noise, i.e.,:

$$< n(t_1)\, n(t_2) >= \sigma_w\, \delta(t_1 - t_2),$$

with the spectral level equal to σ_w.

By analogy with array signal processing, SNR for the case considered can be associated with the test statistic d by defining the desired output signal as the deflection in the mean value of d caused by the presence of the signal at the receiver input. The SNR is then defined as the deflections ratio (see also Eq. (25)):

$$SNR = \frac{< d(p+n) > - < d(n) >}{\{< d^2(n) > - < d(n) >^2\}^{1/2}}. \tag{44}$$

As is well known [36], for an arbitrary linear temporal processor with impulse response $h(t)$, the test statistic d (cf. Eq. (26)) is given by

$$d = \left| \int_{T_i}^{T_f} x(t) h(t)\, dt \right|^2 . \tag{45}$$

A receiver designed to provide the test statistic in Eq. (45) can be treated as a *correlation receiver*. A simple diagram for this receiver is shown in Fig. 4.

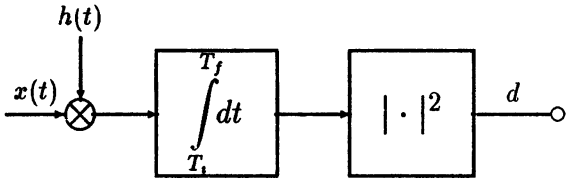

Fig. 4. Receiver structure for linear temporal processor

With the assumption that $n(t)$ is white Gaussian noise, a simple calculation of the SNR from Eq. (44) gives:

$$SNR = \frac{\int_{T_i}^{T_f}\int B_p(t,u)h(t)h(u)\,dt\,du}{\sigma_w \int_{T_i}^{T_f} |h(t)|^2\,dt}. \tag{46}$$

For our further purposes it is convenient to rewrite Eq. (46) as

$$SNR = \frac{E_r}{\sigma_w}\,\delta_{lin},$$

where

$$E_r = \int_{T_i}^{T_f} B_p(t,t)\,dt$$

is the received signal energy during the observation time, and

$$\delta_{lin} = \frac{\int_{T_i}^{T_f}\int B_p(t,u)h(t)h(u)\,dt\,du}{\int_{T_i}^{T_f} B_p(t,t)\,dt \int_{T_i}^{T_f} |h(t)|^2\,dt} \tag{47}$$

has the sense of the coherence–induced SNR gain loss.

A filter $h(t)$ chosen in accordance with $h(t) = s^*(t - \tau_d)$, where τ_d is the expected time delay, defines the receiver structure commonly known as a *standard matched filter*. It provides the optimum performance assuming a

known deterministic signal in white noise. In realistic underwater environments, this is seldom the case. In most practical situations, the signal to be detected is a random function. For the temporal processor of the linear type, the optimal filter response $h_{opt}(t)$ of the correlation receiver can be derived from the following integral equation [36]:

$$\int_{T_i}^{T_f} K_s(t,u)\Phi_i(u)\,du = \lambda_i\Phi_i(t), \quad T_i \leqslant t \leqslant T_f, \tag{48}$$

where

$$K_s(t,u) = \frac{B_p(t,u)}{\int_{T_i}^{T_f} B_p(t,t)\,dt}.$$

The largest eigenvalue $\lambda_{\max} = \lambda_1$ gives the gain loss (47), and the corresponding eigenfunction $\Phi_1(t)$ is the optimal linear filter response, i.e., $\Phi_1(t) = h_{opt}(t)$.

We now treat the general structure of a quadratic temporal processor that determines the potentialities of the random signal detection. The test statistic (cf. Eq. (31)) is now defined as [36]:

$$d = \int_{T_i}^{T_f}\int x(t)h(t,u)x^*(u)\,dt\,du, \tag{49}$$

where $h(t,u)$ is a two–dimensional impulse response function. Let us take into consideration the function $h_f(v,t)$ related to $h(t,u)$ by

$$h(t,u) = \int_{T_i}^{F_f} h_f(v,t)h_f^*(v,u)\,dv, \quad T_i \leqslant t \leqslant T_f; \tag{50}$$

With the use of Eq. (50), the expression (49) takes the form

$$d = \int_{T_i}^{T_f} dv \left| \int_{T_i}^{T_f} dt\, x(t)h_f(t,v) \right|^2.$$

The resulting receiver structure is presented in Fig. 5.

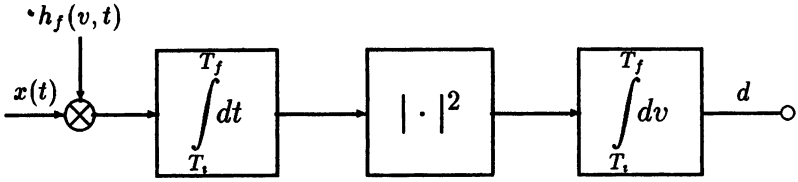

Fig. 5. Receiver structure for quadratic temporal processor

For an arbitrary impulse response function $h(t,u)$, the SNR at the output of the quadratic processor is easily shown to be

$$SNR = \frac{\int_{T_i}^{T_f}\int B_p(t,u)h(t,u)\,dt\,du}{\sigma_w\left[\int_{T_i}^{T_f}\int |h(t,u)|^2\,dt\,du\right]^{1/2}}. \tag{51}$$

The maximum possible SNR is realized if [36]

$$h(t,u) = h_{opt}(t,u),$$

where

$$h_{opt}(t,u) = B_p^*(t,u). \tag{52}$$

Note that the temporal correlation function $B_p(t,u)$ can be expressed directly in terms of the eigenfunction and the eigenvalues of the integral equation (48) as follows

$$B_p(t,u) = E_r \sum_{i=1}^{\infty} \lambda_i \Phi_i(t)\Phi_i^*(u), \quad T_i \leqslant t \leqslant T_f.$$

As a result, the solution of Eq. (50) is

$$h_f(v,t) = \sqrt{E_r}\sum_{i=1}^{\infty} \sqrt{\lambda_i}\,\Phi_i(v)\Phi_i^*(t), \quad T_i \leqslant t \leqslant T_f. \tag{53}$$

For the case of random signals, the scheme in Fig. 5, with $h_f(v,t)$ chosen in accordance with Eq. (53), provides the optimal performance.

The substitution of Eq. (52) into Eq. (51) gives

$$SNR = \frac{E_r}{\sigma_w}\,\delta_{quad},$$

where

$$\delta_{quad} = \frac{\left[\int_{T_i}^{T_f}\int |B_p(t,u)|^2\,dt\,du\right]^{1/2}}{\int_{T_i}^{T_f} B_p(t,t)\,dt} \equiv \sqrt{\sum_{i=1}^{\infty}\lambda_i^2} \tag{54}$$

is the gain loss of the optimal quadratic processor.

4. Numerical simulations and results

In this section, we give some illustrative examples to exhibit numerical prediction of the acoustic MCF in realistic shallow–water environments where bottom interactions are significant. These results are then employed to examine the processing techniques presented above both for (i) vertical and (ii) horizontal $\lambda/2$–arrays, and (iii) temporal filters with the emphasis on the coherence–induced limitations.

The following values of the source parameters are used in simulation: the frequency $f_0 = 500$ Hz; the distance $x = 100$ km; the source depth $z_0 = 100$ m. Some particular results are also presented for the source depth $z_0 = 20$ m to emphasize the effect of the signal modal spectrum which depends on the source depth. The environmental parameter is the speed of wind v which varies from 5 m/s to 10 m/s.

For the horizontal arrays and temporal filters the simulation is focused on the case of white noise background (in spatial and temporal domains, respectively). The simulation of vertical array beamformers includes also modelling of the ambient (modal) sea noise.

4.1. Prediction of the acoustic MCF in shallow water

To illustrate the effects of random surface scattering on acoustic transmission we consider the shallow–water environments and assume the Pierson–Moskowitz spectrum [37] for $F_\eta(æ, \Omega)$:

$$F_\eta(æ,\Omega) = \frac{8.1\times 10^{-3}}{4\pi}\,æ^{-4}\exp\left(-0.74\frac{g^2}{æ^2 v^4}\right)\delta\left(\Omega - \sqrt{g æ}\right), \tag{55}$$

where g is acceleration of gravity, and v is the wind speed over the ocean surface.

The sound–speed profile chosen for our calculations is shown in Fig. 6.

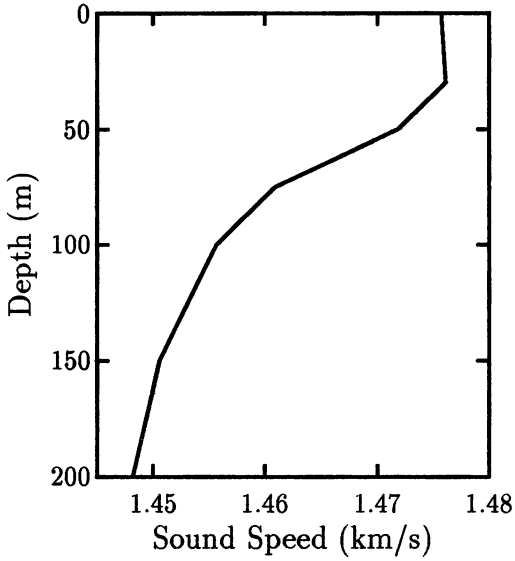

Fig. 6. Sound–speed profile from the Barents Sea

It represents the summer profile from the Barents Sea. The environments selected consist of a layer of water 200 m deep overlying a semi–infinite bottom with constant sound speed of 1700 m/s, density of 1.6 g/cm^3, and attenuation coefficient of 0.02 dB/km·Hz.

The signal coherence degree is characterized by the correlation coefficient:

$$C(\mathbf{r_1}, z_1, t_1|\mathbf{r_2}, z_2, t_2) = \frac{\Gamma(\mathbf{r_1}, z_1, t_1|\mathbf{r_2}, z_2, t_2)}{\sqrt{\Gamma(\mathbf{r_1}, z_1, t_1|\mathbf{r_1}, z_1, t_1)\Gamma(\mathbf{r_2}, z_2, t_2|\mathbf{r_2}, z_2, t_2)}}. \quad (56)$$

This function is fully determined by solution of the eigenvalue problem, Eq. (8), and the second moment of the modal coefficients, Eq. (23).

Figure 7 shows the effect of variable surface roughness on coherence loss in the attenuating channel for given source parameters.

It is clear that, as we increase surface roughness, the rate of coherence loss increases.

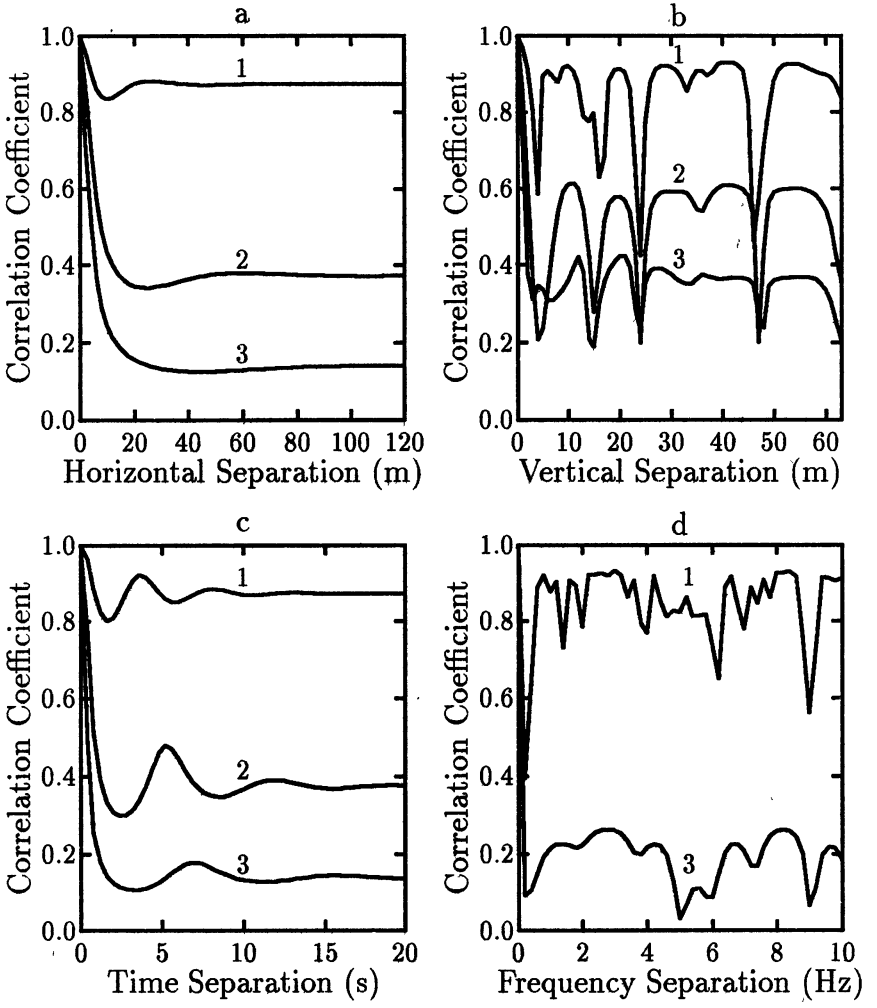

Fig. 7. The normalized MCF of horizontal (a), vertical (b), time (c), and frequency (d) separations in the presence of bottom attenuation at various surface roughness: 1 — v = 5 m/s, 2 — v = 7.5 m/s, 3 — v = 10 m/s. Source frequency is 500 Hz, source depth is 100 m, and distance is 100 km

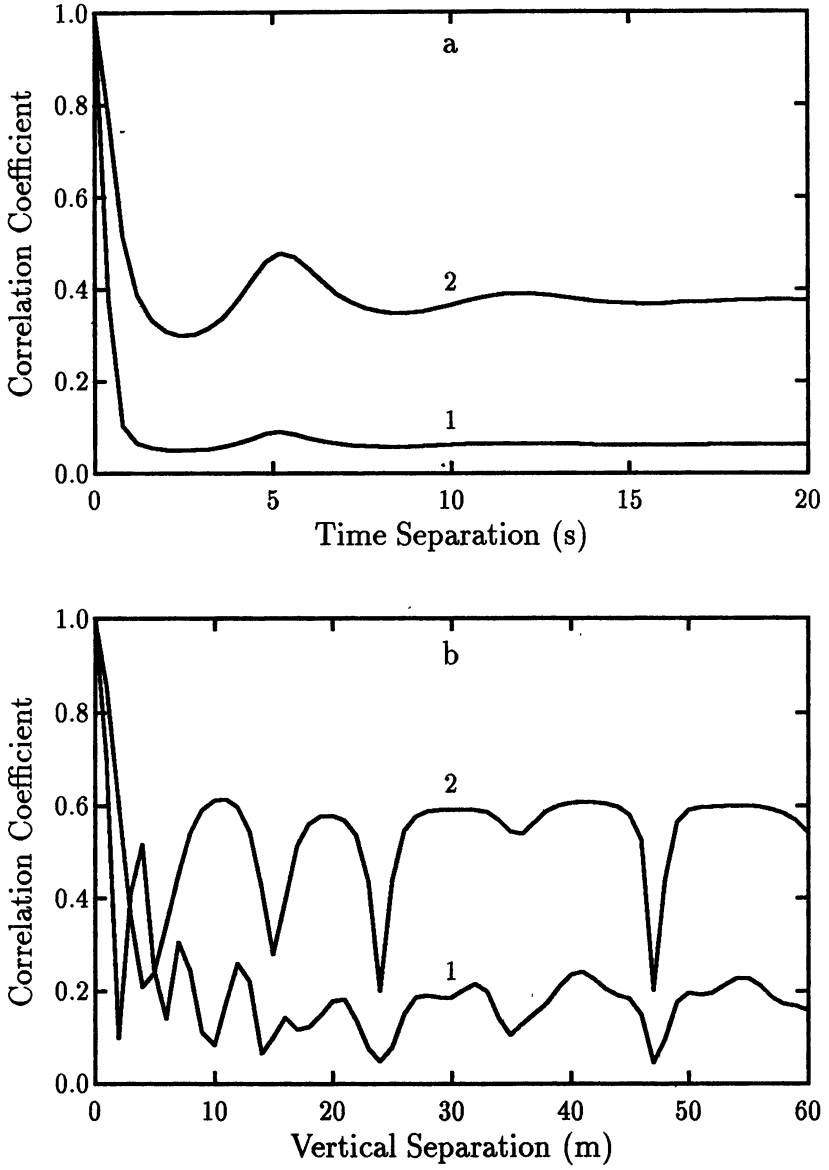

Fig. 8. The normalized MCF of time (a) and vertical (b) separations in the absence (1) and in the presence (2) of bottom attenuation. Source frequency is 500 Hz, source depth is 100 m, distance is 100 km, and wind speed is 7.5 m/s

For moderate v ($v < 7$ m/s), the MCF behaves in an oscillatory fashion, which indicates that the scattering is weak, so that there can be a high degree of signal coherence even at relatively large separation of the observation points. It should be emphasized that the normalized MCF tends asymptotically to the coherence parameter $I_c = |< P(\mathbf{r}, z, t) >|^2 \; / \; < |P(\mathbf{r}, z, t)|^2 >$. The characteristic coherence length, time and coherent bandwidth which are determined by the half–power decay of the correlation coefficient in the case studied depend on wind speed and are approximately 10 m, 2 s and 0.1 Hz, respectively, for $v = 10$ m/s.

For given source parameters and fixed surface roughness ($v = 7.5$ m/s), in Fig. 8 we plot the magnitude of C in the case of time and vertical separations in the absence (curve 1) and in the presence (curve 2) of bottom absorption. The most striking feature in these figures is the fact that the bottom interactions lead to an increase of the coherence degree of the acoustic field. Physically, as was emphasized above, this is a consequence of the competition between the mode coupling, which redistributes the modal energies, and mode stripping, which results in an irreversible loss of energy of the higher modes.

4.2. Vertical array beamformers

In this example, we simulate the key effects of shallow water sound on the array beamforming, including effects of signal coherence and sea noise. To demonstrate the latter one, we assume the noise to be the sum of two mutually uncorrelated components, namely, spatially white noise and ambient sea noise:

$$\mathbf{\Gamma}_n = \sigma \mathbf{I} + \mathbf{\Gamma}_{an}.$$

Here, $\mathbf{I}$ is the identity matrix, σ is the white noise level, and $\mathbf{\Gamma}_{an}$ is the covariance matrix of ambient noise. To calculate the matrix $\mathbf{\Gamma}_{an}$ we use the results from Ref. [25]:

$$(\mathbf{\Gamma}_{an})_{jl} = \sum_{m=1}^{M} \nu_m \varphi_m(z_j) \varphi(z_l),$$

where

$$\nu_m = \frac{\left[\varphi_m'(0)\right]^2}{\kappa_m \operatorname{Im}(\kappa_m) H}, \qquad m = 1, 2, \ldots, M. \tag{57}$$

In what follows we will suppose that the ambient noise is rather intensive in comparison with the white noise, so the ratio of the input white noise power to the input ambient noise power (averaged over the array) is fixed at the level $\simeq -23$ dB.

Figure 9 shows the modal spectra of the received signal (solid line) and the ambient noise (dotted line) for two essentially different source depths, $z_0 = 100$ m and $z_0 = 20$ m. The depth $z_0 = 100$ m corresponds to the source location in the middle of the channel when the source excites effectively the group of relatively low–order modes. On the contrary, the source location in the upper portion leads to excitation of the higher–order modes and to narrowing of the signal modal spectrum at long distances due to non-uniform modal attenuation.

Figure 10 shows the normalized MCFs of the signal and ambient noise along the array (the full array length is $N = 64$ or $L \simeq 95$ m). One can clearly see the significant effect of the surface rough scattering by wind waves on the signal coherence degradation. Typical correlation lengths of the signal and noise are about $N_c \sim 10$, but the signal has residual correlations (coherence "tails") over the entire array, the level of which decreases monotonically with the increase of the wind speed.

A distinguishing feature of shallow–water sound propagation is significant inhomogeneity of the signal covariances over depth. Figure 11 illustrates clearly the inhomogeneity of the signal wavefield along the vertical array. It is seen, in particular, that the averaged signal intensity is much larger for the elements with the numbers $j \gtrsim 40$. The signal correlations are also larger for these elements. Such an inhomogeneous behavior of the signal MCF leads to essential dependence of the array performances, beampattern and gain included, on the array arrangement in the channel.

Figures 12, 13 demonstrate the modal patterns of optimal LBF and adaptive PWBF for two source depths. The effect of cutting off the noised modes is clearly seen in these patterns. In the first case of separated modal spectra (Fig. 12), the plotted modal patterns are similar to each other, so, as demonstrated below, these two beamformers achieve close values of array gain (their difference does not exceed ~ 3 dB). In the second case (Fig. 13), the modal patterns are essentially different. That is a reason of essential difference between the gain performances, which is here ~ 10 dB.

Figure 14 shows one more illustration of the optimal LBF, namely, its weight magnitudes for the largest 64–element array. The lowest numbers of elements correspond here to the greatest depths, so the abscissa axis is inverted with respect to Fig. 11a. These two pictures demonstrate clearly that an effective array length for this case is $N \sim 40$, and arrangement of the array elements in the upper (subsurface) part of the channel is not effective in practice.

Figure 15 shows the 64–element array beampatterns as functions of the steering angle β from Eq. (28), which are plotted for comparison of regular and random–inhomogeneous channels (curves 1 and 2, respectively).

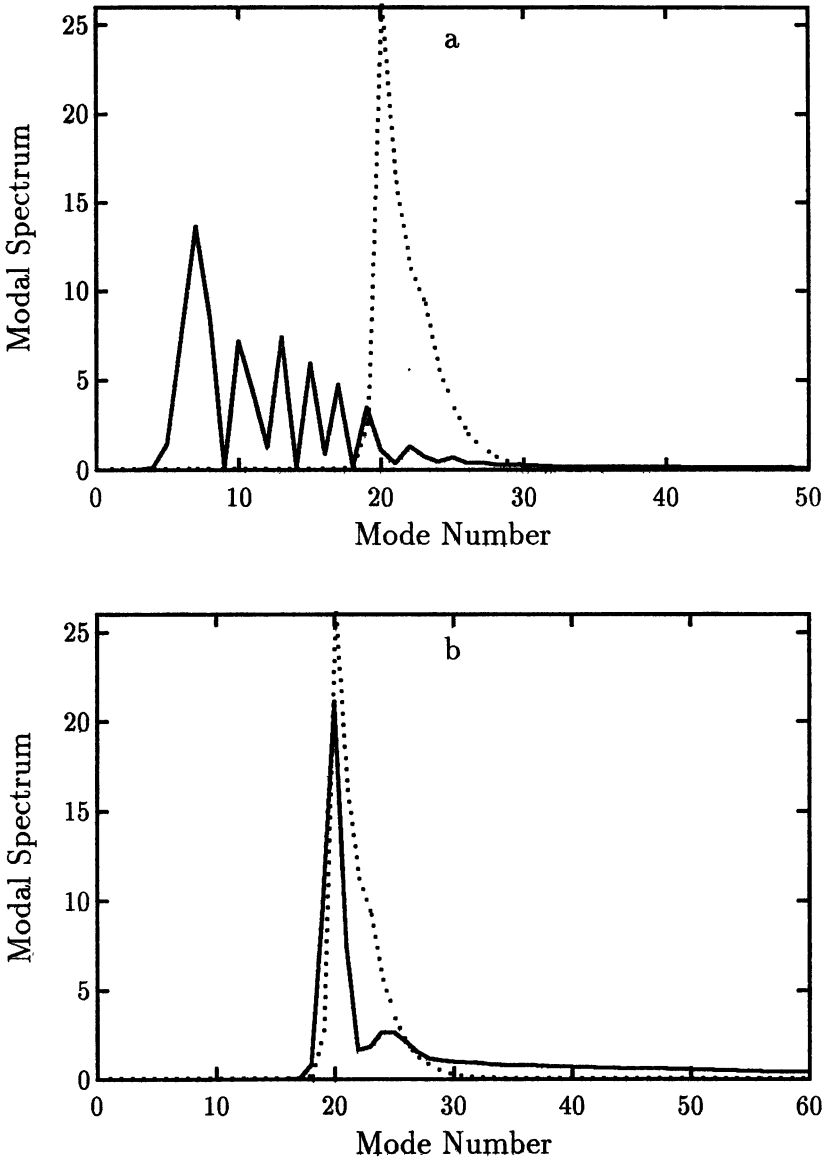

Fig. 9. Modal spectra of signal (solid line) and ambient noise (dotted line) at two selected source depths: $z_0 = 100$ m (a) and $z_0 = 20$ m (b). Source frequency is 500 Hz, distance is 100 km, and wind speed is 10 m/s. Modal spectra have been normalized to the area under their respective curves

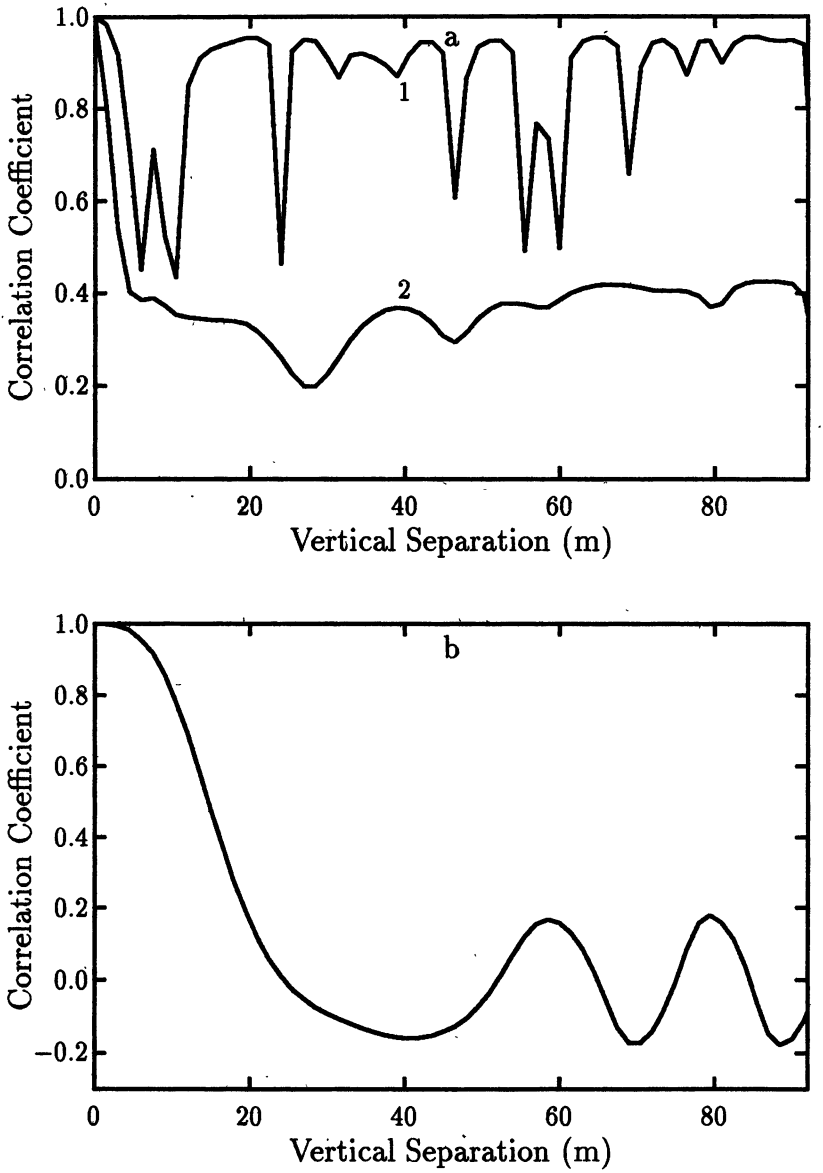

Fig. 10. The normalized MCF of signal (a) and noise (b) along the aperture of the vertical array: 1 — $v = 5$ m/s, 2 — $v = 10$ m/s. Source frequency is 500 Hz, source depth is 100 m, depth of the 1-st hydrophone is 1.5 m, and distance is 100 km

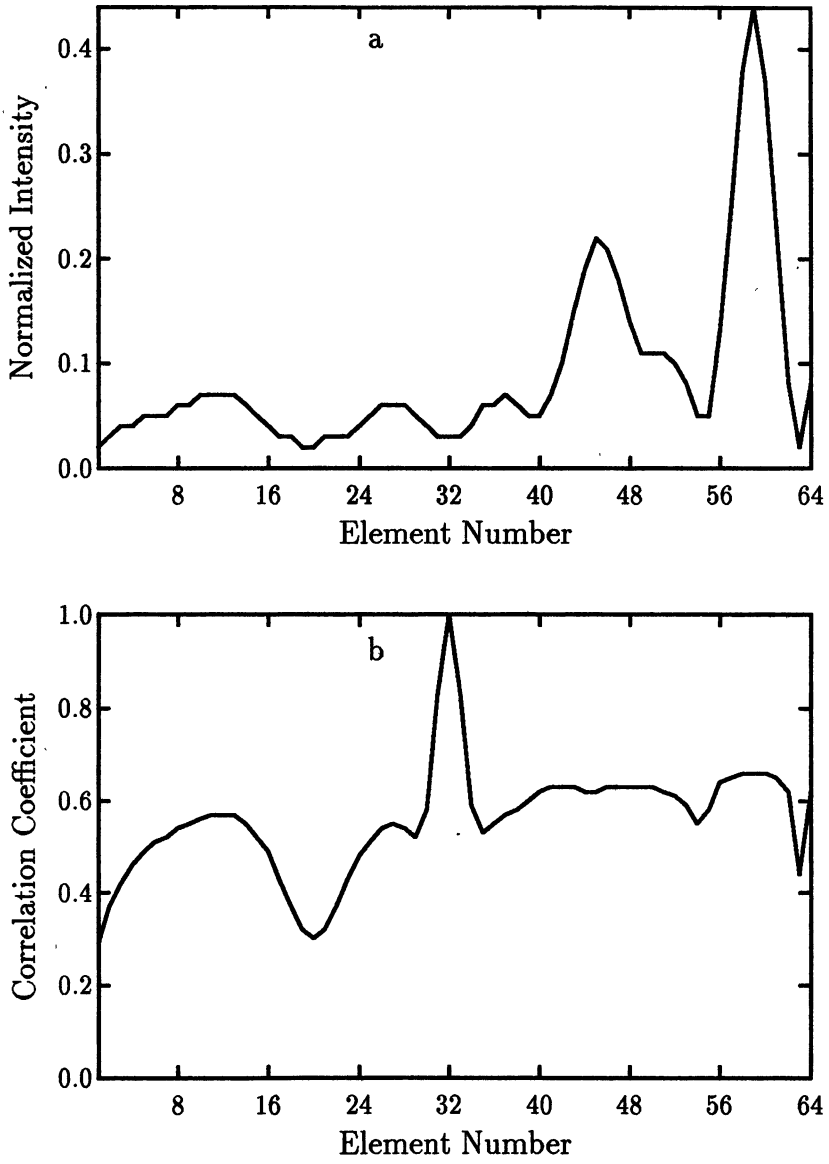

Fig. 11. The normalized signal intensity (a) and the MCF (b) versus element number for the vertical array. Source frequency is 500 Hz, source depth is 100 m, depth of the 1-st hydrophone is 1.5 m, and distance is 100 km

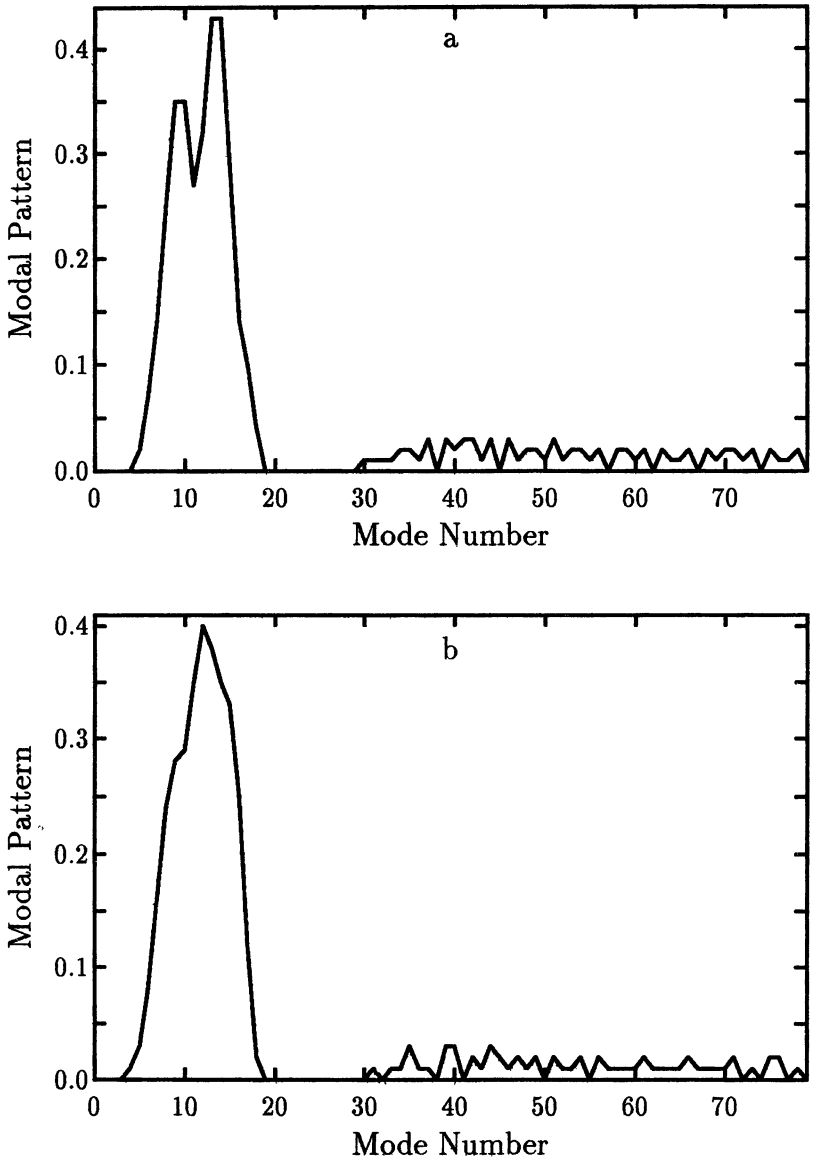

Fig. 12. Modal pattern of the vertical 64–element array in the presence of rough surface scattering ($v = 10$ m/s) for optimal LBF (a) and adaptive PWBF (b). Source frequency is 500 Hz, source depth is 100 m, depth of the 1-st hydrophone is 1.5 m, and distance is 100 km

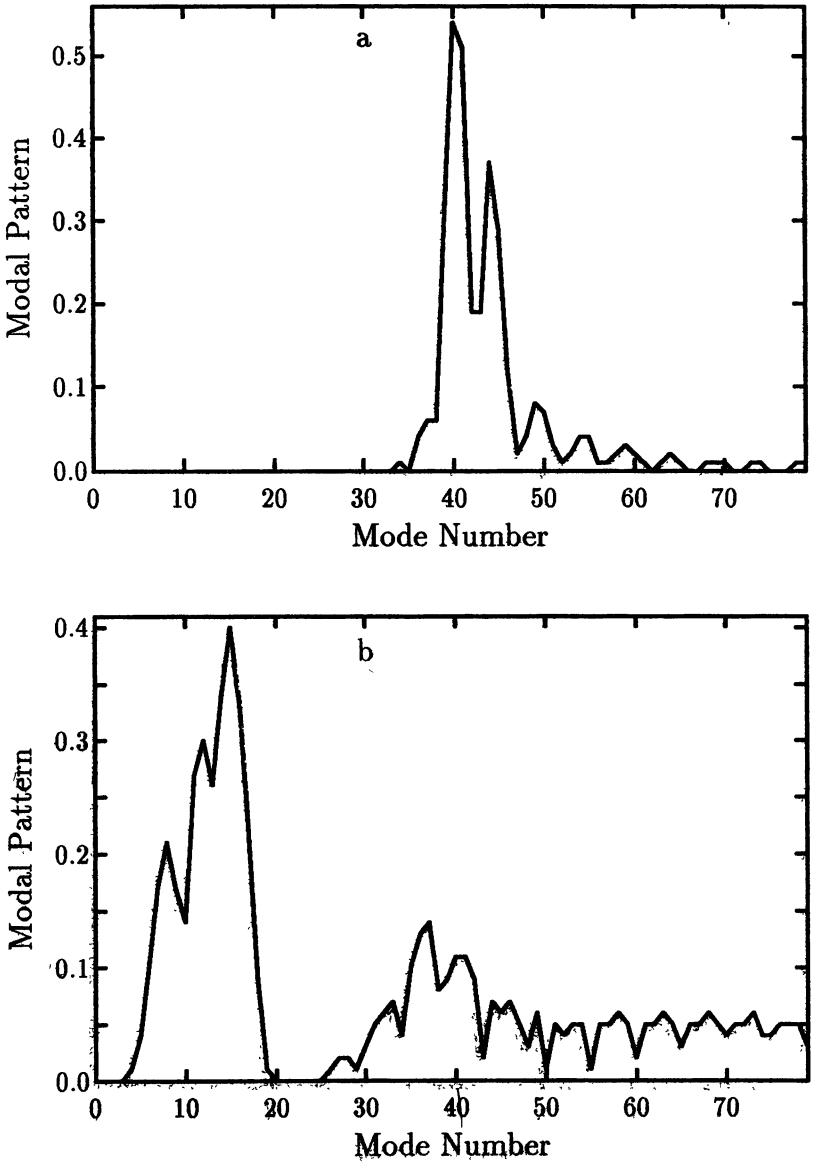

Fig. 13. Modal pattern of the vertical 64–element array in the presence of rough surface scattering (v = 10 m/s) for optimal LBF (a) and adaptive PWBF (b). Source frequency is 500 Hz, source depth is 20 m, depth of the 1-st hydrophone is 1.5 m, and distance is 100 km

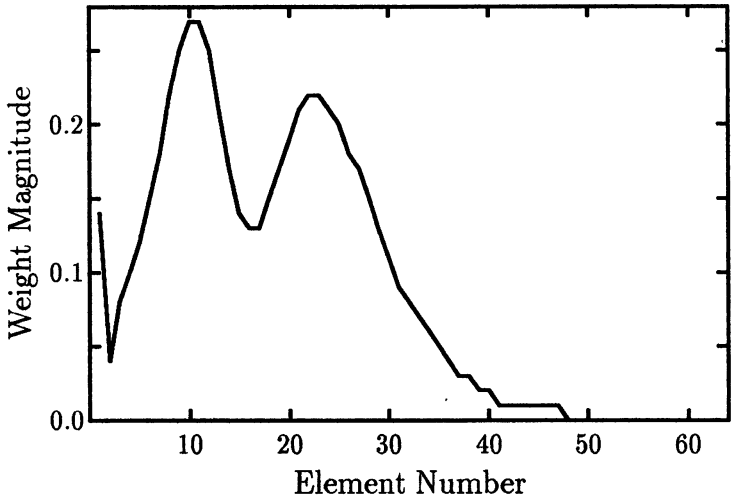

Fig. 14. Weight magnitudes of the 64–element vertical array for optimal LBF. Source frequency is 500 Hz, source depth is 100 m, depth of the 1-st hydrophone is 1.5 m, distance is 100 km, and wind speed is 10 m/s

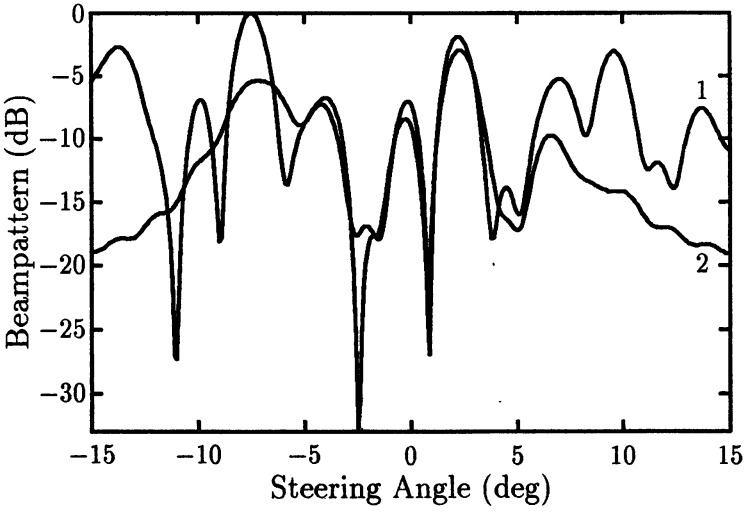

Fig. 15. Beampattern of the vertical 64–element array in the absence (1) and in the presence (2) of rough surface scattering (v = 10 m/s) for the same source parameters and array arrangements as in Fig. 14

The signal coherence loss is seen to lead to a considerable degradation of the multibeam structure of the pattern, similarly to the winter conditions in deep–water environments (see Fig. 12 in Ref. [7]). This beampattern degradation leads, evidently, to very poor gain performance of PWBF.

Figure 16 shows the array gain G as a function of the array length N for the same source depths and wind speed $v = 10$ m/s. Five beamformers are examined for these conditions: optimal QBF and LBF, adaptive PWBF, conventional PWBF (not plotted), and IMBF.

Because the array length is not sufficient to resolve the signal modes with close numbers (see Fig. 9), IMBF (39) was reduced to the matched–mode filter (MF). For the depth $z_0 = 100$ m, when the signal and noise modes are different, the most intensive signal mode ($m = 7$) is chosen to be the reference mode in the MF scheme. On the contrary, the second case ($z_0 = 20$ m) requires a more careful choice based on the analysis of the modal SNRs (the maximum modal SNR is realized here for $m = 79$).

As is seen from Fig. 16a, the first three beamformers enhance considerably the array gain due to modal noise cancellation (prewhitening), and the noise–induced increase of the gain is about $15 - 20$ dB. Beamformers without a special procedure of modal noise prewhitening, PWBF and MF, do not achieve such values of the gain (the PWBF gain is close to the MF gain and does not exceed the level ~ 10 dB). An opposite situation can be realized only if the modal spectra are much more separated from each other. Consequently, a simple modal selection of the signal with the increase of array length leads to a sufficient modal noise cancellation. A similar situation was earlier demonstrated for the summer conditions in deep–water channels (see Fig. 14 in Ref. [7]). Figure 16b shows that "overlapping" of the signal and noise modal spectra leads to gain depression for all beamformers. In this case, a conventional PWBF does not achieve any practical gain for all array lengths (its gain does not exceed $2 - 3$ dB), so the PWBF array is ineffective (cf. Fig. 15 in Ref. [7]).

We emphasize that a decrease of the ambient noise intensity leads to a proportional decrease of the noise–induced effect for the three first beamformers. Besides, it is worthy of notice that a sharp extension of the array by twice increasing the interelement spacing d (for $d = \lambda = 3$ m) leads to a substantial enhancement of the MF gain up to ~ 25 dB.

Thus, we demonstrated here a great importance of the effects of both the signal coherence and ambient modal noise on the vertical array gain. The most critical factor is shown to be the intensive modal noise. A similar conclusion was formulated in our previous papers on the vertical array gain in deep–water environments [3, 7].

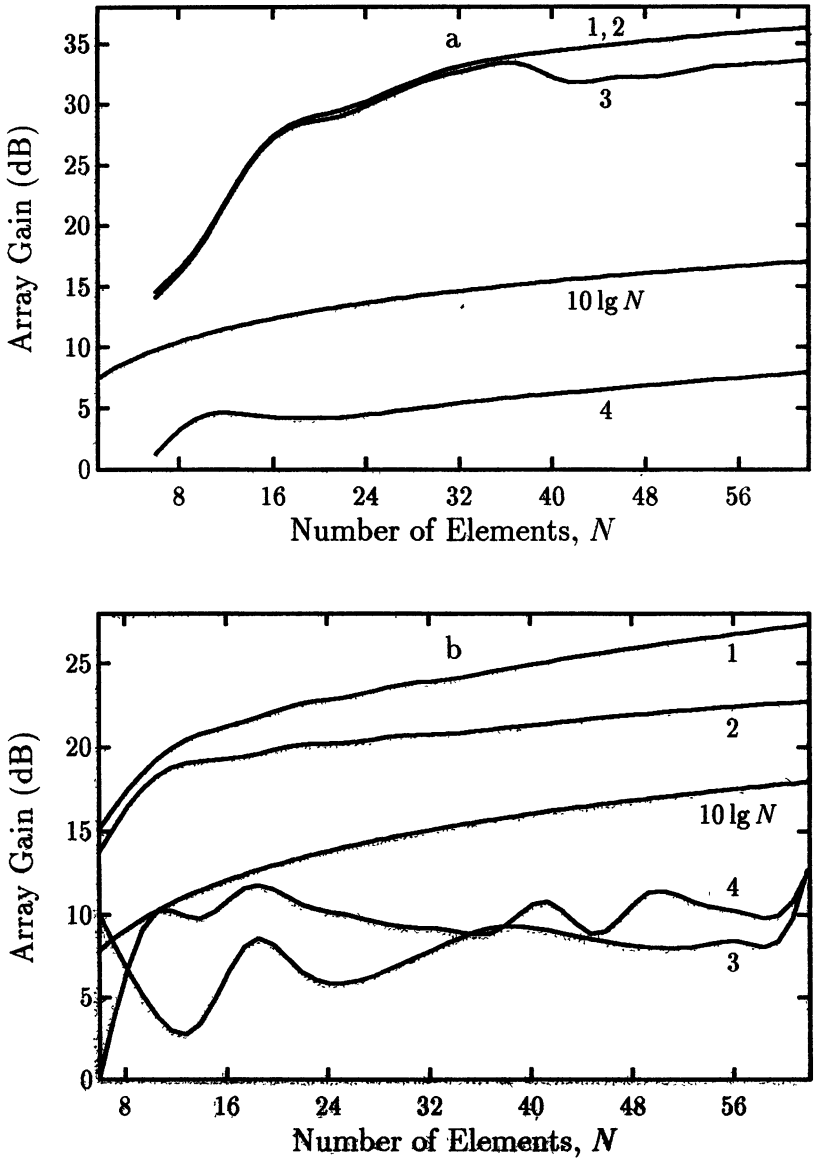

Fig. 16. Vertical array gain as a function of the number of hydrophones: 1 — optimal QBF, 2 — optimal LBF, 3 — adaptive PWBF, 4 — MF. Calculations are for two selected source depths: $z_0 = 100$ m (a) and $z_0 = 20$ m (b). Source frequency is 500 Hz, depth of the 1-st hydrophone is 1.5 m, distance is 100 km, and wind speed is 10 m/s

4.3. Horizontal array beamformers

In this example, we focus our attention on a special case of the white (non-modal) noise background to manifest the coherence–induced effects on array beamforming. We have used a similar "selection" of the noise situations in the horizontal array simulations for deep–water environments [1, 7].

The parameters of simulation are here as follows: the frequency $f_0 = 500$ Hz, the distance $x = 100$ km, the source depth $z_0 = 100$ m, the array depth $z = 145$ m, and the source direction $\alpha = 0°, 30°$. The cross-modal correlations of the signal wavefield almost vanish at such ranges and frequencies. Consequently, the signal is a superposition of weakly correlated plane waves with fluctuating angles of arrival. The cross-modal decorrelation leads to longitudinal coherence loss that increases with the increase of the angle of arrival and vanishes for the transverse propagation (for $\alpha = 0°$). On the contrary, the modal wavefront fluctuations lead to the transverse coherence loss which is maximum, namely, for the transverse arrival.

Figure 17 shows the normalized signal MCF for the two values of α. We conclude from their comparison that the effect of the transverse coherence loss under the conditions of fully developed wind seas is more considerable. The coherence length $L_c \sim 5\lambda \sim 20$ m, or $N_c \sim 10$. The level of residual coherence decreases monotonically with the increase of the wind speed and, eventually, drops to zero for $v \gtrsim 10$ m/s.

The following pictures illustrate the coherence–induced effects on the array beampattern and gain.

Figure 18 shows the effect of surface rough scattering on the beampattern of the 256–element array. Coherence loss is seen to lead to a considerable degradation of the beampattern in the field of its side lobes. Similarly to deep–water environments, a pronounced feature here is a noticeable angular displacement of the main lobes caused by multimode broadening of the signal angular spectrum (cf. Fig. 7 in Ref. [7]). Such displacements lead to an extremely high sensitivity of large–array PWBF to multimode propagation, and adaptive correction of PWBF is required to adjust the steering angle to the angular response maximum.

Figure 19 shows the array gain as a function of the number of elements for the two source directions and the wind speed $v = 10$ m/s. In the first case ($\alpha = 0°$), the coherence–induced gain loss is about -10 dB for all beamformers and array lengths $N \gtrsim 100$. In the second case ($\alpha = 30°$), a considerable degradation of the PWBF gain (for $\beta = \alpha$, see curve 4) is caused primarily by the main lobe displacement emphasized above.

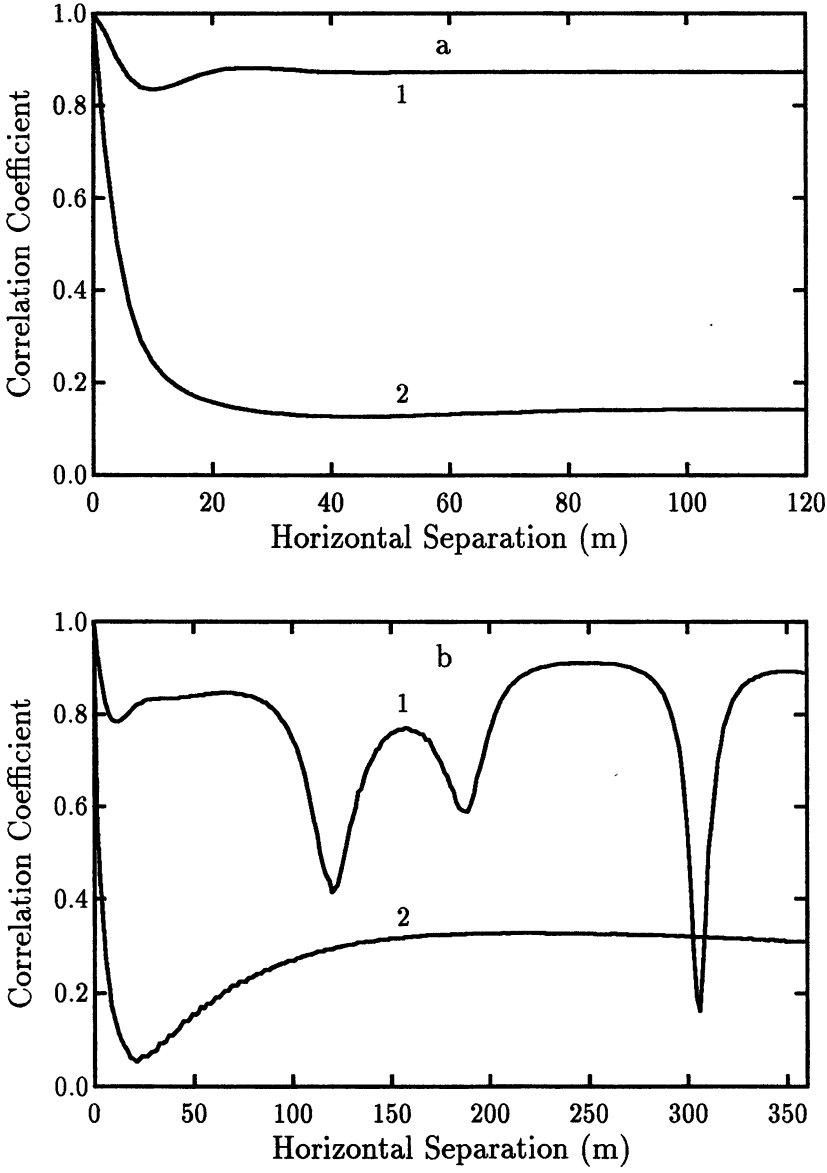

Fig. 17. The normalized MCF of horizontal separation at arrival angle 0° (a) and 30° (b) for various wind speeds: 1 — v = 5 m/s, 2 — v = 10 m/s. Source frequency is 500 Hz, source depth is 100 m, array depth is 145 m, and distance is 100 km

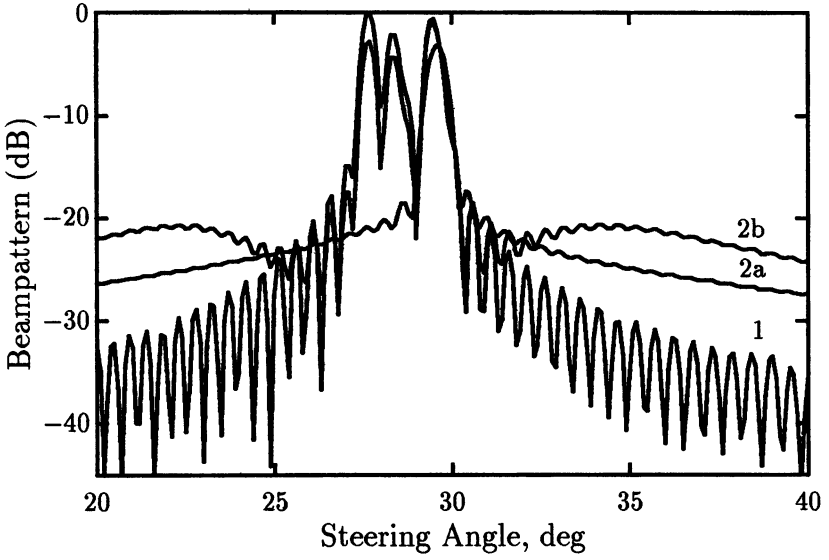

Fig. 18. Beampattern of the horizontal 256–element array in the absence (1) and in the presence (2) of rough surface scattering: 2a — $v = 5$ m/s, 2b — $v = 10$ m/s. Source frequency is 500 Hz, source depth is 100 m, array depth is 145 m, and distance is 100 km

To interpret an oscillating behavior of the PWBF gain we note that the first decrease of the gain (for the array length $N \sim 30$) corresponds to the array beamwidth $\Delta\theta \sim 0.1 \simeq 5°$, and the next one (for $N \sim 150$) to $\Delta\theta \sim 0.02 \simeq 1°$. Comparing these estimations with the beampattern showed above we conclude that the oscillations are caused by its multibeam structure, which, in turn, is caused by the presence of several intensive modes in the signal spectrum (see Fig. 9a.) The most steep decrease of the gain (for $N \gtrsim 150$) corresponds to a critical situation, namely, when the PWBF beamwidth is narrowed in comparison with the angular displacement. In this situation the multimode signal is almost lost by a large–array PWBF. As a result, the gain achieves the maximum value $G \simeq 10$ dB for $N \simeq 150$ and shows a gradual decrease for larger array lengths. The proper angular correction of PWBF leads to the significant increase of the gain up to $\sim 5 - 15$ dB, and the corrected PWBF achieves a nearly optimal LBF performance (see curves 2 and 3). On the other hand, this angular correction of PWBF does not entail any increase in computational complexity. This point is of a great importance for the choice of a suboptimal approach to horizontal large–array beamforming in underwater channels.

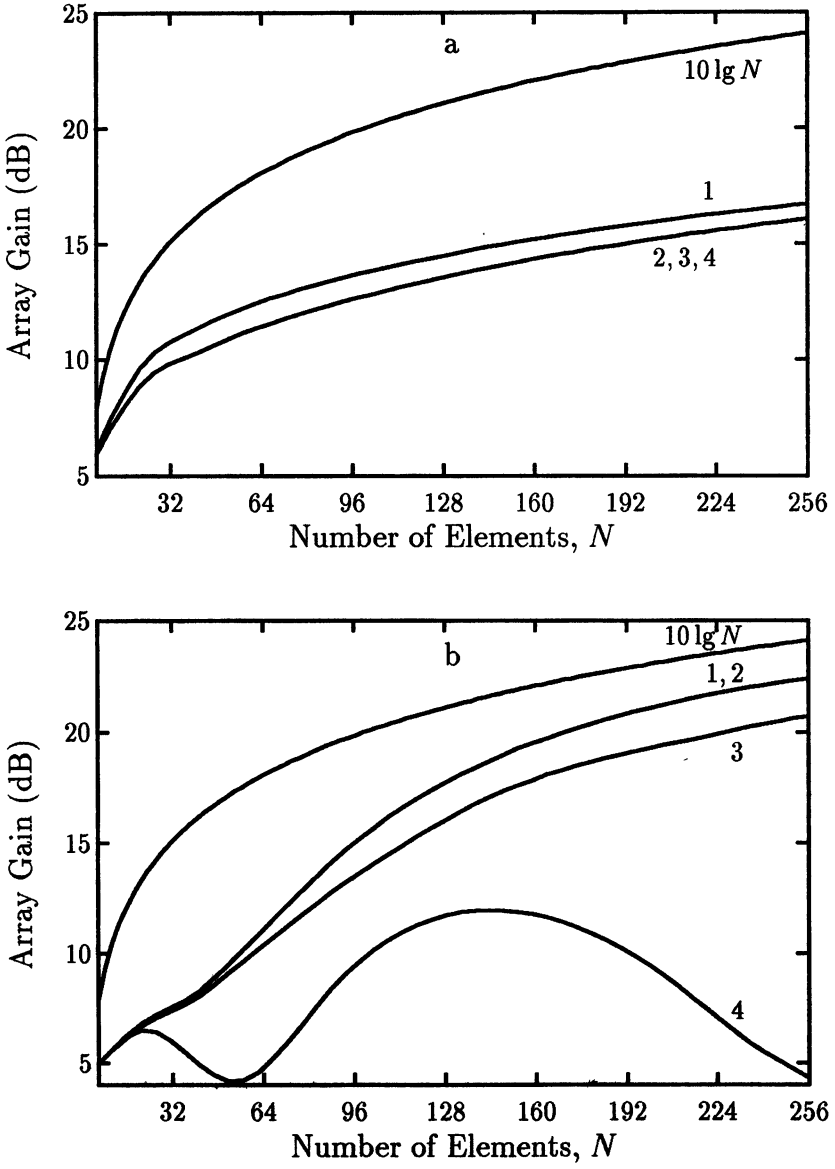

Fig. 19. Horizontal array gain as a function of the number of hydrophones for $v = 10$ m/s, $\alpha = 0°$ (a), and $\alpha = 30°$ (b): 1 — optmal QBF, 2 — optimal LBF, 3 — PWBF with angular correction, 4 — conventional PWBF. Source frequency is 500 Hz, source depth is 100 m, and distance is 100 km

One more beamforming technique, SABF (37), (38), is simulated also for the largest 256–element array to illustrate this suboptimal approach. For the case of $\alpha = 0°$ we obtain that the SABF gain depends on array sectioning (subarrays length N_{SA}) but does not exceed the PWBF gain. The SABF gain ranges from $G_{SA} = 14$ dB for $N_{SA} = 16$, $R = 16$ to $G_{SA} = G_{PW} = 16$ dB for $N_{SA} = 256$, $R = 1$. The relatively weak dependence $G_{SA}(N_{SA})$ is explained by the "tails" of residual coherence over full array. Therefore, the SABF technique may be a suboptimal choice only in the case of the coherence–degraded signal without a partially coherent component.

Thus, the array gain in the case of spatially white noise background is determined directly by the signal coherence degradation which is, in turn, a function of the source and environmental parameters.

4.4. Ensemble–averaged pulse shape and energy loss of temporal filtering

We begin with observing the effect of rough surface scattering on the wavefield intensity as a function of time. The quantity of interest, $I(t)$, can be derived from Eq. (41) by letting $t_1 = t_2 = t$:

$$I(t) = \left| \sum_{n=1}^{M} \frac{1}{\kappa_n} < p_n(\mathbf{r}, t > \varphi_n(z) \right|^2 + \sum_{n=1}^{M} \frac{1}{\kappa_n} \Gamma^i_{nn}(x,t,t)\, \varphi_n^2(z). \qquad (58)$$

Equation (58) describes the shape of an ensemble–averaged pulse.

As an example we consider the Gaussian shape for the input pulse at $x = 0$:

$$s(t) = \exp\left[-\left(t^2/2T^2\right)\right].$$

Figure 20 shows the behavior of $\sqrt{I(t)}$ for 500 Hz and $T = 50$ ms in the absence (a) and in the presence (b) of random surface scattering. The wind speed was taken to be 10 m/s. (The theoretical curves in Fig. 20 were calculated for the sound speed profile in Fig. 6 with the use of the MCF of frequency and time separations indicated in Figs. 7c and 7d).

In the absence of scattering (Fig. 20a), each mode carries the Gaussian pulse, which was launched at $x = 0$, independent of all the other modes. Each mode suffers its characteristic bottom absorption and travels at a different group velocity.

If the pulses overlap, we receive a long pulse instead of a sequence of individual short pulses. The signal is distorted by the group delay differences of the modes. The total pulse width is proportional to the propagation distance.

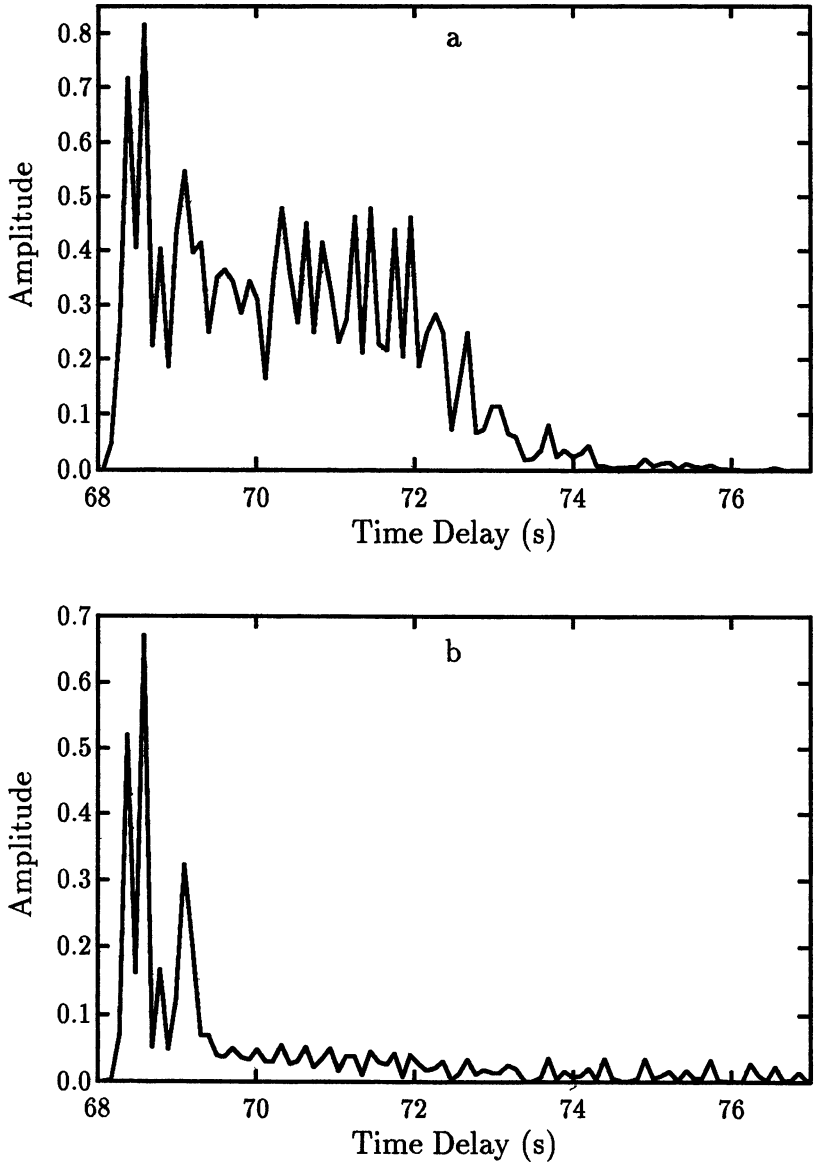

Fig. 20. Temporal behavior of the rms pulse amplitude in the absence (a) and in the presence (b) of random inhomogeneities. Source frequency is 500 Hz, source depth is 100 m, receiver depth is 145 m, and distance is 100 km. Amplitude values have been normalized to the area under their respective curves

The first arrival times belong to the lowest–order mode pulses having the largest group velocities v_n, and the last ones are observed for higher–order mode pulses with relatively low v_n. On the other hand, for a given shallow–water environment, the modal attenuation resulting from sediment absorption increases with the mode number. As a result, we can see on the arrival pattern the largest peaks only for the initial time delays.

If the modes are coupled with each other due to scattering, the pulse performance of the multimode waveguide is changed. Comparison of Fig. 20a and Fig. 20b shows that multiple scattering leads to a decrease of the amplitudes of the resolved initial peaks and to a sharper drop of the intensity at the end of the observation.

Consider now the energy loss of the temporal filtering caused by the time and frequency decorrelation of the registered pulse. The results of numerical calculations of the energy losses according to Eqs. (47), (54) as a function of pulse duration T are presented in Fig. 21. The calculations were carried out for f_0 =500 Hz, z_0 =100 m, and x =100 km. The wind speed was taken to be 10 m/s.

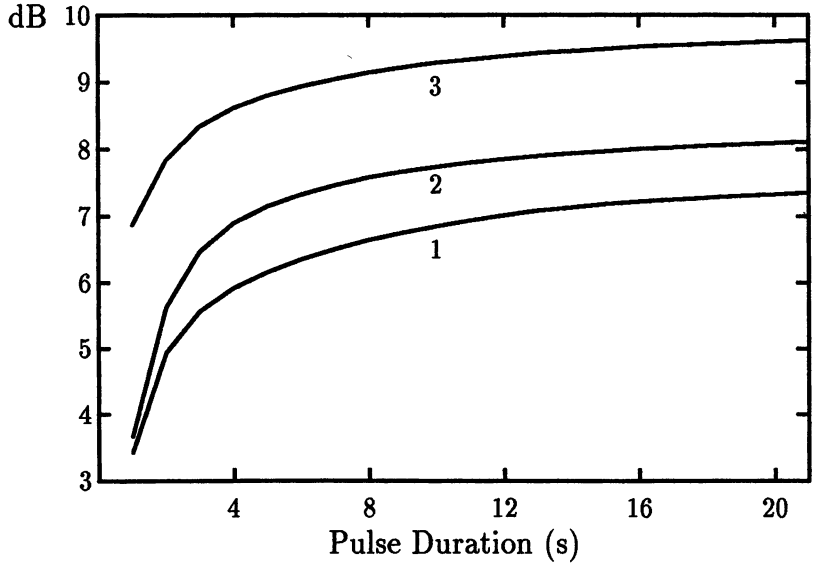

Fig. 21. The energy loss of temporal filtering versus pulse duration: 1 — optimal quadratic processor, 2 — optimal linear processor, 3 — standard matched filter

Figure 21 indicates that the coherence–induced gain loss increases monotonically with pulse duration. When T exceeds the correlation time τ_c (in

the case considered τ_c is of the order of 6 s), the corresponding curve tends to a "saturation" plateau. The gain loss "gap" between the optimal quadratic and standard matched filtering techniques is about 3 dB for the pulse length of about 20 s.

5. Discussion and conclusions

In this section, we summarize the numerical predictions presented above to conclude our study of the acoustic coherence effects on the array beamforming and temporal processing techniques in realistic shallow–water channels.

5.1. Acoustic MCF

From an application point of view, the knowledge of the spatial–temporal MCF of the registered acoustic field is of the uppermost importance to optimize the signal processing techniques and, therefore, to decrease a coherence–induced degradation of the processor performances.

In the framework of a modal approach, the total MCF can be expressed as the weighted sum of the self–modal and cross–modal coherence functions. Based on the wave-theoretical description we formulated second moment equations for the quantities of interest in which an extra absorption term modeling the bottom effects was included. The solution for the self–modal functions was obtained by direct numerical integration of a coupled set of the corresponding partial differential equations. For the cross-modes we used an useful approximate analytical solution which is valid when the characteristic correlation length of surface irregularities is much less than the typical mode cycle distance. Physically, the cross-modes describe interference pattern of the acoustic field. Under the assumption made, this pattern is fully determined by the coherent component of the propagation signal. As a result, the cross-modal MCFs are exponentially decaying functions of range. Therefore, with increasing range, the self-modal MCFs become increasingly more important and exclusively these terms play a dominant role in modeling the asymptotic behavior of the total acoustic MCF.

The application was illustrated by numerical computation of the expected acoustic coherence for typical shallow–water environments from the Barents Sea under the assumption that the fully developed seas are the dominant source of transmission fluctuations. Several conclusions may be drawn from the presented analysis.

First, it was established that the spatial and temporal MCFs are significantly affected by random rough surface scattering. As we increased

surface roughness, the rate of coherence loss increased (for given range and frequency).

However, of the most importance is the fact that the behavior of the acoustic MCF in shallow water is fundamentally different from the corresponding MCF behavior for the deep–water situation due to modal stripping caused by considerably different modal attenuations. The major effect is the increase of the coherence degree of the acoustic field.

5.2. Large–array beamforming

Similarly to deep–water environments, the following three key factors of large–array beamforming were demonstrated distinctly in this paper. These are, namely, (i) multimode spreading of the received signal angular spectrum; (ii) signal coherence degradation; (iii) modal structure of the ambient sea noise, which is a critical factor for the vertical array beamformers. An inherent feature of shallow–water environments is, however, a very inhomogeneous behavior of the MCF of space, including the cross–element correlations and wavefield intensity. This feature concerns both the vertical and horizontal MCFs and leads to essential dependence of the array gain on the array arrangement in a channel.

A physical reason for such a complicated behavior is a relatively small number of the modes propagating over long distances under the conditions of modal stripping through the bottom interactions, and partial conservation of the modal interference pattern. Therefore, the particular effects of the factors pointed out on the array performance depend cardinally on many parameters including the source ones (frequency region, depth, distance), the environmental ones (type of the channel, or sound–speed profile, bottom properties, speed of wind and other parameters characterizing the intensity of the sound scattering), and, finally, the array parameters (total length and elements arrangement). The numerical results presented permit us to conclude that the problem of adequate predictions of the beamforming performances in shallow–water channels is more difficult and requires a much more detailed consideration taking into account all the parameters specified.

Several essential comments this study could be formulated, however, as universal physical conclusions concerned with the vertical and horizontal array beamformers.

Vertical arrays

A key factor of vertical array beamforming is the relationship between the signal and noise modal spectra. While the sea noise spectrum is rather stable and is determined by the environmental parameters of an underwa-

ter channel, the signal spectrum is a function of the source location. This dependence is most important for moderate distances, when the effect of modal stripping is not so essential as to lead to a considerable deformation of the modal intensities. Therefore, for a given set of parameters (frequency, distance, array arrangement), some source positions are "masked" by overlapping of the signal and noise modal spectra.

In the case of separated spectra, of the most importance is the procedure of modal noise prewhitening (achieved by the noise covariance matrix inversion), which leads to a great enhancement of the output SNR and gain above the level of $G = N$. All the noise–suppressing beamformers simulated here (optimal QBF and LBF, adaptive PWBF) demonstrate this possibility distinctly. On the contrary, the beamformers without purposeful noise cancellation (PWBF, MF) show a rather poor performance if the array length is not sufficient for spatial selection of the "pure" signal modes. For any modal spectra, short arrays arranged in the subsurface part of the shallow–water channel are not so effective because the depth functions, mainly, of high–order and quickly attenuating modes are located under the surface.

The modal noise suppression by adaptive PWBF allows us to consider the PWBF techniques as a good choice for effective large–array processing.

Horizontal arrays

Of primary importance for large horizontal arrays is the modal spectrum broadening which is "projected" on the array in the case of non-zero angle of arrival. If the signal modal spectrum contains several groups of intensive modes (as in our simulations), the array angular response is also split in the field of the main lobe. This feature leads to noticeable oscillations of the PWBF gain as a function of the array length, or, actually, of the beamwidth. (An oscillating behavior of the PWBF gain is typical also for vertical arrays due to the existence of several comparable peaks in the beampattern.) This means that the PWBF gain can essentially vary as a function of the source direction. The adaptive correction of the steering angle can lead to a significant gain enhancement, which is rather essential for the array lengths $L \sim 50\lambda$.

An obvious advantage of this approach over suboptimal beamforming is its comparative simplicity because the array performance can be easily maintained by re-forming of the beampattern. Such a useful possibility is firmly restricted, however, by the case of residual signal coherence over the full array length. Comparing the PWBF techniques with the optimal ones for both the shallow–water and deep–water simulations we conclude that the residual coherence is the cause of a relatively small additional gain of the optimal QBF over all LBFs, PWBF included.

5.3. Temporal filters

The general theory of random signal detection was also applied to shallow water acoustics for the construction of temporal processors, optimal one included. The key role in the temporal performance analysis belongs to the MCF of time and frequency. We employed the wave-theoretical expression for the MCF of interest for the study of the combined effects of random surface scattering and bottom interactions on the shape of ensemble–averaged pulse and on the temporal filtering performance.

The most striking feature in the behavior of the EAP shape is the fact that the largest peaks on the arrival pattern are observed only for the initial time delays. Physically it is rather clear, if we take into account that the first arrival times belong to the lowest–order mode pulses having the largest group velocities v_n, and the last ones belong to higher–order mode pulses with relatively low v_n. On the other hand, for a typical shallow–water environment, the modal attenuation resulting from sediment absorption increases with the mode number. As a result, the main contribution to the total wavefield intensity versus time is made by the weakly attenuated lowest–order mode pulses. Multiple rough surface scattering leads to a decrease of the amplitudes of the resolved initial peaks and to a sharper drop of the intensity at the end of the observation.

The presence of rough surface scattering results in the energy loss of the temporal filtering due to time and frequency decorrelations of the registered pulse. It has been established that the corresponding coherence–induced gain loss increases monotonically with pulse duration T. When T exceeds the characteristic signal correlation time the observed gain loss tends to a "saturation" plateau. For given shallow water environments, the level of this plateau depends essentially on the technique used: the minimal level corresponds to optimal quadratic processor and the maximal one corresponds to a conventional matched filter. Thus, for typical conditions from the Barents Sea, the temporal SNR degradation at $f_0 = 500$ Hz and $T = 20$ s is rather substantial (of order 6 dB), even for the optimal quadratic filter.

5.4. Summary

In this paper, the effects of shallow–water sound were examined for various types of array beamformers and temporal filters. Our approach was to incorporate the realistic calculations of the MCF of space, time and frequency for comparative analysis of the linear and quadratic signal processors, spatial and temporal ones included. It was shown distinctly that both the signal coherence and sea noise mutually affect the processor performance.

ACKNOWLEDGMENTS

This work was supported in part by the Russian Foundation for Basic Research under Grants No 96–02–19462, No 96–02–19460, No 96–15–96592, No 97–02–17536, No 97–02–17555, and the TNO Electronics and Physics Laboratory (The Netherlands).

References

1. *E. Yu. Gorodetskaya* et al. Effects of long-range sound propagation in random ocean on horizontal array gain loss // Acoust. Phys., 1996, vol. 42(5), pp. 543–649.
2. *E. Yu. Gorodetskaya, A. I. Malekhanov, A. G. Sazontov, and N. K. Vdovicheva.* Large–array gain limitations in a random oceanic waveguide with application to the North Pacific // In: Proc. 3rd Europ. Conf. on Underwater Acoustics, edited by J. S. Papadakis (Heraklion, Greece, 1996), Vol. 1, pp. 507–512.
3. *N. K. Vdovicheva* et al. Gain of a vertical antenna array in a randomly inhomogeneous oceanic waveguide. // Acoust. Phys., 1997, vol. 43(6), pp. 669–675.
4. *A. G. Sazontov.* Acoustic coherence in a deep random oceanic waveguide // In: Formation of Acoustical Fields in Oceanic Waveguides, edited by V. I. Talanov and V. A. Zverev (Institute of Applied Physics RAS, Nizhny Novgorod, 1995), pp. 37–62.
5. *A. G. Sazontov.* Quasi–classical solution of the radiation transport equation in a scattering medium with regular refraction // Acoust. Phys., 1996, vol. 42(4), pp. 487–494.
6. *A. G. Sazontov and N. K. Vdovicheva.* Modelling low-frequency sound scattering in a random oceanic waveguide using a modal formulation // In: Proc. 3rd Europ. Conf. on Underwater Acoustics, edited by J. S. Papadakis (Heraklion, Greece, 1996), Vol. 1, pp. 133–138.
7. *E. Yu. Gorodetskaya* et al. Acoustic coherence in a deep water: effects on array signal processing // In: Formation of Acoustical Fields in Oceanic Waveguides, edited by V. A. Zverev (Institute of Applied Physics RAS, Nizhny Novgorod, 1997), pp. 5–47.
8. *A. G. Sazontov and V. A. Farfel'.* Matched filtering of narrow–band pulsed signal transmitted through random waveguide channel // Sov. Phys. Acoust., 1992, vol. 38(6), pp. 591–595.

9. *A. G. Sazontov and V. A. Farfel'.* Calculation of the coherence degree and form of a pulse sound signal in an oceanic waveguide with a rough surface // Acoust. Phys., 1995, vol. 41(1), pp. 109–113.
10. *S. M. Flatte, R. Dashen, W. H. Munk, K. M. Watson, and F. Zachariasen.* Sound Transmission Through a Fluctuating Ocean, edited by S. M. Flatte (Cambridge U.P., New York, 1979).
11. Bottom–Interacting Ocean Acoustics, edited by W. Kuperman and Finn B. Jensen (Plenum Press, New York, 1980).
12. *B. G. Katsnelson and V. G. Petnikov.* Shallow Water Acoustics (Nauka, Moscow, 1997) [in Russian].
13. *M. J. Beran and S. Frankenthal.* Volume scattering in a shallow channel // J. Acoust. Soc. Amer., 1992, vol. 91(5), pp. 3203–3211.
14. *D. B. Creamer and B. J. Orchard.* Acoustic wave propagation in a random, shallow–water waveguide // J. Acoust. Soc. Amer., 1994, vol. 95(5), pp. 2927.
15. *D. B. Creamer.* Scintillating shallow–water waveguides // J. Acoust. Soc. Amer., 1996, vol. 99(5), pp. 2825–2838.
16. *M. J. Beran and S. Frankenthal.* Combined volume and surface scattering in a channel using a modal formulation // J. Acoust. Soc. Amer., 1996, vol. 100(3), pp. 1463–1472.
17. *C. Garrett and W. H. Munk.* Space–time scales of internal waves: A progress report // J. Geophys. Res., 1975, vol. 80(3), pp. 291–297.
18. *W. H. Munk.* Internal waves and small–scale processes // In: Evolution of Physical Oceanography, edited by B. A. Warren and C. Wunsch (MIT, ambridge, MA, 1981), pp. 264–291.
19. *E. L. Hamilton.* Geoacoustic models of the sea floor // In: Physics of Sound in Marine Sediments, edited by L. Hampton (Plenum, New York, 1974), pp. 264–291.
20. *L. M. Brekhovskikh and Yu. P. Lysanov.* Fundamentals of Ocean Acoustics (Springer–Verlag, Berlin, New York, 1982).
21. *F. G. Bass and I. M. Fuks.* Wave Scattering From Statistically Rough Surface (Pergamon, Oxford, U.K, 1979).
22. *A. G. Nechaev.* Decay of the interference structure of the sound field in an ocean with random inhomogeneities // Sov. Phys. Acoust., 1987, vol. 33(3), pp. 312–314.
23. *A. Beilis and F. D. Tappert.* Coupled mode analysis of multiply rough surface scattering // J. Acoust. Soc. Amer., 1979, vol. 66(3), pp. 811–826.

24. *B. M. Kudryashov.* On the evaluation of acoustic fields in waveguides with statistically rough surface // In: Mathematical Problems of Geophysics (Nauka, Novosibirsk, 1973), Vol. 4, pp. 256–272 [in Russian].
25. *W. A. Kuperman and F. Ingenito.* Spatial correlation of surface generated noise in a stratified ocean // J. Acoust. Soc. Amer., 1980, vol. 67(6), pp. 1988–1996.
26. *H. Cox.* Line array performance when the signal coherence is spatially dependent // J. Acoust. Soc. Amer., 1973, vol. 54, pp. 1743–1746.
27. *A. I. Malekhanov and V. I. Talanov.* Optimal signal reception in multimode waveguides // Sov. Phys. Acoust., 1990, vol. 36(5), pp. 496–499.
28. *D. R. Morgan and T. M. Smith.* Coherence effects on the detection performance of quadratic array processors, with application to large–array matched–field beamforming // J. Acoust. Soc. Amer., 1990, vol. 87(2), pp. 737–747.
29. *Ya. D. Shirman and V. N. Manzhos.* Theory and Techniques of Signal Processing in Radar (Radio i Svyaz', Moscow, 1981) [in Russian].
30. *R. A. Monzingo and T. W. Miller.* Introduction to Adaptive Arrays (Wiley, New York, 1980).
31. *H. Cox, R. M. Zeskind, and M. Myers.* A subarray approach to matched–field processing // J. Acoust. Soc. Amer., 1990, vol. 87, pp. 168–178.
32. *A. I. Malekhanov.* Incoherent spatial mode filtering in randomly inhomogeneous ocean waveguides // Sov. Phys. Acoust., 1992, vol. 38(5), pp. 489–493.
33. *E. Yu. Gorodetskaya, A. I. Malekhanov, and V. I. Talanov.* Modeling of the optimal array signal processing in underwater sound channels // Sov. Phys. Acoust., 1992, vol. 38(6), pp. 571–575.
34. *A. I. Malekhanov.* Optimal spatial signal processing in nonstationary waveguides // In: Proc. 14th GRETSI Sypm. on Signal and Image Processing (Juan–les–Pins, 1993), pp. 293–296.
35. *A. I. Malekhanov and G. V. Serebryakov.* The detection performance of optimal array processing of the discrete spectrum signals // Radiotekhnika i Elektronika, 1993, vol. 38(6), pp. 1069–1080 [in Russian].
36. *H. L. Van Trees.* Detection, Estimation and Modulation Theory, Part III (Wiley, New York, 1969).
37. *W. J. Pierson and L. Moskowitz.* A proposed spectral form for fully developed wind seas based on the similarity theory of S. A. Kitaigorodskii // J. Geophys. Res., 1964, vol. 69(24), pp. 5181–5190.

The Investigation of Acoustic Fluctuations in a Lake Environment

A. V. Lebedev, B. M. Salin

INTRODUCTION

Fluctuations of the sound propagating in a sea environment were studied extensively (see [1, 2] and the references therein). Such fluctuations are caused by rough surface scattering and perturbations in a waveguide due to internal waves, turbulence, and other factors. This paper is concerned with experimental data obtained in a lake environment. The measurements were carried out in 1997–1998 in the Sankhar lake. The Sankhar lake is a carst lake with a mean depth of 15 meters that has the size of 1.5 km [1] in "length" and 500 m in "width" (see the scheme in Fig. 1). As the lake is deep, the temperature in summer conditions varies from $20 \div 24°C$ at the surface to 4°C at the bottom. The main variations occur within the depth of $4 \div 7$ meters. The main goal of the measurements was investigation of acoustic fluctuations and hydrophysical characteristics in such an interesting environment.

SPATIO-TEMPORAL CHARACTERISTICS OF ACOUSTIC SIGNALS

Acoustic signals were recorded by horizontal and vertical arrays (Fig. 1). The arrays consisted of 64 hydrophones spaced 19 cm apart. Hydrophysical characteristics were recorded by a surface displacement sensor mounted at the bottom near the pontoon, a temperature sensor, and a wind force sensor (see Fig. 1).

Figure 2 shows spatio-temporal characteristics of the acoustic signal received by hydrophones of the horizontal array at the carrier frequencies

[1] Including the bay of $500 \div 600$ m long.

$F = 979.761$ Hz and $F = 1480.408$ Hz. The spectra depicted in Fig. 2 were obtained after the following data processing:

$$A(\Delta F) = \sqrt{\langle |a_l(\Delta F)|^2 \rangle} \equiv \sqrt{\frac{1}{N_{avg}} \sum_{i=1}^{N_{avg}} |a_l(\Delta F)|^2}, \quad l = 1, 2, 3, \qquad (1)$$

where N_{avg} is the number of averaging and $a_l(\Delta F)$ are defined as follows:

$$a_1(\Delta F) = \sqrt{\frac{1}{N} \sum_{k=1}^{N} |\hat{p}_k(\Delta F)|^2}. \qquad (2)$$

Here, N is the amount of hydrophones in the array ($N = 64$); k is the hydrophone number; $\hat{p}_k(\Delta F)$ is defined as:

$$\hat{p}_k(\Delta F) = \frac{1}{M} \sum_{j=1}^{M} p_k(t_j) \exp(i2\pi \Delta F t_j), \qquad (3)$$

where Mt_j is the time during which each time series is analysed ; $t_j = j/F_s$, F_s is the sampling frequency ($F_s = 10.767$ Hz), $-F_s/2 < \Delta F < +F_s/2$; and $p_k(t_j)$ the complex output of a hydrophone after heterodyne and low-pass filters. The carrier frequency F_m coincides with the heterodyne frequency.

The data presented in Fig. 2b correspond to the array output for source-receiver direction:

$$a_2(\Delta F) = \frac{1}{M} \sum_{j=1}^{M} \max(\zeta_k(t_j)) \exp(i2\pi \Delta F t_j). \qquad (4)$$

Here, ζ_k is defined as

$$\zeta_k(t_j) = \frac{1}{N} \sum_{k=1}^{N} p_k(t_j) \exp(-i2\pi F_m \Delta x \; k/C_0), \qquad (5)$$

where Δx is the distance between the hydrophones in the array and C_0 is the sound velocity.

The procedure (5) allows us to select fluctuations along the line linking the source and the array center if there are no additional reflections which are a hindrance. As only one source was used, we can also employ the following procedure to determine fluctuations along the source-receiver line (Fig. 2c):

$$a_3(\Delta F) = \frac{1}{M} \sum_{j=1}^{M} \tilde{\zeta}_k(t_j) \exp(i2\pi \Delta F t_j), \qquad (6)$$

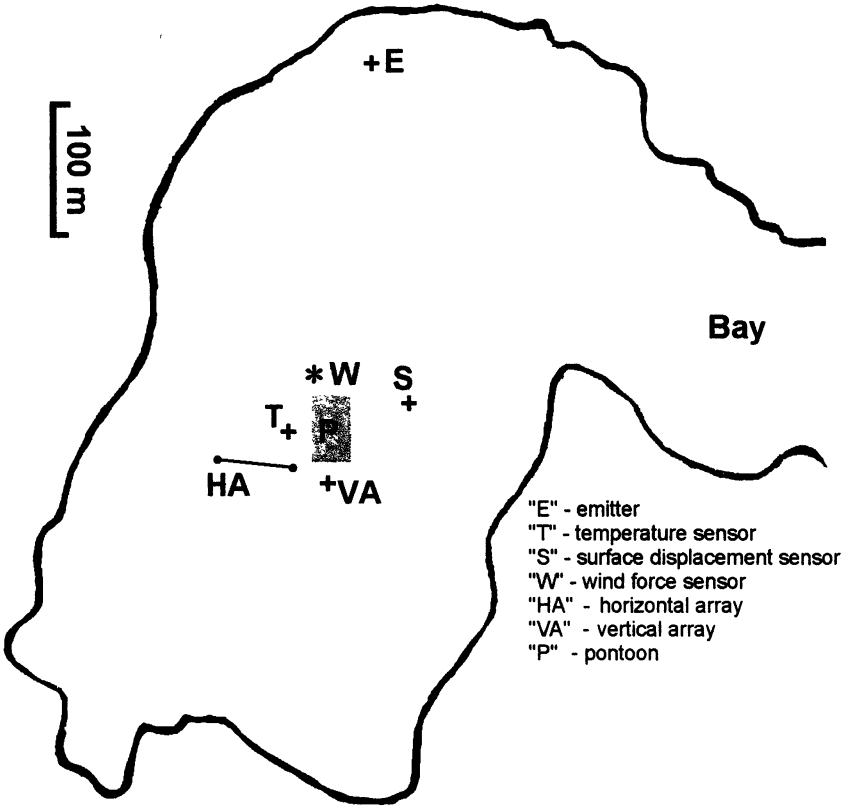

Fig. 1. Scheme of measurements in the Sankhar lake. The distance between the emitter and the arrays was about 500 m.

where

$$\tilde{\zeta}_k(t_j) = \frac{1}{N} \sum_{k=1}^{N} \frac{p_k(t_j)\langle p_k^* \rangle}{|\langle p_k^* \rangle|}, \tag{7}$$

with

$$\langle p_k \rangle = \frac{1}{N_{avg} M} \sum_{j=1}^{N_{avg} M} p_k(t_j), \tag{8}$$

N_{avg} is the number of averaging; $T = N_{avg} M / F_s$ is the entire time of analysis, in our case $T = 10^m 40^s$.

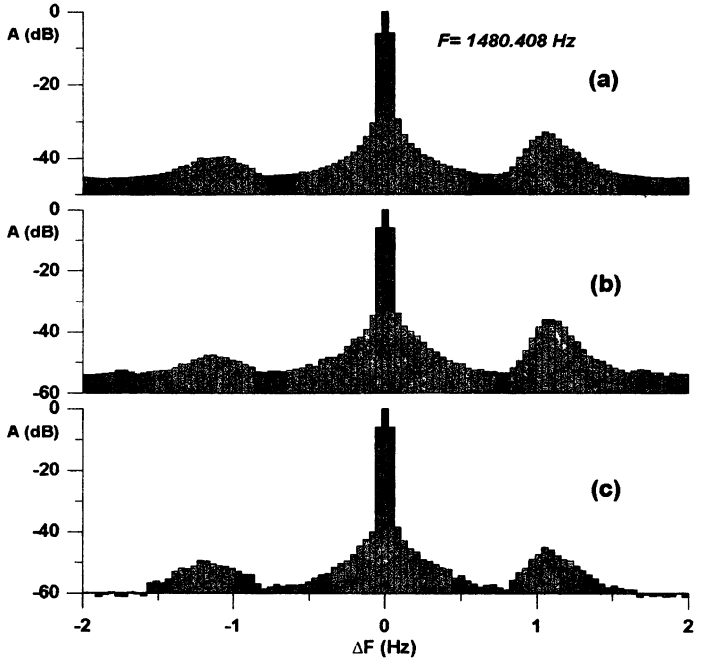

Fig. 2. Spectra of the measured acoustic signal: (a) non-coherent averaging over elements of the horizontal array; (b) focusing to the source (5); (c) focusing to the source (7). The frequency resolution is 42.057 mHz.

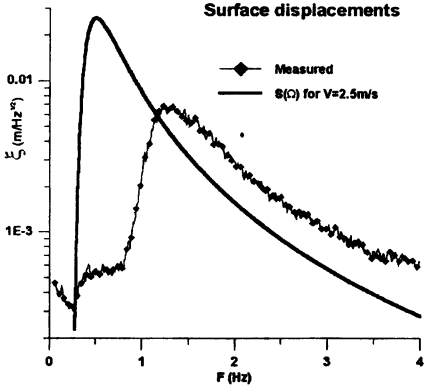

Fig. 3. Spectral distributions of surface displacements.

Looking at the spectra presented in Figs. 2, we can make the following conclusions:

1. There are "modulations" within $\Delta F = \pm 1.2$ Hz (Fig. 2a and Fig. 2c). As the corresponding levels for Fig. 2c are $\sim$ 10 dB less than for Fig. 2a, we can conclude that the "modulations" are not caused by the source-receiver direction.

2. Two frequency bands can be distinguished: (i) $|\Delta F| < 0.05$ Hz and (ii) $|\Delta F| > 0.05$ Hz. The first of them makes the main contribution to fluctuations and is associated with the line from the source to the array center (Fig. 2c).

3. The amplitude-phase distribution over the array is complex and, apparently, corresponds to additional reflections in the horizontal plane (appearance of imaginary sources) (Fig. 2b and Fig. 2c).

The spectral dependence of lake surface oscillations for the wind force of 2 m/s under which acoustic measurements were made is shown in Fig. 3. Solid lines correspond to the Pierson-Moskowitz power-law spectrum [3]:

$$\mathcal{S}(\Omega) = \sqrt{\mathcal{P}(\Omega)}, \tag{9}$$

$$\mathcal{P}(\Omega) = \mathcal{C} G^2 \Omega^{-5} \exp\left(-\frac{5}{9}\left(\frac{G}{\Omega V}\right)^4\right), \tag{10}$$

where $\mathcal{C} = 0.0081$, $\Omega = 2\pi\Delta F$, V is the wind force in meters per second, and $G = 9.8$ m/s^2 is the acceleration of gravity.

Comparing the spectra presented in Fig. 2 and in Fig. 3 we can conclude that the "modulations" within $\Delta F = \pm 1.2$ Hz are caused by oscillations of the lake surface with characteristic wavelength $\Lambda \simeq 1$ m ($\Lambda = 2\pi G/\Omega^2$ with $\Omega = 2\pi|\Delta F|$). Comparison of experimental data with Pierson-Moskowitz dependence shows that there is a qualitative difference between sea and lake environments. The energy of wind waves in lake environment is less than that predicted by theory for fully developed wind waves and the spectral maximum is high-frequency shifted. Such peculiarities of developed wind waves is well-known [4]. The wavelength of wind waves which correspond to spectral maximum in Fig. 3 in the lake is 6 times shorter than in the sea: $\Lambda_{exp} \simeq 1$ m, $\Lambda_{theor} \simeq 6$ m. Futhermore in the lake there exist oscillations with frequencies sufficiently less that 0.25 Hz $\Lambda \sim 50$ m. Such waves in the sea are absent. Thus, the first main difference between the sea and the lake environments is in wind waves spectra.

Using the data presented in Fig. 3, mean-square root displacements of the lake surface can be estimated: $\sqrt{\langle \xi^2 \rangle} \leqslant 0.007$ m. The Rayleigh parameter [2] is:

$$\mathcal{R} = \frac{4\pi F \sqrt{\langle \xi^2 \rangle} \sin \chi}{C_0}, \tag{11}$$

where χ is the sliding angle. For the carrier frequency $F = 1480.408$ Hz this parameter is equal to $0.1 \sin \chi$, that is less than unity for all χ. As the space scale of wind waves $\Lambda = 1$ m is comparable with the acoustic wavelength $\lambda = 1$ m, resonant scattering by surface perturbations is possible. This scattering is of the Bragg type:

$$\mathbf{k}_s = \mathbf{k}_i \pm \kappa, \tag{12}$$

where $\mathbf{k}_s$ and $\mathbf{k}_i$ are the wave vectors of scattered and incident waves, correspondingly and κ is the wave vector of surface perturbations.

Consider the scheme of scattering shown in Fig. 4.

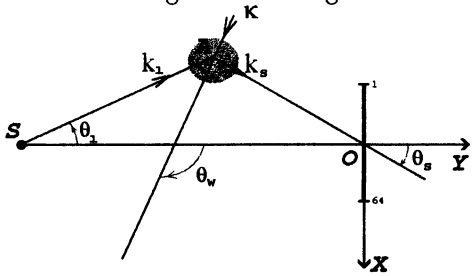

Fig. 4. Scheme of resonant scattering by the surface ($\mathbf{k}_s = \mathbf{k}_i + \kappa$). "S" is the source of radiation, "O" is the array center.

Equation (12) can be rewitten in the form

$$\cos(\theta_i + \theta_w) = \frac{k_s^2 - k_i^2 - \kappa^2}{2k_i\kappa}, \tag{13}$$

$$\cos(\theta_s - \theta_w) = \frac{k_s^2 - k_i^2 + \kappa^2}{2k_s\kappa}. \tag{14}$$

Assume that as for a sea condition resonant scattering is due to small sliding angles [2]: χ_s, $\chi_i \ll 1$. In this case $k_s \simeq k_i \simeq k_0$. Then, equations (13) and (14) are rewritten as

$$\cos(\theta_i + \theta_w) = -\frac{\lambda}{2\Lambda}, \tag{13'}$$

$$\cos(\theta_s - \theta_w) = +\frac{\lambda}{2\Lambda}. \qquad (14')$$

Resonant scattering occurs if $\Lambda > \lambda/2$, that is valid for carrier frequency 1480.408 Hz. The spatio-temporal spectrum of acoustic signal for this frequency in the horizontal array is shown in Fig. 5. The region marked as "○" depicts souce position. The regions labeled by "$\alpha - \gamma$" correspond to resonant scattering: (α) $\theta_w = 112°$, $\theta_s = 55°$ and $\theta_i = 10°$; (β) $\theta_w = 112°$, $\theta_s = -10°$ and $\theta_i = -55°$; (γ) $\theta_w = -63°$, $\theta_s = -5°$ and $\theta_i = -60°$. The spatio-temporal spectrum in Fig. 5 is averaged over 24 samples. As resonant scattering is clearly distinguished in Fig. 5, it may be due to a *regular structure* of 1 Hz surface perturbations only.

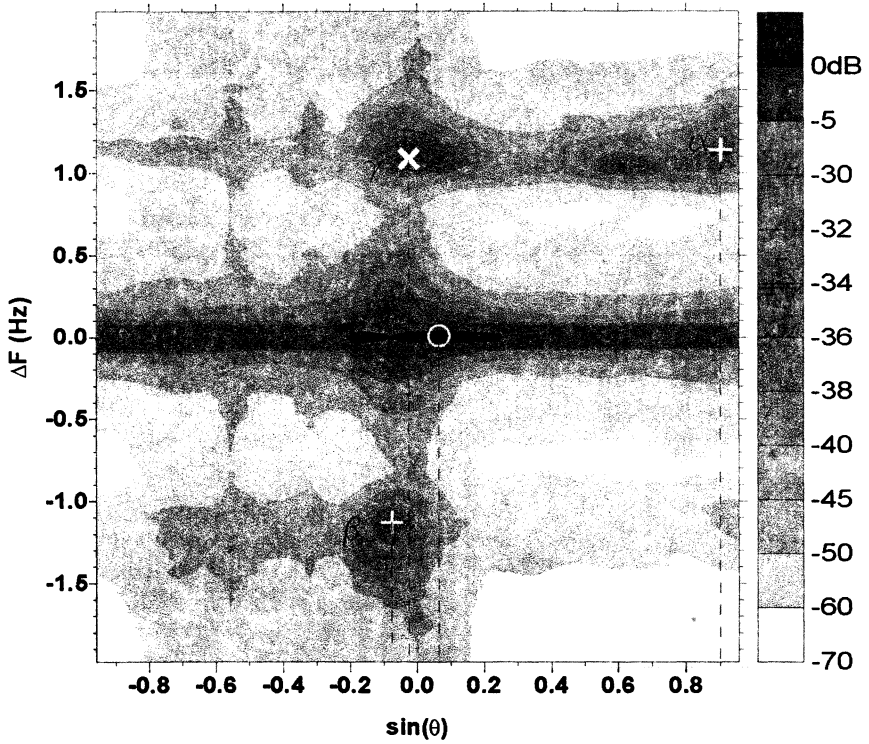

Fig. 5. Spatio-temporal spectrum of measured acoustic signal. The regions labeled correspond to resonant scattering. Source position is $\theta_0 = +5°$.

We now estimate the area of the region "A" (Fig. 4), that meets the resonant scattering condition (12). If the region "A" scatters sound waves

coherently, then the sizes of this region are equal to the sizes of the corresponding Fresnel zones:

$$L_1 = 2\sqrt{\lambda|SA|}, \tag{15}$$

$$L_2 = 2\sqrt{\lambda|AO|}. \tag{16}$$

For the carrier frequency $F = 1480.408$ Hz, the sound wavelength is $\lambda \simeq 1$ m. Using the values of angles θ_i and θ_s for region "α" (Fig. 5) we immediately obtain: $L_1 = 19.5$ m and $L_2 = 42.4$ m (The distance between the emitter and the array was about 500 m – Fig. 1), and the area of the region "A" is

$$S_{scat} \approx 830 \text{ m}^2. \tag{17}$$

Assuming cylindrical divergence and $\mathcal{R} \ll 1$ (small perturbations) we can write down relative intensity of the scattered field.

$$\frac{\mathcal{I}_s}{\mathcal{I}_i} = \frac{16\pi^4|SO|}{9H\lambda_0^2}\langle\zeta^2\rangle \sin^6\chi_\star, \tag{18}$$

where $\chi_\star = \arccos(c_0/c_b)$ is the critical angle [2], c_b is the sound speed in the bottom. For a sand $c_b \simeq 1800$ m/s and $\chi_\star \simeq 34°$. Using data presented in Fig. 6 one can determine that 90% of total power is localized within $|\chi| \leq 35°$, that is in a very good agreement with the value expected: $|\chi| \leq \chi_\star$.

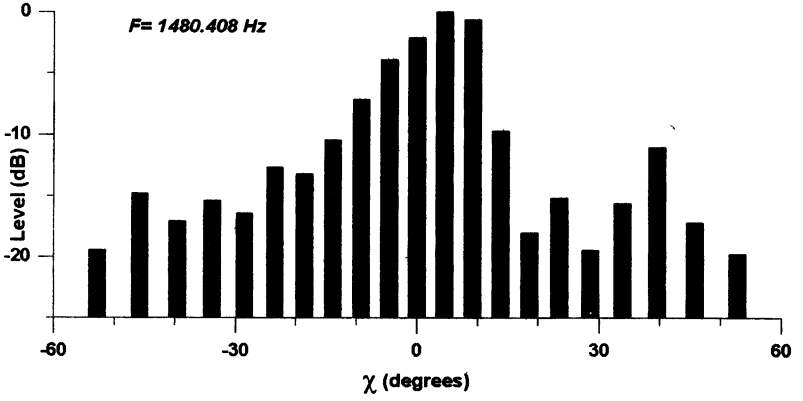

Fig. 6. Spatio-temporal spectrum on vertical array.

Simple estimations give the following level: $\mathcal{I}_s/\mathcal{I}_i = -22$ dB. Integration of measured values (Fig. 2a) over frequencies $\Delta F = 0.5 \div 2$ Hz gives $\mathcal{I}_s/\mathcal{I}_i =$

−25 dB. This value is closed to estimated one. Thus, we can conclude that the 1 Hz modulations of the acoustic signal observed in experiment were really due to *coherent* scattering of Bregg type.

CONCLUSION

After analysis made in this paper we can conclude that:

1. Wind waves in a lake environment differ from those in a sea environment mainly by spectral characteristics.

2. Surface perturbations in a lake environment are regular and resonant scattering of sound by surface is clearly seen. Due to it the direction of wind waves can be determined using acoustic measurements.

ACKNOWLEDGMENTS

This work would have been impossible without great efforts of a large team of skilled experimenters. The authors are grateful to Vladimir Tyutin, Vyacheslav Pikalev, Alexander Balalaev and Andrey Potapov for their well-coordinated work when experiments were made. We also thank Alexander Chashin for the electronic equipment design and Alexei Tsiberev, the leading programmer, for data acquisition. Hydrophysical data would not have been available without the temperature and wind wave sensors that were made by Vladimir Bredikhin and Vyacheslav Papko, we also thank them for their help. Pavel Korotin made a substantial contribution by coordinating parts of experimental investigations. The authors are grateful to all of them.

This work was partly supported by the Russian Foundation for Basic Research (RFBR) grants № 96-02-19460, № 96-02-17555 and by Contract № B012966/DB between GEC-Marconi Ltd. (United Kingdom) and Institute of Applied Physics of the Russian Academy of Science (Nizhny Novgorod, Russia).

REFERENCES

1. Flatte S. M., Dashen R., Munk W. H., Watson K. M. and Zachariasen F. *Sound Transmission Through a Fluctuating Ocean*, Cambridge U.P., Cambridge, England, 1979.

2. Brekhovskikh L. M. and Lysanov Yu. P. *Theoretical Foundations of an Ocean Acoustics*, Leningrad, Gidrometeoizdat, 1982 [in Russian].

3. Pierson W. J. and Moskowitz L. "A proposed spectral form for fully-developed wind seas based on the similarity theory of S. A. Kitaigorodsky", J. Geophys. Res. 1964, **69**, №24, P. 5181–5190.

4. Phillips O. M., The Dynamics of the Upper Ocean, second edition, Cambridge University Press, 1977.

PARAMETER ESTIMATION FOR UPPER LAYERS OF MULTI-LAYERED BOTTOM IN SHALLOW SEA

V. P. Antonov, V. V. Borodin, G. N. Kuznetsov, A. A. Kuz'menko, V. P. Tebyakin

This paper contributes to reconstruction of the bottom structure in a shallow sea, that is, to estimation of a number of layers, their thicknesses, and acoustic parameters: sound speed, density, and attenuation. This problem has practical-purpose applications in searching for mineral resources at a shelf, in laying pipelines, in mounting drilling platforms. The two latter applications require the bottom to be reconstructed up to small depths – tens or hundreds of meters, the strength parameters of the bottom, which are determined by the density and compressibility, being of primary interest in this case. Experiments show that an ordinary echo-sounder, with a carrier frequency of about 12 kHz, can "see" such shallow depths: even in deep ocean, it may yield a number of layers and their thickneses (in ms) up to a depth of 150 m. However, one cannot determine the acoustic parameters of the layers with the echo-sounder. On the other hand, there are many theoretical and experimental works [1–3] on reconstruction of the physical bottom model at low frequencies. By using low frequencies, one can reconstruct the bottom for larger depths – up to several kilometers, low-frequency sensing however requiring high-cost and bulky sound sources and receivers to be used. In addition, the low-frequency resolution is insufficient to estimate parameters of thin upper layers.

Here we consider the problem of bottom reconstruction up to small depths where rather high frequencies are optimal, the acoustic equipment being less expensive and bulk in this case but, in contrast to ordinary echo-sounding, yielding quantitatively all acoustic parameters of the sea floor.

Consider a mathematical statement of the problem. For the shallow sea, we specify a model that includes a water layer with the known sound speed profile $c(z)$, a system of N water-like layers with unknown sound speeds $c_i(z)$ and densities $\acute{n}_i$, i=1,...,N , and an underlying elastic half-space with unknown velocities of longitudinal c_l and transverse c_t waves and density $\acute{n}$. To be specific, we suppose that there are linear depth dependencies of the sound speeds $c_i(z)$ within the water-like layers. For sensing the medium, a ship-towed sound-transmitting system is supposed to be used that emits complex signals of some periodicity and period-to-pulse duration ratio. The signals are received by an

antenna array of pressure sensors, the array being fixed or ship-towed. Figure one shows the sketch of the experiment.

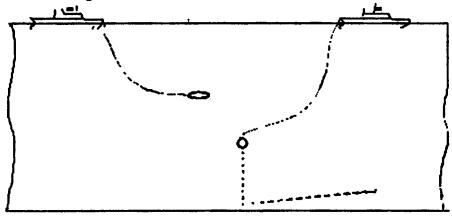

Fig. 1. Sketch of experiment no.1.

Thus, for each act of sounding, the model of measurements may be formulated as

$$p(x_s,t)=p_N(x_s,t)+\int_{-\infty}^{t} G(x_s,x_0,t-\tau)\,s(\tau)\,d\tau \quad ,t\in(0,\tau), \quad s=1,\ldots,N_R.$$

With this model, by supposing that the receiving aperture is in Fresnèl or Fraunhofer zone for the μ-th ray congruency, the Green function may be specified in the ray approximation, and the solving statistics may be written in the form:

$$T(p|x_0)=\frac{\left|\sum_{\mu=1}^{M}A_\mu(x_a,x_0)\sum_{s,r=1}^{N_R}K_N^{-1}(x_s,x_r,\omega_0)\,q\left(x_r,t_\mu(x_a,x_0)+\frac{(\vec{e}_\mu,d_s)}{c}+\frac{1}{2c}(æ_\mu d_s,d_s)\right)\right|^2}{\sum_{\mu,\nu=1}^{M}A_\mu A_\nu\sum_{s,r=1}^{N_R}K_N^{-1}\,r\left(t_\mu+\frac{(e_\mu,d_s)}{c}+\frac{1}{2c}(æ_\mu d_s,d_s)-t_\nu-\frac{(e_\nu,d_r)}{c}-\frac{1}{2c}(æ_\nu d_r,d_r)\right)}. \quad (1)$$

Here $q(x_s,t)=\sum_{\omega_n>0}p(x_s,\omega_n)e^{-i\omega_n t}s^*(\omega_n)$ is the cross-correlation function between the signal of the s-th receiver and the sounding one, $\omega_n=\frac{\pi n}{T}$, $r(t)=\sum_{\omega_n>0}|s(\omega_n)|^2 e^{i\omega_n t}$ is the auto-correlation function of the sounding signal, K_N^{-1} is the inverted matrix of the cross-spectral densities for the noise, M is the number of rays joining the points of transmission x_0 and reception x_s, $A_ξ$ is the amplitudes of signals, $t_ξ$ - the ray arrival times, x_a are the coordinates of the array phase center, $d_s=x_s-x_a$, $\vec{e}_\mu(x_a,x_0)$ is the unity vector that is tangent to the μ-th ray at the array phase center, but $æ_\mu(x_a,x_0)$ is the curvature matrix for the μ-th ray congruency at the array phase center.

The apparatus that implements expression (1) must include the Fresnel-compensation device and a unit that executes correlation with the sounding signal.

In seismometry, phase relations between different receivers are often neglected, and only arrival times are used. In this case, the solving statistics takes the form:

$$T_1(p \mid x_0) = \sum_{s=1}^{N_R} \frac{1}{\mathbf{K}_N(\omega_0)} \frac{\left| \sum_{\mu=1}^{M} A_\mu q\left(x_s, t_\mu + \frac{(\mathbf{e}_\mu, \mathbf{d}_s)}{c} + \frac{1}{2c}(\text{æ}_\mu \mathbf{d}_s, \mathbf{d}_s) \right) \right|^2}{\sum_{\mu,\nu=1}^{M} A_\mu A_\nu r\left(t_\mu - t_\nu + \frac{(\mathbf{e}_\mu - \mathbf{e}_\nu, \mathbf{d}_s)}{c} + \frac{1}{2c}((\text{æ}_\mu - \text{æ}_\nu)\mathbf{d}_s, \mathbf{d}_s) \right)}. \quad (2)$$

The algorithm that solves the inverse problem of bottom structure reconstruction consists in maximizing expressions (1) and (2) by choosing the bottom model. Upon specifying the number of layers and their acoustic parameters, one calculates ray parameters of the Green function: M, A_ξ, t_ξ, $\mathbf{e}_\xi$ and æ_ξ and substitutes them to expressions (1) and (2) to obtain the solving statistics. By exhausting the bottom parameters in accordance with a specified iteration scheme, one maximizes expressions (1) and (2), thereby finding the bottom structure parameters. Obtaining the global unbiased extremum from (1) and (2) is significantly simplified if *a priori* information on probable model parameters is known. For instance, it is advantageous to know a number of layers within the near-surface sediment domain, along with their inclinations.

In practice, the number of bottom layers may be determined with an echo-sounder if a ship-towed receiving array is used. If a fixed receiving array is used, the number of layers is to be determined by vertical sounding when the transmitting vessel passes over the array. In this case, the depth of sensing is the maximum one, most intense reflections from all layers being obtained. Thereby, the number of layers can be determined from the number of correlation peaks.

A wave-field computer code is required to determine the acoustic parameters of bottom layers. Such code, RAY225, has been developed by V.P. Tebyakin. Figures 2 and 3 show the propagation times and arrival angles versus distance between the source and receiver. The receiver is bottom-moored, the source was towed at a depth of 30 m, the distance ranging from 0 to 1 km. The density of gray color indicates the intensity of ray congruencies. Figure 2 shows the t-R and α-R diagrams computed for a frequency of 100 Hz (1 kHz in Fig. 3). Left fractions of the figures exhibit the t-R and α-R dependencies for "purely" water rays, the right ones corresponding to rays reflected from the bottom layers. Figure 2 indicates a "rich" structure of the bottom-reflected rays: even twice reflected

ray congruencies can be noticed because of low sound absorption in bottom layers at 100 Hz. At a frequency of 1 kHz (Fig. 3), the structure of bottom reflections is much "poorer": absorption in the layers is significantly higher. In addition, the figures show that the *t-R* and α-*R* diagrams are different for the water-path and bottom-reflected rays, and correlation peaks which correspond to the bottom-reflected congruencies may be distinguished from those which correspond to the water-path ones if complex sounding signals and receiving arrays of large wave size are used.

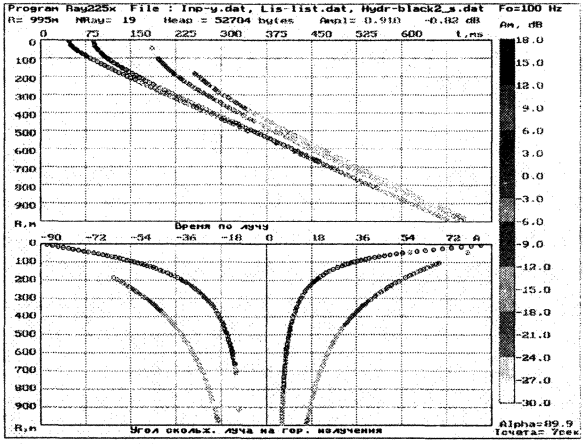

Water-path rays.

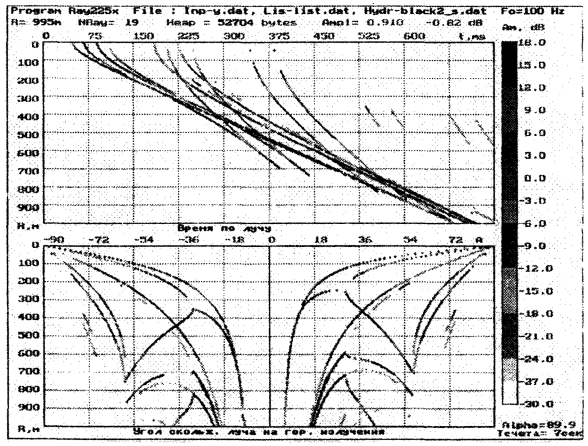

Bottom-reflected rays.

Fig. 2. *t-R* and α-*R* diagrams for water-path and bottom-reflected rays, 100 Hz, 0–1000 m.

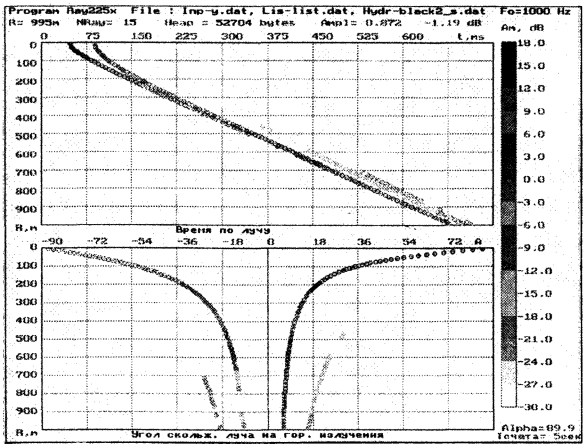

Water-path rays.

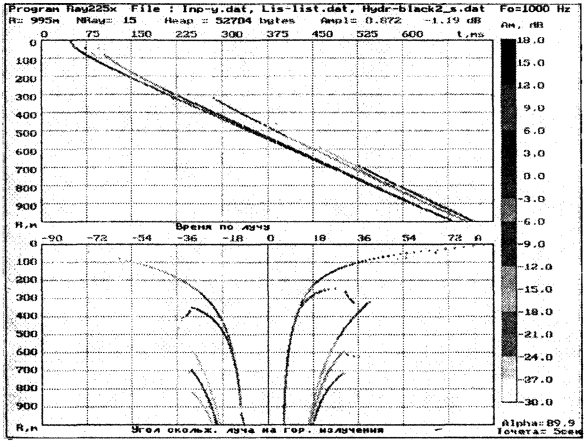

Bottom-reflected rays.

Fig. 3. *t-R* and α-*R* diagrams for water-path and bottom-reflected rays, 1 kHz, 0–1000 m.

To estimate an accuracy of determining the acoustic parameters for the bottom model, we use the Fisher information matrix which characterizes the potential accuracy in parameter estimating. The Fisher matrix has the form

$$I_{i,j}=\sum_{\omega_n>0}\left\langle K_N^{-1}(\omega_0)\frac{\partial G(\omega_n)}{\partial\lambda_i},\frac{\partial G(\omega_n)}{\partial\lambda_j}\right\rangle|s(\omega_n)|^2 \ . \qquad (3)$$

Here $\partial G/\partial \ddot{e}_i$ are the partial derivative of the Green function with respect to the parameter vector which consists of the following components: $\ddot{e}_i = \{h_1, c_1, \rho_1, \delta_1, h_2, c_2, \rho_2, \delta_2, \ldots, h_N, c_N, \rho_N, \delta_N, c_l, c_t, \rho_{el}, \delta_l, \delta_t\}$. A computer code has been developed to calculate the Fisher information matrix in view of data acquisition over passage of the ship-towed array. As an interference, sea ambient noise was used at Beauport 3 sea state. The power of transmitted signal was specified to be 50 W. The central frequencies of sounding were 0.1, 0.5, 0.75, 1.0, and 1.5 kHz. The calculations were performed for sea depth of 100 m. The sound speed profile in water is shown in Fig. 4 (on the left).

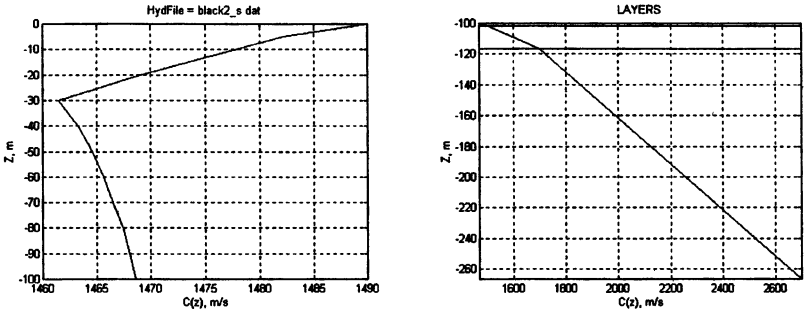

Water layer. Bottom.

Fig. 4. Sound speed dependence on depth.

The bottom model included three layers. The layer thicknesses were 1.5, 1.5, and 150 m respectively. The sound speed profile is also shown in Fig. 4 for the water-like bottom layers. The following densities and attenuation decrements were specified: $\rho_1 = 1.3$ g/m^3, $\delta_1 = 0.002$, $\rho_2 = 1.9$ g/m^3, $\delta_2 = 0.004$, $\rho_3 = 2.7$ g/m^3, $\delta_3 = 0.008$. The parameters of the elastic half-space were chosen to be $c_l = 5.5$ km/c, $c_t = 1.8$ km/c, $\rho_{el} = 3.2$, $\delta_l = 0.01$, $\delta_t = 0.01$.

Figure 5 shows rms errors of the estimated sound speeds and layer thicknesses for the mentioned three-layer bottom model, these values being plotted versus length of the transmitter passage, for different central frequencies of sounding.

For the two upper layers, higher errors were obtained at the sounding frequency 0.1 kHz. This fact is a consequence of a high level of the ambient sea noise at low frequencies, the frequency band of sounding being rather narrow (about 50 Hz), and the accuracy of estimating the ray arrival times being low. As the frequency increases, the accuracy of estimating the parameters of the first layer also increases, and the optimal frequency is close to 2 kHz. The optimal

frequencies are 1 and 0.75 kHz for the second and third layers respectively. These frequencies are governed by both decreasing the sound attenuation in the bottom and increasing the noise at low frequencies.

As the figures show, the passage length must be higher than 0.5 km to attain errors less than 1%. The error sharply falls off at 0.4 - 0.5-km spacing for all frequencies. This effect is governed by the second, surface-bottom-reflected ray that exhibits itself at this distance in addition to the "pure" bottom reflection. The second ray allows one to survey the multi-layered medium at different aspects from a single point, this effect leading to sharp drop in the estimating error.

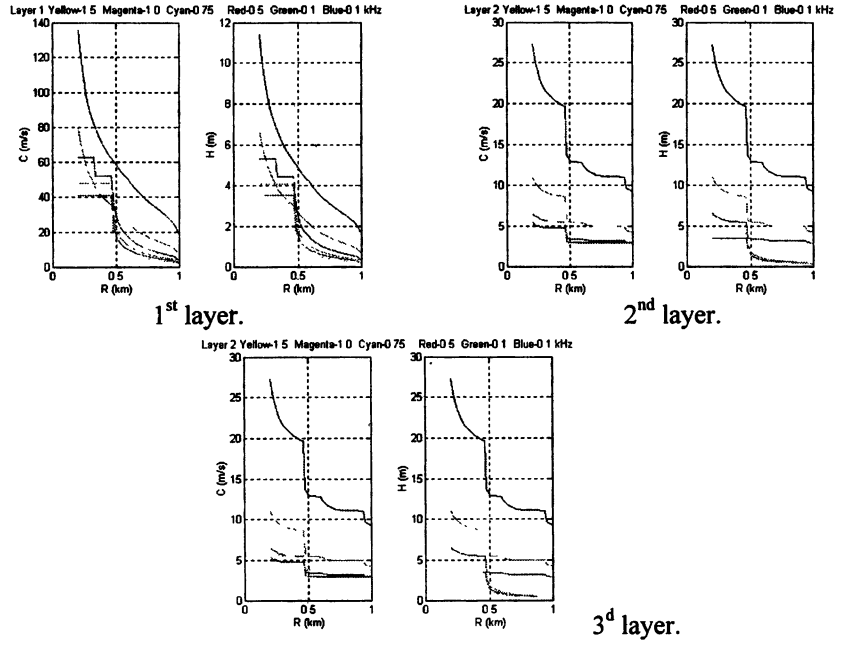

Fig. 5. Errors of measuring *c* and *h* as functions of the frequency and a number of observations.

To solve the bottom reconstruction problem, V.P. Antonov has developed a computer code that maximizes the solving statistics (1) and (2) with the use of the Nelder-Mid algorithm. The computations are illustrated in Fig. 6 where the convergence rate of the iteration process is shown. According to the plots, 20 - 25 iterations are sufficient for the estimated model-bottom parameters to converge to the actual parameter values of the layers.

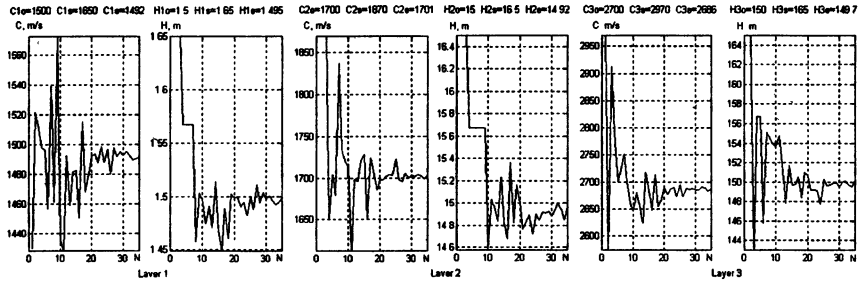

Fig. 6. Parameters c and h of the bottom model versus the number of iterations.

To increase the rate of the iteration algorithm, it is important to choose the starting approximation to the parameter vector, which is close to the actual vector value. To do so, the inverse problem may be solved for two successive positions of the transmitter relative to the receiving system. In the first position, normal incidence and reflection from the bottom layers must be implemented; the second position should be at the Fresnel zone relative to the first one. In this case, an analytic solution exists for the system of equations for sound speeds and thicknesses of the layers. This solution may serve as a starting approximation for a general iteration method to solve the inverse problem for large antenna arrays and long paths of towing, and higher convergence rate may be attained.

The developed algorithm of estimating model parameters for a shallow-sea multi-layered bottom may serve as a basis for a technique to estimate and test errors of experimental parameter reconstruction. The algorithm includes procedures of both preliminary signal processing and optimizing the solution of the inverse problem. By simulating the reconstruction procedure for various propagation conditions, required specifications of the sound source and receiver systems may be chosen.

References

1. Grachev, G. A. Redetermination of the bottom parameters at low frequencies. *Izv. Severo-Kavkazskogo nauchnogo tsentra, Vyssh. Shk., ser. Estestv. nauki*, 1983. № 1. P. 57–59.
2. S. D. Rajan, I. F. Lynch, G. V. Frisk. Perturbation – Inversion method for obtaining bottom geoacoustic parameters in Shallow Sea. *J. Acoust. Soc. Am.*, 1987. V. 82, № 3. P. 998–1017.
3. Marphy, O. Olsen. Intensity – range relation for Shallow-Water Sound Propagation, *J. Acoust. Soc. Am.*, 1976. V. 59, № 2. P. 305–311.

ACOUSTIC METHODS FOR DETERMINING BUBBLE CONCENTRATIONS IN SUBSURFACE LAYERS

S.N.Gurbatov, B.Kerman, N.V.Pronchatov-Rubtsov, O.V.Lebedev

1. THEORY OF SOUND ATTENUATION IN SUBSURFACE BUBBLE LAYERS

1.1 BASICS OF DETERMINING BUBBLE CONCENTRATIONS IN PLANE LAYERED WAVEGUIDES

Air bubbles in water significantly affect the sound propagation. It can be explained that in a wide frequency band the scattering and absorption are of resonant nature. Thus, at the resonant frequency scattering cross section of an air bubble could be more than 1000 times larger than its geometrical cross section. If the bubble concentration is rather high water compressibility changes considerably and sound velocity changes respectively. Moreover, among the all possible sound scatterers bubbles have the most clearly expressed nonlinear properties. All these facts allows to consider acoustic methods as the most adequate ones for the distant diagnostics of air bubbles.

A bubble as a resonance system can be described by its quality factor Q and natural (resonance) frequency f_0, which in adiabatic approximation [1,2] is given by expression

$$f_0 = \frac{1}{2\pi a}\sqrt{\frac{3\gamma p_0}{\rho}}, \qquad (1)$$

where a is a bubble radius, $\gamma = c_p/c_v$ - index of adiabat (in the air $\gamma = 1.4$), p_0 - pressure in a bubble in the absence of sound wave, ρ - water density. The resonant frequency f_0 of the air bubble located at the depth z can be estimated as

$$f_0 = 327/a\sqrt{1 + 0.1z}\,,$$

where f_0 is in Hz, depth z - in metres, bubble radius a - in centimetres.

If bubbles are of different sizes, their size distribution can be described by function $n(a)$. Then $n(a)da$ is the number of bubbles with sizes from a to $a + da$ in a unit volume (m^3).

For the coherent component of an acoustic field the water with air bubbles often can be treated as a continuous medium with the effective sound speed c_{eff} and with the greater absorption, which is described by the absorption coefficient in a bubble media $\alpha(\omega)$. As a rule, the density of the water with suspended air is only slightly different from the density of the water free of bubbles.

Analysis of these expressions for the variation of sound speed Δc shows that if we may neglect the variability of the distribution function $n(a)$ at the width of the resonant curve, then $\Delta c \approx 0$. So in this case the absorption is determined only by the concentration of resonant bubbles of the correspondent frequency and does not depend on their quality factor. The numerical expression for the absorption coefficient $\alpha(\ 1/cm\ )$ is

$$\alpha = \alpha(\omega) \approx 725 n(a_r) a_r^3\ , \qquad (2)$$

where a_r is the radius of resonant bubbles (cm) (their resonant frequency is $\omega = 2\pi f$) and $n(a_r)$ is expressed in $1/cm^4$.

As it follows from the previous results , the attenuation of a signal of rather high frequency f mainly depends on the concentration of resonant bubbles. If a plane wave propagates in the medium with homogeneously distributed bubbles, its amplitude decreases as

$$p = p_0 e^{-\alpha r}.$$

Thus, measuring the transmission loss (TL_p) on the path of range

$$TL_p = 20 log_{10} \frac{p_0}{p} = 10 log \frac{I_0}{I} = \alpha r 20 log_{10} e = 8.64 \alpha r \qquad (3)$$

we can find out the attenuation coefficient $\alpha = TL_p/8.64r$, and then - the concentration of resonant bubbles (see 2).

However, the problem becomes more complicated in natural waveguides. It is concerned with the finity of a bubble layer. Here the sound field has a very complex structure so the simple dependence of TL_p on attenuation coefficient $\alpha(\omega)$ fails. Because of it the diagnostics of subsurface bubble layer requires the more detailed analysis.

In this chapter we will try to show clearly the physical base of sound field attenuation in a waveguide with subsurface bubble layer and will discuss both the principal feasibility of determining the bubbles concentration and the difficulties which appear when solving the problem.

To calculate the acoustic fields of high frequency one can use the ray approach [3,4]. For the case of a layered waveguide, when the sound speed c depends only on depth z $(c = c(z))$, trajectories of rays might be calculated from Snell's law:

$$cos\chi(z)/c(z) = const\ ,$$

where $\chi(z)$ - grazing angle at a horizon z. In the framework of ray approximation the energy flows within the ray tube.

In a general case, there are some rays which might come into the point of receiver. Because of it one has to sum their amplitudes and phases to calculate the field. Due to that at the long distances the field structure becomes very complex and unsteady (small changes of sound speed profile could strongly influence on the rays phases). Thus, it is more expediently to use the averaged description.

For a plane layered waveguide the ray trajectory $z = z(r)$ has a range periodicity called ray cycle. The cycle length $D(\chi_1)$ depends also on the source depth and departure angle of the ray χ_1.

At long distances, where $r >> D$ to obtain the averaged on the cycle length intensity of the field the contribution of a ray bundle $d\chi_1$ is to be weighted by the probability that it irradiates a receiver at depth z in the course of complete cycle near range r.

In [4] there was obtained the expression for average sound field intensity:

$$\bar{I} = \frac{4}{r}\int_0^{\pi/2} \frac{E(\chi_1, r)cos\chi_1}{D(\chi_1)sin\chi(\chi_1)} d\chi_1 \,, \tag{4}$$

where $\chi = \chi(\chi_1)$ is the inclination (grazing angle) of ray at the receiver horizon and $E = E(\chi_1, r)$ - attenuation factor introduced to account for dissipation and reflection losses.

Within one cycle a ray once touches the bottom, being attenuated in $|V(\chi_h)|^2$ times in it. Here χ_h - is the ray inclination at the bottom and $V(\chi_h)$ is the reflection coefficient of the bottom.

If we consider attenuation coefficient $\alpha(z)$ to be depending on depth, then the factor concerned with dissipation within one cycle is

$$E_v = exp(-2\int_0^{l_0} \alpha(z(l))dl) \,, \tag{5}$$

where l_0 is the length of a ray trajectory.

For the path of length r the number of cycles $N = r/D(\chi_1)$ and, thus, the attenuation factor in (4) might be written as

$$E(\chi_1) = |V^2 E_v|^{r/D(\chi_1)} \,. \tag{6}$$

Expressions (4) - (6) allow to obtain the range dependence of averaged sound transmission loss in a range - independent waveguide. The generalization for a range- dependent ducts is given in [5] and is used in this work for calculation of sound field intensity.

Let's consider some particular cases of sound propagation in the isovelocity waveguide. In a homogeneous water layer with $c = c_1 = c_h = const$ the cycle length is:

$$D = 2H/tg(\chi_1)\,, \tag{7}$$

where H is a thickness of water layer - the depth of a waveguide. If $\alpha = 0$ and $|V| = 1$, then from (4) we have

$$\bar{I} = \frac{2}{Hr}\int_0^{\pi/2} d\chi_1 = \frac{\pi}{Hr}\,. \tag{8}$$

This formula shows the well known cylindrical law of field decrease. Returning to a general case we can rewrite the expression for average intensity in the following form :

$$\bar{I} = \frac{2}{Hr}\int_0^{\pi/2} A(\chi_1)d\chi_1\,, \tag{9}$$

$$A(\chi_1) = \frac{2HE(\chi_1, r)cos\chi_1}{D(\chi_1)sin\chi(\chi_1)}\,. \tag{10}$$

Here factor A is a factor which accounts both the effects of attenuation and the effects, concerned with variability of sound speed, i.e. with stratification. It might be seen, that for the isovelocity homogeneous waveguide with $\alpha = 0$ and $|V| = 1$ factor $A = 1$.

Expressions (4), (9) describe an average intensity of acoustic wave in a volume near the point of receiving which is positioned at a distance r from the transmitter at the depth z. In real conditions the averaging over the volume is substituted by the averaging over the time of narrow-band noise signal. The spectrum width of such a signal is chosen to provide the averaging of interference structure.

Let the bubble concentration $n(a)$ and, consequently, the absorption coefficient depends only on depth. Then, as it can be easily seen from (2),the integral

$$m = \int_0^H \alpha(z)dz\,, \tag{11}$$

is proportional to the amount of resonant bubbles in a water volume below the square unit of the surface

$$M = \frac{4}{3}\pi a^3 \int_0^H n(a, z)dz\,, \tag{12}$$

Integral $\int_0^\infty M(a)da$ is in this case is the gas volume in that water volume.

Below we will be using m as it is expressed in (11). It is equal to the integral decrement of absorption of the ray propagating vertically through the depth of waterbody.

As it can be seen, the problem of determination of volume void fraction leads to the problem of evaluation of integral m (11) using the measured average intensity $\bar{I}$ (9). This quantity is determined in a very complicated way by the depth distribution of the absorption coefficient. In general, the problem is mathematically incorrect and there is no solution for an arbitrary $\alpha(z)$.

We will consider the cases when the reconstruction of integral void fraction which is proportional to the integral decrement of absorption can be carried out in principle.

Practically, we have no precise information on hydrology (the depth dependence of sound velocity, bottom properties). That is why the possibility of solving the inverse problem of reconstruction of integral absorption using the loss function in the absence of information on the hydrology of waterbody will be considered.

In the second part the homogeneous bubble distribution in a layer of constant depth h will be considered. In Chapter 2 we presume that all parameters of bubble layer are explicitly determined by the wind velocity. This parameterization of bubble distribution leads the integral problem to the determination of functional dependence of average intensity on a single parameter (absorption coefficient in first case, wind speed - in another).

Thus, in a first case there is a functional dependence $\bar{I} = \bar{I}(\alpha)$ and by solving this equation with respect to $\alpha = \alpha(\bar{I})$ we can practically determine measuring $\bar{I}$.

It is more convenient, though, to consider the relative signal attenuation induced by subsurface bubble layer

$$\Delta TL(\alpha) = -10log_{10}\frac{\bar{I}(\alpha)}{\bar{I}(\alpha = 0)}, \qquad (13)$$

where $\bar{I}(\alpha = 0)$ - the average field intensity in the absence of bubbles which can be measured in calm.

1.2 INFLUENCE OF INDEFINITY OF WAVEGUIDE ACOUSTIC PARAMETERS ON THE ACCURACY OF MEASUREMENTS OF BUBBLE INDUCED ATTENUATION

Now let's consider the homogeneous bubble layer of thickness h and constant absorption coefficient α near the surface. We will be considering the dependence of losses on the absorption coefficient for different hydrologies supposing the thickness of bubble layer being the same.

First we consider the isovelocity water layer settled down on a liquid bottom without absorption ($c_b > c_1$), then one can introduce the critical angle χ_*, which might be calculated from Snell's law:

$$cos\chi_* = \frac{c_1}{c_b}\ ,\ \chi_* \approx \sqrt{\frac{2\Delta c}{c_b}}\ . \tag{14}$$

Here c_b - is the sound speed in the bottom and $\Delta c = c_b - c_1$. If the angle of ray inclination at the bottom $\chi_h = \chi_1 < \chi_*$, then $|V| = 1$, otherwise V becomes less. Taking into account the fact that for $r/D \gg 1$ the number of ray reflections is great, obviously, the rays which leave the source at the angles $\chi_1 > \chi_*$ are being attenuated almost completely (see 6). It allows to change the upper limit of integration in (9) from $\pi/2$ to χ_* (if, for instance, $c_b = 1580m/s$ and $c_1 = 1420m/s$, then $\chi_* \simeq 0.47$).

From Fig.1 it is seen that within one cycle attenuation factor is

$$E_v = e^{-2\alpha S_*} \doteq e^{-4\alpha h/sin\chi_1}\ , \tag{15}$$

where $S_* = 2h/sin\chi_1$ - the length of the ray cycle part within the bubble layer. Then (10) might be rewritten as follows (for the isovelocity waveguide):

$$A = exp\left[-\frac{2\alpha hr}{Hcos\chi_1}\right] \approx exp\left[-\frac{2\alpha hr}{H} - \frac{\alpha hr\chi_1^2}{H}\right]\ . \tag{16}$$

Here we took into account that the main contribution is being made by the rays of angles $\chi_1 < \chi_*$.

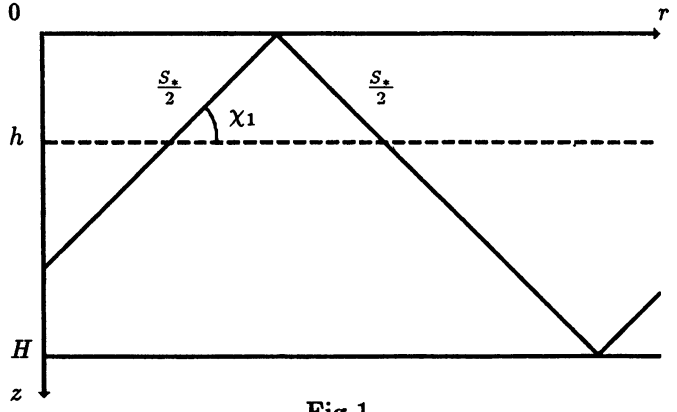

Fig.1

From (16) we can make the important conclusion, that at small angles of inclination A does not depend on χ_1. The reason is that for the rays with $\chi_1 \ll 1$, S_* is rather great, but the number of cycles is small. And these effects compensate each other.

There are two main effect concerned the attenuation in a thin bubble layer. The first is the decrease of amplitudes of all the rays: they decreases as $exp(-2\alpha hr/H)$. And the second one is the narrowing of angle spectrum up to $\chi_{bbl} = \sqrt{H/\alpha hr}$. If $\chi_{bbl} \gg \chi_*$ we can neglect this effect, and then from (8), (16) one can obtain the following expressions for averaged intensity and transmission loss:

$$\bar{I} = \frac{2}{rH}\chi_* e^{-2\alpha hr/H} , \tag{17}$$

$$TL = 10log_{10}\frac{I_0}{\bar{I}} = TL_0 + 8.64\frac{\alpha rh}{H} = TL_0 + \Delta TL . \tag{18}$$

Here $TL_0 = 10ln(rH/2\chi_*)$ transmission loss in the waveguide free of bubbles and the second item describes the additional losses due to the bubble layer. From the comparison of this expression with TL_p for the homogeneous bubbly media (3) it is seen that for such a layer TL is less in h/H times. The reason is that only the part of a ray trajectory goes through a bubble layer. It must be mentioned, that additional loss are proportional to the quantity of bubbles along all the path.

It is convenient to depict the dependence of additional losses, induced by appearance of subsurface bubble layer on the attenuation as a function of losses for plane wave ΔTL_p:

$$\Delta TL_p = TL_p\frac{h}{H} = 8.64\frac{\alpha rh}{H} . \tag{19}$$

In these variables the functional dependence $\Delta TL(\Delta TL_p)$, which corresponds to (13) becomes linear :

$$\Delta TL(\alpha) = \Delta TL_p. \tag{20}$$

It means that by measuring of additional losses it is easy to determine ΔTL_p and, consequently, the absorption coefficient.

The expression (17) was obtained under the assumption that one can neglect the narrowing of field angle spectrum due to the stronger attenuation of rays of steep angles. In this approximation $\bar{I}$ does not depend on χ_*, i.e. on the sound speed in bottom c_b. That is why possible errors in determination of sound velocity in bottom does not affect the precision of determination of attenuation coefficient.

We have assumed above that for angles less that the critical one χ_* the bottom reflection coefficient $|V| = 1$ and the narrowing of angle spectrum was neglected. In an absorbing bottom for small angles of ray inclination V can be approximated as

$$|V_h(\chi)| = 1 - S\chi \approx e^{-S\chi} , \tag{21}$$

where coefficient S depends on sound velocities in water and in bottom and on attenuation coefficient in bottom. From (6),(7) and (10) it is easy to obtain the expression for A:

$$A(\chi) = e^{-2\alpha hr/H} e^{-\chi^2(\alpha hr/H + Sr/H)} . \tag{22}$$

As it can be seen from (22), the absorption in subsurface layer leads both to the lowering of general level of angle distribution of intensity and to the narrowing of angle spectrum. Using (9) and (22) the average intensity might be rewritten as follows

$$\bar{I} = \frac{2}{rH}\chi_* e^{-2\alpha hr/H} F , \tag{23}$$

$$F = \sqrt{\frac{\pi}{2\chi_*((1+\alpha h/S)Sr/H)}}\, erf(\chi_* \sqrt{(1+\alpha h/S)Sr/H}) .$$

Here $erf(x) = 2/\sqrt{\pi}\int_0^x exp(-t^2)dt$ - error function, which has the following asymptotics :

$$erf(x) = \begin{cases} \frac{2}{\sqrt{\pi}} x(1 - \frac{x^2}{3}) & , \quad x \ll 1 \\ 1 - \frac{e^{-x^2}}{1+0.5x} & , \quad x \gg 1 \end{cases} \tag{24}$$

For additional losses ΔTL due to the of subsurface bubble layer using (23) one can write the following expression:

$$\Delta TL = \Delta TL_p + 10log_{10}\left[\frac{erf(\chi_* \sqrt{Sr/H})\sqrt{1+\alpha h/S}}{erf(\chi_* \sqrt{Sr/H(1+\alpha h/S)})}\right] . \tag{25}$$

As it can be seen, the relation between the additional losses ΔTL and the absorption coefficient α becomes more complicated when taking into account the effects of absorption in bottom and the narrowing of angular spectrum. But the main problem is that parameters χ_* and S defined by bottom properties as usual are not known precise enough. But still the situation is not so doomed for the isovelocity waveguide, especially when considering the relative error δ in determination of attenuation coefficient :

$$\delta = \frac{\Delta\alpha}{\alpha} \simeq \frac{\Delta TL - \Delta TL_p}{\Delta TL_p}. \qquad (26)$$

In (26) we assume that as an estimation we calculate α using expression(20), which is valid for the bottom without absorption. Then $\Delta\alpha$ is an absolute error in determination of the absorption coefficient calulated by the exact expression. As it follows from (25), the relative error δ is always relatively small ($\delta < 5\%$), and it decreases as the absorption coefficient α grows.

All that leads us to the conclusion that the determination of α can be carried out rather successfully for the isovelocity waveguide. In this case one can use the simple approximate expression (20) to estimate absorption.

In an arbitrary case to compute averaged intensity (4) analytically seems to be impossible, so one has to do it numerically. Some results are presented below. The calculation has been made for the following model of waveguide : the path length is $20km$, sound speed in bottom $c_b = 1580m/s$, sound speed in water at the bottom $c_h = 1420m/s$ (critical angle $\chi_* \approx 0.47 \approx 28°$), depth of the waveguide $H = 100m$. Two models of bottom has been used: half-space without and with losses (the imaginary part of the refraction index $\eta = 0.008$). Model of the bubble layer: thickness $h = 6m$, absorption coefficient $\alpha = 0.0025$. (For the case of the waveguide with homogeneously distributed bubbles, i.e. $h = H$, the bubble induced loss would be $432dB$ - see (18)).

At Fig.2 angle distribution of factor A is shown for bottom without (a) and with (b) absorption. As it might be seen from these figures, for this case the effect is clear: all the rays radiated reach the subsurface bubble layer and are attenuated in it, so it leads to the decrease of signal level. It is remarkable, that in an isovelocity waveguide the introducing of the bottom absorption leads to general decrease of signal level approximately on $5dB$, but almost does not affect the bubble layer induced attenuation value ($\Delta TL \approx 26dB$ in both cases). This result is in a good agreement with (18). Calculating ΔTL from (18) one can find that the bubble induced attenuation in the case of layer thickness $6m$ is less than for homogeneously distributed bubbles in $h/H = 0.06$ times.

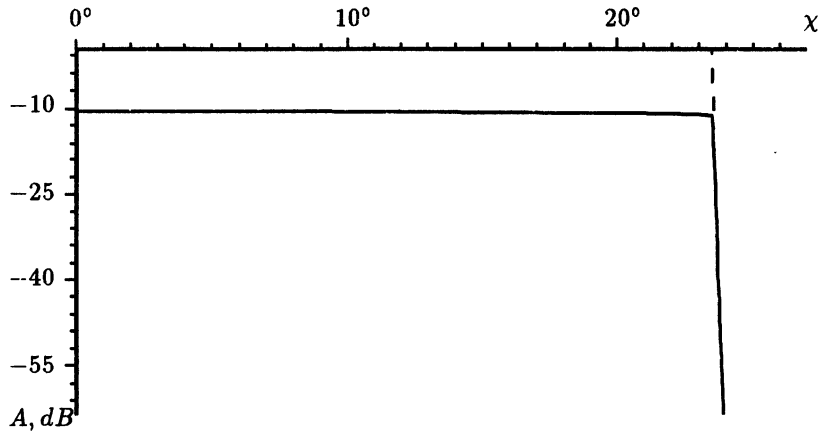

Fig.2(a) Factor A as a function of departure angle of ray in a isovelocity waveguide without absorption in bottom.

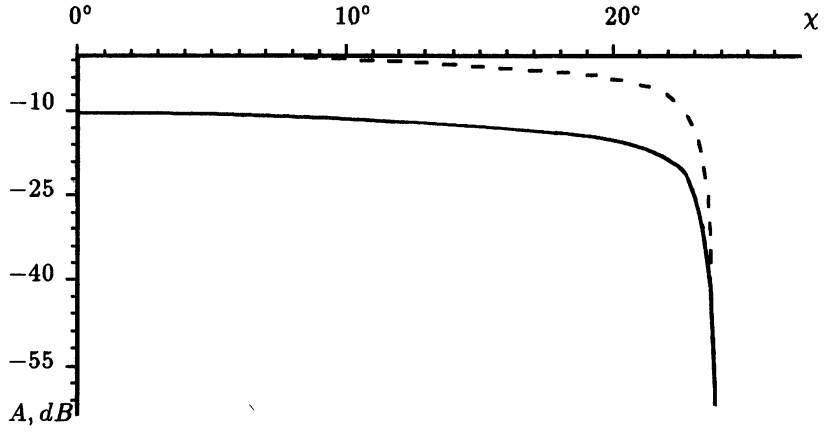

Fig.2(b) Factor A as a function of departure angle of ray in a isovelocity waveguide with absorption in bottom.

In arbitrary case the problem of determination of absorption coefficient is reduced to solving of the equation (13) or in the new variables (19) to solving of the equation

$$\Delta TL = \Delta TL(\Delta TL_p) \tag{27}$$

with respect to ΔTL_p. In the isovelocity waveguide this dependence becomes linear (20) for small absorption coefficients. In Fig.3 this

dependence is depicted for a isovelocity waveguide for unabsorptive (dashed line) and absorptive (solid line) bottom. At Fig.4 the corresponding graphics for δ (26) are depicted. It is seen that in the isovelocity waveguide the situation looks rather suitable for the determination of absorption coefficient.

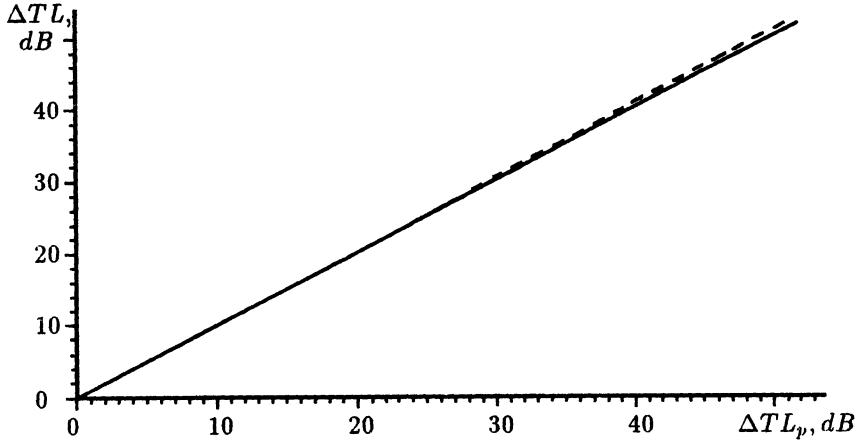

Fig.3 Additional losses ΔTL as a function of ΔTL_p for a isovelocity waveguide.

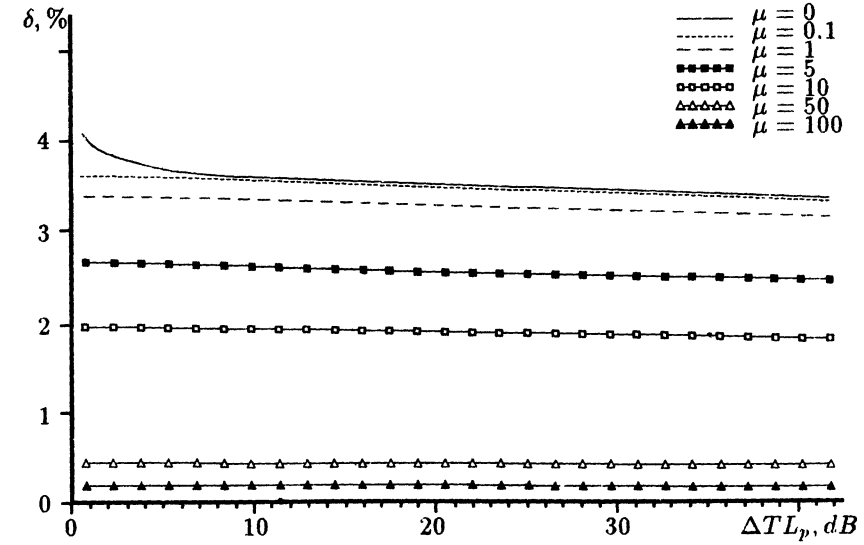

Fig.4 Relative error in determining bubble concentration as a function of ΔTL_p for a isovelocity waveguide ($\mu = \alpha hr/H$).

In a case of "summer" profile of sound speed the picture seems to be more complicated (Fig.5(a)). As it is seen from Fig.5(b) there are three groups of rays (A factor for these rays presented on Fig.6(a),(b) for both models of bottom): **A** - the rays of small grazing angles, which do not reach the bubble layer; **B** - the rays, which reach the layer but don't touch the surface - their inclination at the bound of bubble layer is small and because of it the attenuation of these rays is great; **C** - the rays reflected by the surface.

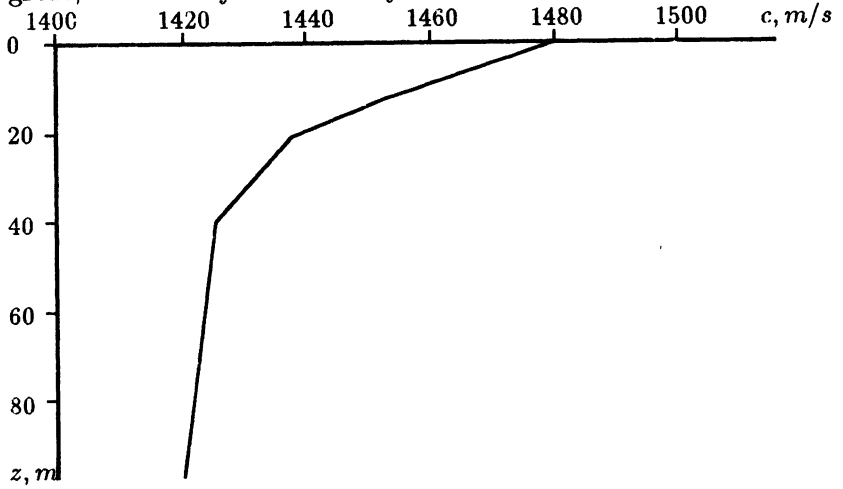

Fig.5a Sound speed profile in a "summer" waveguide.

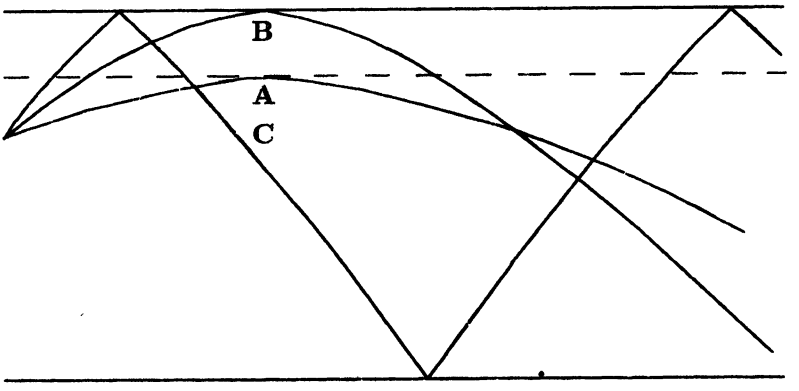

Fig.5b Ray trajectories in a "summer" waveguide.

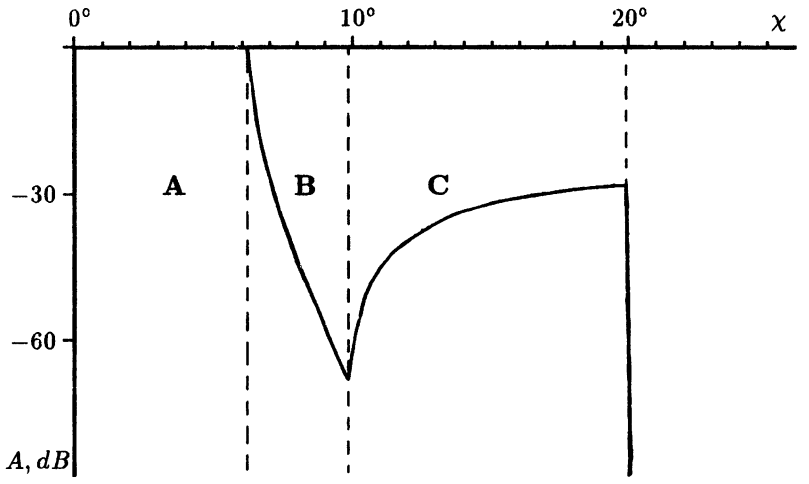

Fig.6a Factor A as a function of departure angle of ray in a "summer" waveguide without absorption in bottom.

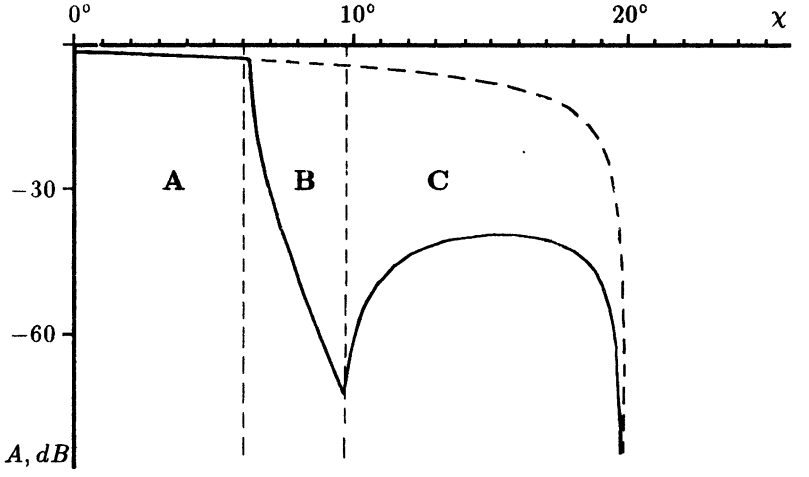

Fig.6b Factor A as a function of departure angle of ray in a "summer" waveguide with absorption in bottom.

It is seen, that the influence of bottom absorptivity is significant and at rather great values makes the the bubble induced attenuation to be hardly distinguished. Obviously, this effect is concerned with the fact that all the rays which reach the bubble layer have a great

inclination at the bottom and due to it are strongly attenuated there. So their contribution to the averaged field intensity is less than for the bottom without absorption. For unabsorptive additional losses due to the bubble layer $\Delta TL \approx 6dB$, and for the bottom with absorption $\Delta TL \approx 2dB$.

In Fig.7 the calculated dependence of ΔTL on effective absorption coefficient ΔTL_p for the unabsorptive bottom (dashed line) and the bottom with absorption (solid line). As it can be seen, the dependence $\Delta TL(\Delta TL_p)$ has a "satiation" at large absorption coefficients. Moreover, there exists rather strong dependence on the bottom properties.

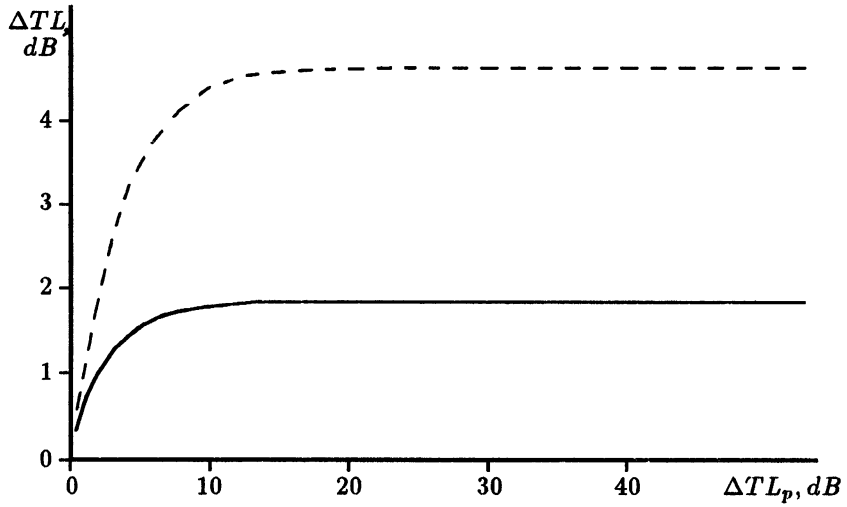

Fig.7 Additional losses ΔTL as a function of ΔTL_p for a "summer" waveguide.

This result can be explained qualitatively using the simple model. Let us divide all rays into two groups. The first type of rays which does not graze the bubble has an summary intensity A. The second type of rays go through the bubble layer and their intensity can be approximated as $Bexp(-\alpha_e r)$. The average intensity of such a signal can be written qualitatively as

$$I = A + Be^{-\alpha_e r}, \tag{28}$$

where α_e is some effective absorption coefficient. In this case from (28) one can obtain the following expression for the function of relative losses :

$$\Delta TL = -10log_{10}\frac{A + Be^{-\alpha_e r}}{A + B} . \quad (29)$$

If almost all the rays graze the bubble layer ($B >> A$), then from (29) there follows a simple relation between ΔTL and α which is valid in a rather wide range ($exp(-\alpha_e r) >> A/B$). That means that in this case the problem of determination of absorption coefficient α can be effectively solved.

In the opposite case, when only a small fraction of energy-carrying rays grazes the bubble layer, from (29) we have

$$\Delta TL \approx -10log_{10}(1 + \frac{B}{A}(e^{-\alpha_e r} - 1)) \approx$$
$$\approx -10log_{10}(e\frac{B}{A}(e^{-\alpha_e r} - 1)) . \quad (30)$$

From this expression it is seen that for small absorption coefficients

$$\Delta TL \approx 8.64\frac{B}{A}\alpha_e r .$$

It means that there exists a simple relation between α_e and ΔTL, but the coefficient of proportionality strongly depends on the hydrology. And when the absorption coefficient α is large, the ΔTL "satiates":

$$\Delta TL \approx 8.64\frac{B}{A} .$$

It significantly complicates the problem of determination of the absorption coefficient in "summer" conditions.

2 INFLUENCE OF BUBBLES ON SOUND ATTENUATION IN PLANE LAYERED WAVEGUIDES

2.1 WINDSPEED DEPENDENCE OF SOUND ATTENUATION IN A ISOVELOCITY CHANNEL

In this part we will use another parametrization of bubble concentration assuming that it is completely determined by the wind speed. In paper [6], basing on the results of [7,8], it was shown that the concentration of bubbles $n(\alpha)$ which appears due to the sea surface agitation may be parameterized and written as

$$n(\alpha) = N_0 G(a,z)\chi(U)Y(z,U)\,, \tag{31}$$

where U is the wind speed in m/s (its basic value was U=13 m/s), z - depth (m),

$$Y(z,U) = exp(-\frac{z}{L(U)})\,, \tag{32}$$

$$L(U) = \begin{cases} 0.4 & , \quad U \le 7.5m/s \\ 0.4 + 0.115(U - 7.5) & , \quad U > 7.5m/s \end{cases}$$

$$N_0 = 1.6 \times 10^2 cm^{-4}\,,\ \chi(U) = (U/13)^3\,,$$

$$G(a,z) = \begin{cases} (a/a_1)^2 & , \quad a < a_1 \\ 1 & , \quad a_1 \le a \le a_2 \\ (a_2/a)^{d(z)} & , \quad a > a_2 \end{cases} \tag{33}$$

and the limit bubble sizes a_1 and a_2 are expressed as

$$\begin{aligned} a_1 &= (34 + 1.24z) \times 10^{-6}(m)\,, \\ a_2 &= 1.6a_1\,, \\ d(z) &= 4.37 + (z/2.55)^2\,. \end{aligned} \tag{34}$$

Thus, using (31) and measuring the transmission loss at different frequencies it might be possible in some cases to solve the inverse problem - to reconstruct the size distribution. Then, one of the questions appearing is the feasibility of parameterization for the size distribution $n(a)$ of subsurface bubbles in inner lakes.

In the framework of this model the bubble concentration near the surface is proportional to U^3 and at the wind speeds $U > 7.5m/s$, the thickness of bubble layer begins to increase. Taking an integral over z we obtain the bubble size distribution at a square unit of surface, and by integrating over size a with the factor $4/3\pi a^3$ a we obtain the volume void fraction at the square unit of surface. It is obvious, that all these quantities are completely determined by the wind speed U and in this case the problem is reduced to to the determination of effective wind speed using the measured transmission loss ΔTL. Then, using the parametrization (31) - (34) it is easy to reconstruct all parametres of bubble layer.

In this part to compute an average intensity of acoustic field we will use the computer program which is based on the method of adiabatic invariant. This method is described in Appendix. The program for computation was enhanced and now it takes into account

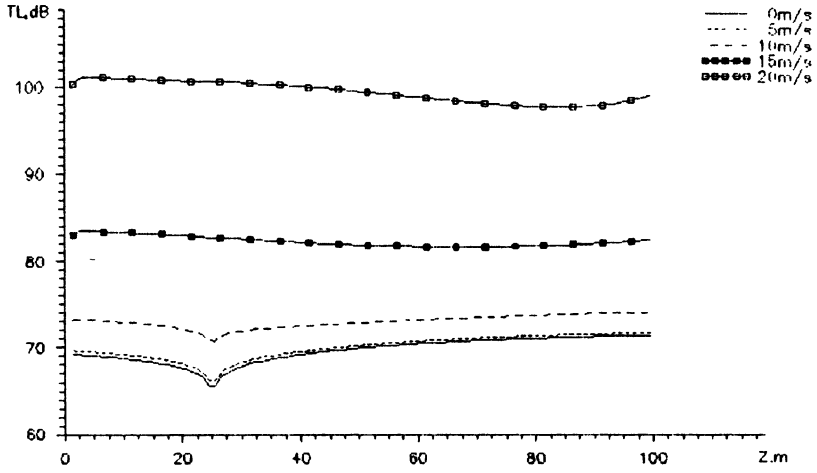

Fig.10 Transmission loss as a function of receiver depth z at different wind speed values for a isovelocity waveguide model. Source frequency $f = 1kHz$, source depth $z_0 = 25m$, range $r = 20km$.

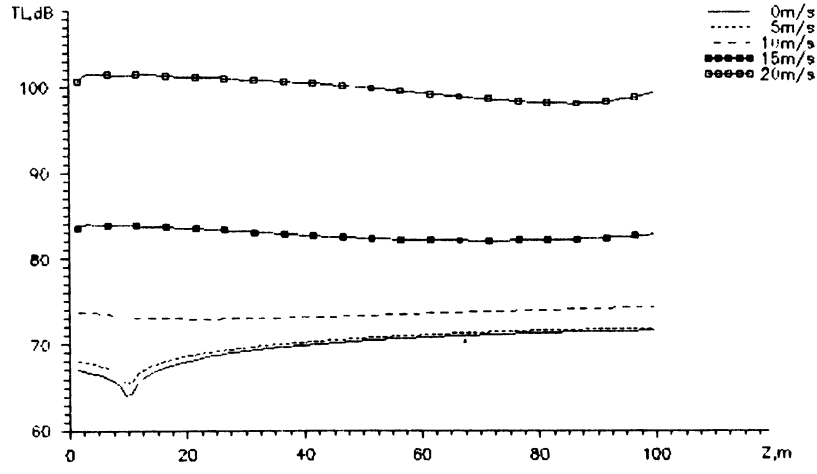

Fig.11 Transmission loss as a function of receiver depth z at different wind speed values for a isovelocity waveguide model. Source frequency $f = 1kHz$, source depth $z_0 = 10m$, range $r = 20km$.

2.2 INFLUENCE OF LOCAL CHANGES OF HYDROLOGY ON TRANSMISSION LOSS IN A ISOVELOCITY WAVEGUIDE AND WIND SPEED DEPENDENCE OF TRANSMISSION LOSS IN "SUMMER" CONDITIONS

As it follows from the results above there exists the principial possibility to determine the effective wind speed U (and, coreresponding-ly, the parameters of a bubble layer) measuring transmission loss along a path. But the loss function is extermely sensitive to changes in the waveguide's hydrology. In order to prove it, let us consider the sound propagation in channel with the slightly heated (the temperature deviation at the surface is $1°C$) thin subsurface layer. There the sound speed near the surface is $1422.3m/s$ (previously $1417.9m/s$), at depth $5m$ - $1418.1m/s$, and below this depth coincides with a typical isovelocity hydrology. The wind speed dependence of losses $TL(U)$ for this model is shown in Fig.12. In Fig.13 the wind speed dependence of bubble induced attenuation $\Delta TL(U)$ is shown in a double logarithmic scale.

Comparing Fig.8, 9 with Fig.12, 13 it is seen, that the presence of a slightly heated layer of a thickness only $5m$ leads to the significant change of additional losses at the horizon $z = 75m$. Such a strong sensitivity might be understood if we pay attention to the dependence of transmission loss on receiver depth (Fig.14-17).

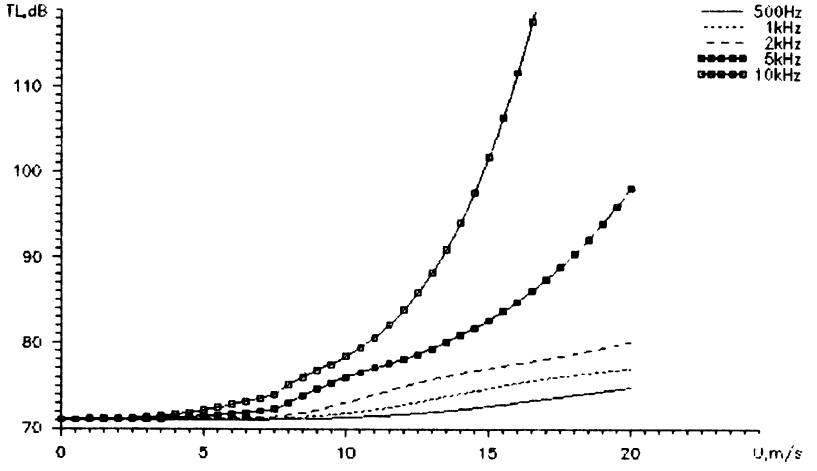

Fig.12 Transmission loss as a function of wind speed U at different frequencies for a isovelocity waveguide model with slightly heated subsurface layer. Source depth $z_0 = 25m$, receiver depth $z = 75m$, range $r = 20km$.

the absorption in a subsurface bubble layer, which is described by the absorption coefficient $\alpha(z)$ related to the bubble concentration by the expression (2). The line-broken approximation of the absorption coefficient was used in computation.

Below we discuss the results of computations of a wind speed dependence of losses TL for the range-independent waveguide of a depth 100 m at the path 20 km long.

A typical isovelocity profile (sound speed at the surface - $c = 1417.9 m/s$ and near the bottom - $c = 1421.4 m/s$) was chosen for modeling of sound propagation during winter months. This is a weakly expressed subsurface waveguide channel where all rays reach the surface and are nearly linear.

In Fig.8 the dependence of losses on the wind speed $TL(U)$ is shown for five frequencies f (0.5, 1, 2, 5, 10 kHz). In Fig.9 the wind speed dependence of bubble induced attenuation is depicted in double logarithmic scale. It can be seen from Fig.9 that $\Delta TL \simeq U^3$ at $U < 7.5 m/s$ and $\Delta TL \simeq U^4$ for $U \gg 7.5 m/s$, i.e. in this case additional losses due to bubble layer are determined by the integral void fraction at the square unit of the surface.

$$m \sim \int_0^\infty \alpha(z) dz \sim N_0 \chi(U) L(U) \,. \tag{35}$$

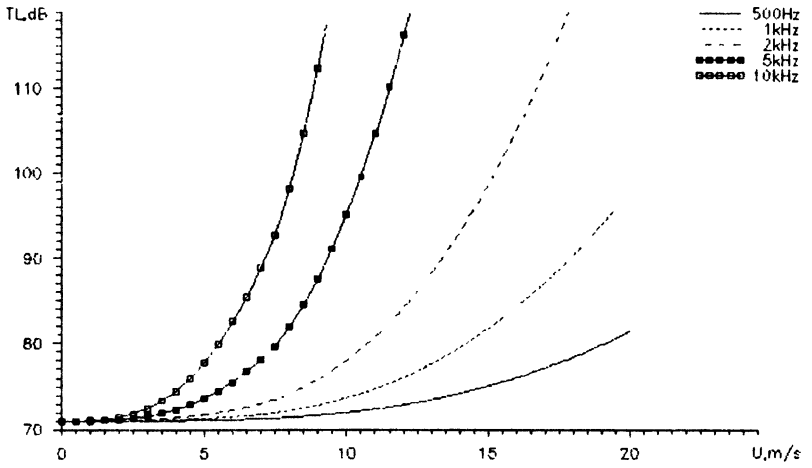

Fig.8 Transmission loss as a function of wind speed U at different frequencies for a isovelocity waveguide model. Source depth $z_0 = 25m$, receiver depth $z = 75m$, range $r = 20km$.

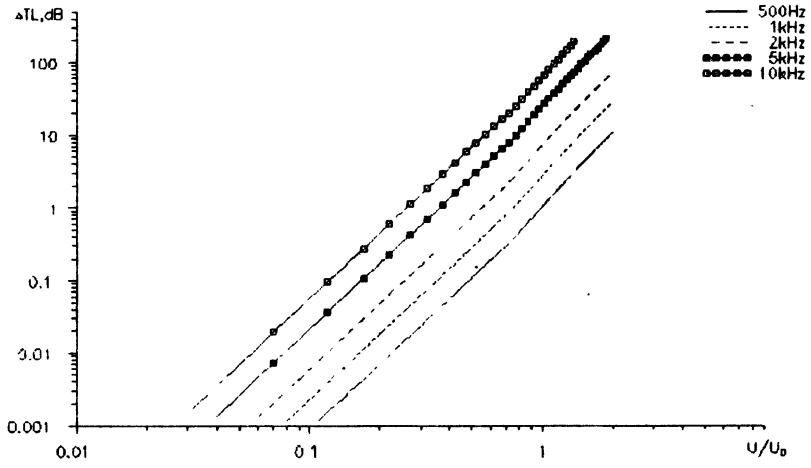

Fig.9 Additional loss as a function of wind speed U at different frequencies for a isovelocity waveguide model. Source depth $z_0 = 25m$, receiver depth $z = 75m$, range $r = 20km$, basic wind speed value $U_0 = 10m/s$.

From these figures it is seen, that for high wind speeds ($U > 10m/s$) it is reasonable to use relatively low frequencies $f < 2kHz$, since in this case bubble induced attenuation is not too big (less than 50 dB at $U < 20m/s$) and, simultaneously, is sensitive to the wind speed. For small wind speeds it is better to use high frequencies.

In Fig.10, 11 the dependence of transmission losses TL on receiver depth z at the frequency $f = 1kHz$ is presented for various wind speeds (source depths $z_0 = 25m$ and $10m$). One can conlude from these figures that bubble induced attenuation depends weakly on the position of source and receiver. This result can be explained if we take into account the fact that in isovelocity conditions all rays reach the surface and the influence of a subsurface bubble layer on the attenuation of signal level is almost equal at all horizons. The singularity at the depth $z = z_0$ is due to the behaviour of a ray focusing factor and is beyond the computation precision of ray approach.

Thus, in isovelocity conditions transmission loss function is rather sensitive to the appearance of subsurface bubble layer and the use of the frequency band $0.5kHz - 10kHz$ allows to consider the whole range of wind speeds we are interested in ($3 - 20m/s$).

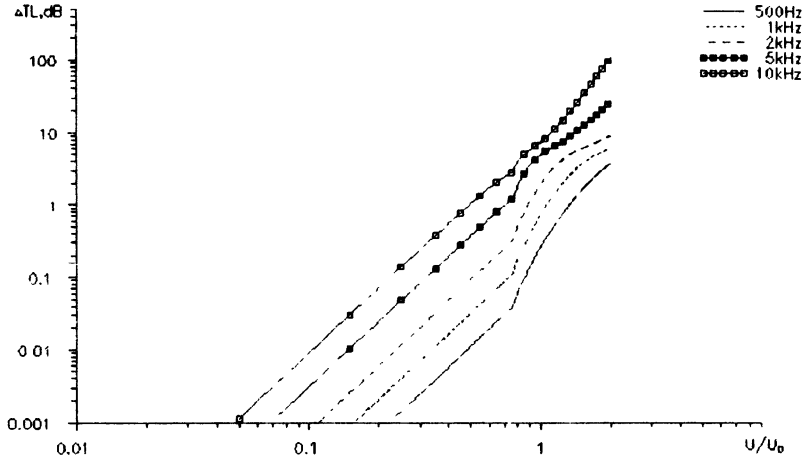

Fig.13 Transmission loss as a function of wind speed U at different frequencies for a isovelocity waveguide model with slightly heated subsurface layer. Source depth $z_0 = 25m$, receiver depth $z = 75m$, range $r = 20km$, basic wind speed value $U_0 = 10m/s$.

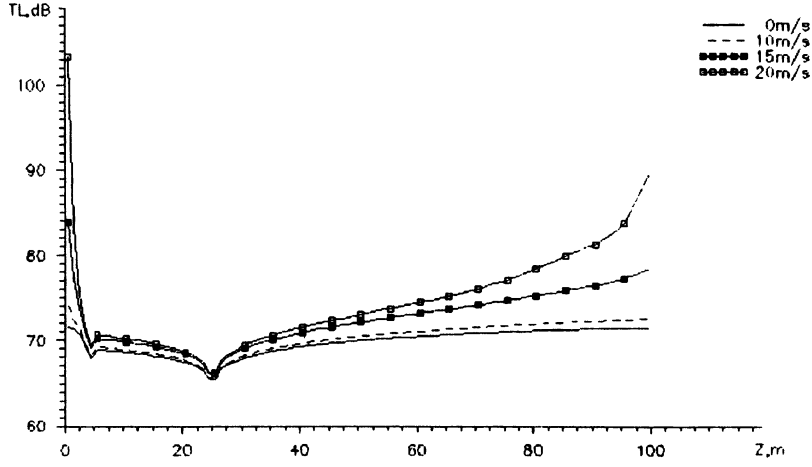

Fig.14 Transmission loss as a function of receiver depth z at different wind speed values for a isovelocity waveguide model with slightly heated subsurface layer. Source frequency $f = 1kHz$, source depth $z_0 = 25m$, range $r = 20km$.

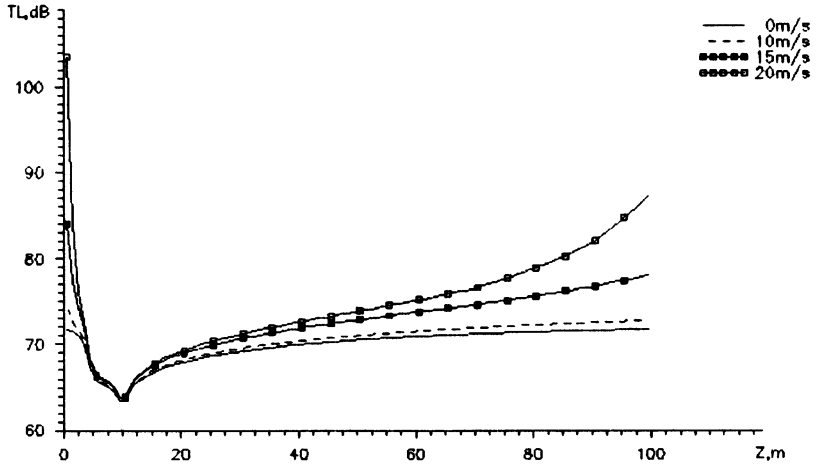

Fig.15 Transmission loss as a function of receiver depth z at different wind speed values for a isovelocity waveguide model with slightly heated subsurface layer. Source frequency $f = 1kHz$, source depth $z_0 = 10m$, range $r = 20km$.

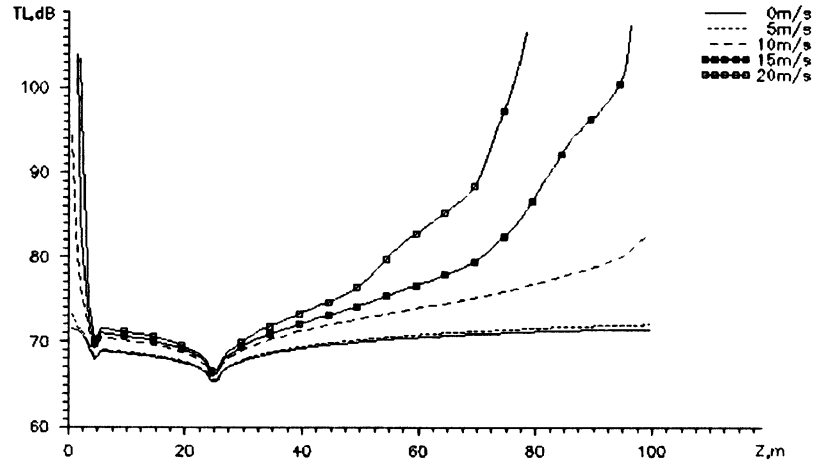

Fig.16 Transmission loss as a function of receiver depth z at different wind speed values for a isovelocity waveguide model with slightly heated subsurface layer. Source frequency $f = 5kHz$, source depth $z_0 = 25m$, range $r = 20km$.

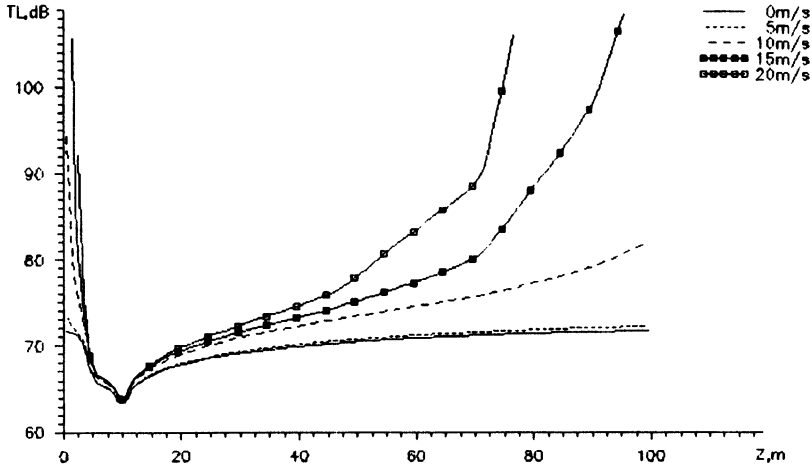

Fig.17 Transmission loss as a function of receiver depth z at different wind speed values for a isovelocity waveguide model with slightly heated subsurface layer. Source frequency $f = 5kHz$, source depth $z_0 = 10m$, range $r = 20km$.

It is seen that if a source and a receiver are positioned at the almost same level, then the subsurface bubble layer does not practically affect signal level. It is due to the fact that at these horizons the field is determined mainly by the rays radiated at the small angles. Those rays graze the surface and are significantly attenuated in the subsurface layer, so they contribute insignificantly onto the field energy. That is why their attenuation practically does not affect the signal level at these horizons.

A bubble layer strongly affects the filed intensity near the surface. It might be explained by the fact that near the surface the field is formed by the rays which are attenuated strongly in the subsurface bubble layer. The decrease of a signal level near the bottom is explained by the existence of a waveguide channel and the field near the bottom is determined by the rays which trajectories partially go through a bubble layer.

We have demonstrated above that bubble induced attenuation is significantly sensitive to small local changes of a sound speed profile. There also exists a very strong dependence of the additional losses on the global changes of hydrology. At Fig.18, 19 the dependencies of transmission loss on a wind speed and on a receiver depth for the weak near-bottom channel are shown. This channel represents a

inverted profile with the sound speed near the surface $c = 1417.9m/$ and near the the bottom $c = 1421.4m/s$.

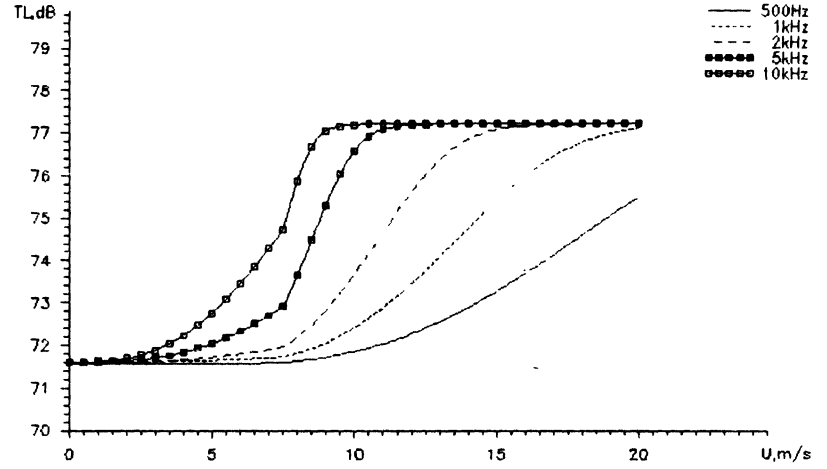

Fig.18 Transmission loss as a function of wind speed U at different frequencies for waveguide model with weakly near-bottom sound channel. Source depth $z_0 = 25m$, receiver depth $z = 75m$, range $r = 20km$.

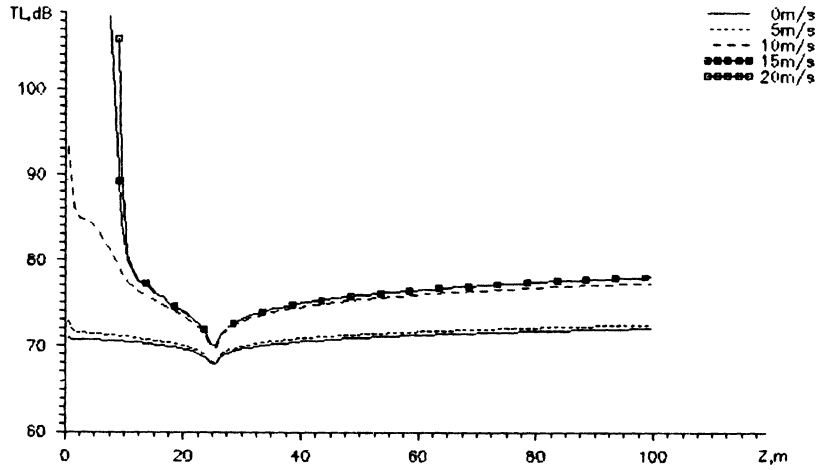

Fig.19 Transmission loss as a function of receiver depth z at different wind speed values for waveguide model with weakly near-bottom sound channel. Source frequency $f = 5kHz$, source depth $z_0 = 25m$, range $r = 20km$.

The effect of the "satiation" is worth noting. It is connencted with the fact that in a near-bottom sound channel a considerable fraction of rays never go through subsurface layer. That is why after rather strong attenuation of the subsurface rays the following increase of the sound speed does not affect signal level in any way. The qualitative theory of this phenomenon is given in the end of Chapter 1.

The problem of diagnostics of a bubble layer becomes considerably more difficult to solve in "summer" conditions. Upper layers of water are well-heated and there exists the deep sound channel. Here we present the computations for the sound speed profile depicted in Fig.5a. In a "summer" waveguide the intensity of acoustic field near the surface is low. This is due to the fact that rays, which reach the subsurface layer are of a great inclination at the bottom and so are greatly attenuated in it. At the rest part of a waveguide - in the middle and below, the field mostly is determined by rays which does not reach the subsurface layer. Because of that the diagnostics of a subsurface bubble layer by measuring transmission loss becomes siginificantly difficult. In Fig.20, 21 the dependencies of transmission loss on receiver depth z are presented for the frequency $f = 10kHz$ and wind speeds $0m/s$ and $20m/s$. At this frequency and at the wind speed $20m/s$ the bubble induced attenuation should be maximal.

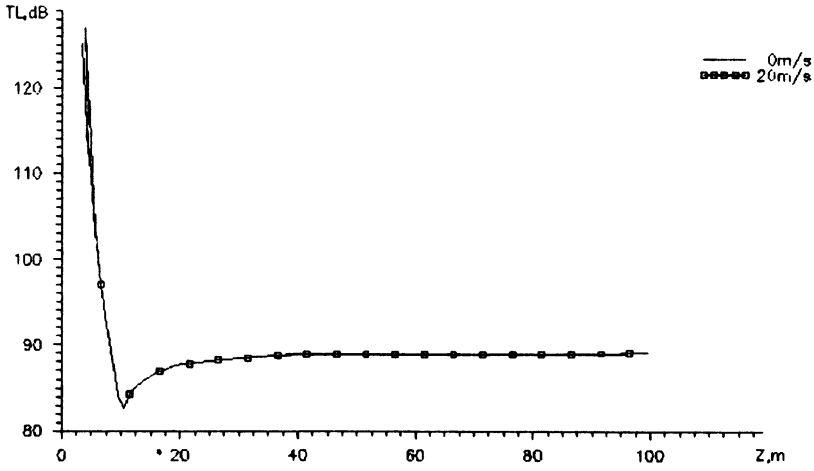

Fig.20 Transmission loss as a function of receiver depth z at wind speed values $U = 0, 20m/s$ for a "summer" waveguide model. Source frequency $f = 10kHz$, source depth $z_0 = 10m$, range $r = 20km$.

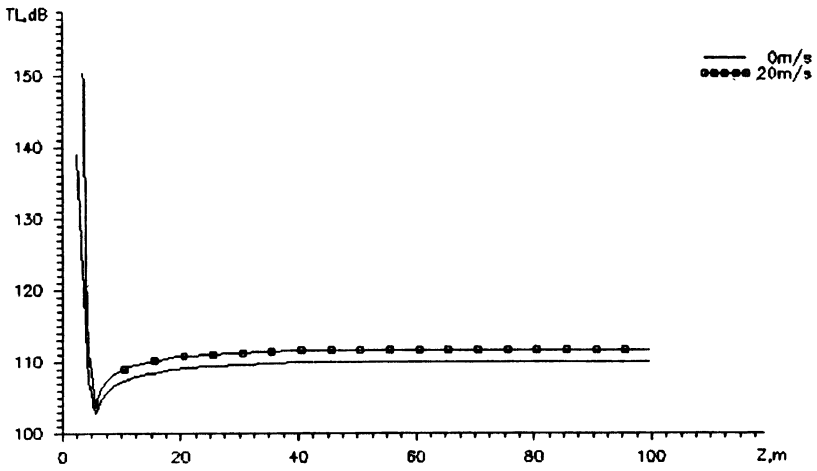

Fig.21 Transmission loss as a function of receiver depth z at wind speed values $U = 0, 20m/s$ for a "summer" waveguide model. Source frequency $f = 10kHz$, source depth $z_0 = 5m$, range $r = 20km$.

From Fig.20 it is seen, that at the receiver depth $z = 10m$ bubbles practically do not affect sound attenuation. It is explained by the fact, that in "summer" waveguide an acoustic field is formed mainly by the rays which do not reach the surface. As moving a receiver nearer to the surface ($z = 5m$) Fig.21 the intensity decreases, which is due to the greater attenuation of the rays forming acoustic field in the bottom because of their more steep angles there. Then, the intensity of a field begins to depend on the amount of bubbles in a subsurface layer. Though this dependence is very weak: at the wind speed $20m/s$ the additional losses due to bubbles are about $2dB$, which is obviously not enough to sove the problem of diagnostics.

ACKNOWLEDGMENTS

This work was supported by RFBR grants No 98-02-16402, No 96-15-96722, CCPE grant No 97-8.1-78.

APPENDIX: CALCULATION OF AVERAGE SOUND FIELD INTENSITY IN RANGE - DEPENDENT WAVEGUIDES USING ADIABATIC INVARIANT METHOD

In [4] the expressions for average intensity of sound field in plane layered waveguide are introduced within the framework of ray approach. The generalization of this approach for the range - dependent ducts might be found in [5]. There the agreement of the results

obtained from ray and wave theories is discussed as well. Below we follow these two works in general, though some details might be slightly different.

Let us consider the cylindrically symmetric waveguide with the sound speed profile $c = c(z, r)$. The sound field generated in such waveguide by point harmonic source in the adiabatic approach of normal waves method is given by [4] :

$$p(z,r) = \sqrt{\frac{2\pi}{r}} \sum_{n=1}^{\infty} \frac{\varphi_n(z_0,0)\varphi_n(z,r)}{\sqrt{\xi_n(r)}} exp\left(-i\int_0^r \xi_n(r)\,dr - \frac{i\pi}{4}\right), \quad (36)$$

where $(z_0, 0)$ - the coordinates of source, (z, r) - the coordinates of receiver, $\xi_n(r)$ - the eigenvalues, $\varphi_n(z, r)$ - the eigenfunctions.

The intensity of sound field, averaged over range r in this case is described as follows :

$$< I >= \frac{2\pi}{r} \sum_{n=1}^{\infty} \frac{|\varphi_n(z_0,0)|^2 |\varphi_n(z,r)|^2}{Re\,\xi_n(r)} exp\left(-2\int_0^r Im\,\xi_n(r)\,dr\right). \quad (37)$$

If the number of propagating modes is great and the depth dependence of wave number $k(z, r) = \omega/c(z, r)$ at any fixed range r has the only one maximum, then to find out the eigenfunctions one can use the WKB approximation [9]:

$$\varphi_n(z,r) = 2\sqrt{\frac{Re\,\xi_n(r)}{\nu_n(z,r)D_n(r)}}\, cos\left(\int_{z_n' or\ z_n''}^{z} \nu_n(z,r)\,dz + \Phi_n(r)\right), \quad (38)$$

$$D_n(r) = 2\,Re\,\xi_n(r) \int_{z_n'}^{z_n''} \frac{dz}{\nu_n(z,r)}, \quad (39)$$

$$\nu_n(z,r) = \sqrt{k^2(z,r) - (Re\,\xi_n(r))^2}, \quad (40)$$

where $z_n'(r)$ and $z_n''(r)$ - the depths, within which the normal wave is concentrated, $|\Phi_n(r)| < \pi$ - the additional phase, depending on the kind of normal wave. Substituting (38) into Eq.(37) and averaging over depths z and z_0 we obtain

$$< I >= \frac{8\pi}{r} \sum_{n=1}^{\infty} \frac{Re\,\xi_n(r)}{\nu_n(z_0,0)\nu_n(z,r)D_n(0)D_n(r)} exp\left(-2\int_0^r Im\,\xi_n(r)\,dr\right). \tag{41}$$

The real part of eigenvalues might be found from the expression for the phase integral in WKB approximation :

$$J(r) = \int_{z_n'}^{z_n''} \nu_n(z,r)\,dz = n\pi + \theta_n(r)\,, \tag{42}$$

where $|\theta_n(r)| < \pi$ - the additional phase, depending on the kind of normal wave.

Within the WKB approximation each normal wave might be considered as the system of rays :

$$Re\,\xi_n(r) = k(z,r)\,cos\chi(z,r)\,. \tag{43}$$

If the parameters of waveguide slowly varies within the ray cycle, i.e. each cycle does not strongly differs from the previous one, then for the particular ray one can suppose J to constant. (In fact, it is the condition of adiabaticity and J/ω is an ray adiabatic invariant). The assumption made allows to obtain two important conclusions. At first, using J one can link the departure angle of ray χ_0 with its angle at the horizon of receiver χ. Second, in Eq.(41) one can change the summation over n to the integration over angle χ_0 (or χ). Using (42) and taking into account (38)-(40) and (43) the following expression might be obtained:

$$dn = \frac{dJ}{\pi} = \frac{\nu(\chi_0,0)D(\chi_0,0)}{2\pi}\,d\chi_0 = \frac{\nu(\chi,r)D(\chi,r)}{2\pi}\,d\chi\,. \tag{44}$$

As a result we find:

$$< I >= \frac{4}{r}\int_0^{\pi/2} \frac{1}{tg\,\chi\,D(\chi,r)} exp\left(-2\int_0^r \beta(\chi,r)\,dr\right) d\chi_0 \tag{45}$$

or

$$< I >= \frac{4}{r}\int_0^{\pi/2} \frac{1}{tg\,\chi_0\,D(\chi_0,r)} exp\left(-2\int_0^r \beta(\chi,r)\,dr\right) d\chi. \tag{46}$$

Here

$$\beta(\chi, r) = \frac{ln|V(\chi', r)|}{D(\chi, r)} \tag{47}$$

is the loss function for bottom interacting rays, $V(\chi', r)$ is the bottom reflection coefficient, and angles χ and χ' are connected by Snell's law:

$$k(z, r)cos\chi = k(H(r), r)cos\chi' , \tag{48}$$

where r is introduced as a parameter.(The generalization of (47) for the case of bubble layer induced attenuation might be made easily). Thus, the formulae (45)-(48) allows to calculate the average sound field intensity in a range - dependent waveguide.

The description of numerical algorithm presented below requires to consider the medium of propagation. The values of sound speed $c(z_{ij}, r_i)$ at the fixed distances r_i supposed to be given on the upper $(z = 0)$ and lower $(z = H(r_i))$ boundaries and at some depths z_{ij} between (see Fig.22). To make the following computation more convenient the waveguide is divided into the space segments, using the linear interpolation both of wave number square $k^2(z, r)$ and of lower waveguide boundary $H(r)$ as it is shown at Fig.23. A segment is triangle-shaped, if one of its boundaries is the inclined bottom, and is of rectangle shape otherwise. In segments of the first kind the wave number approximation is $k^2(z, r) = a_0 + a_1 z + a_2 r$, the wave number in the second kind of segments is approximated as $k^2(z, r) = a_0 + a_1 z + a_2 r + a_3 zr$. Thus, for a fixed range r the depth dependence of wave number square is line - broken, so it allows to use the implicit expressions for computation of the integrals (39) and (42).

The bottom is represented as a structure which consists of some liquid layers upon the liquid or solid half-space. The reflection coefficient of such bottom is calculated using the recurrent relations [3].

Taking into account all the above one can calculate the transmission loss using adiabatic approach in accordance to the following algorithm.

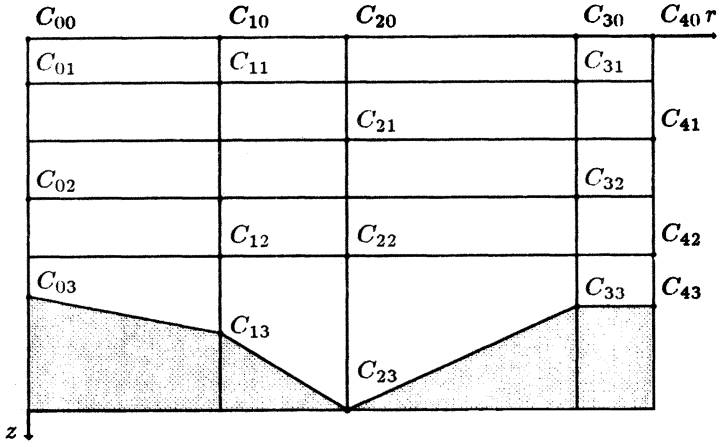

Fig.22

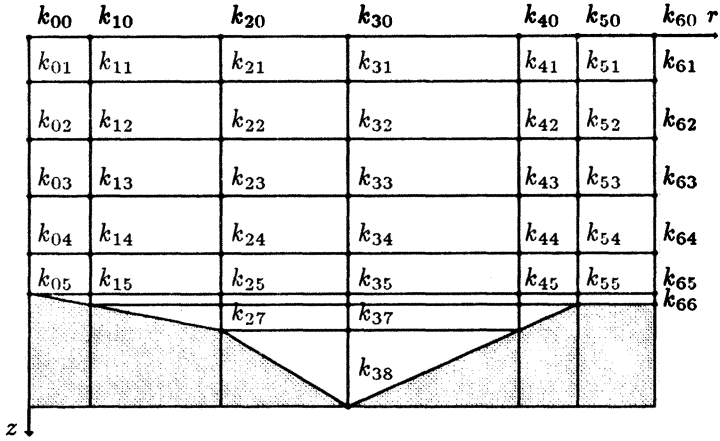

Fig.23

First, the invariant values $J(\chi_{0,l}, 0)$, the cycle lengths $D(\chi_{0,l}, 0)$ and the loss functions $\beta(\chi'_{0,l}, 0)$ for the rays which leave source at the angles $\chi_{0,l} = \Delta\chi\, l$ are to be calculated. (Here $l = 0, 1, ..., N, \Delta\chi = \chi^*/N, N+1$ - is the number of rays).

Then, for the distances $r_k = \Delta r\, k$, $k = 1, 2, \ldots$ the characteristics of rays and the sound field intensity at the receiver horizon are to be calculated. These computations are conducted as follows.

First of all, the invariants $J(\chi_m, r_k)$ of rays of inclination angles at the minimal sound speed horizon $\chi_m = \Delta\chi\, m$ $(m = 0, 1, \ldots, M,\ M = Int(\pi/2\Delta\chi))$ are calculated. If $J(\chi_m, r_k) \le J(\chi_{0,l}, 0) \le J(\chi_{m+1}, r_k)$, $0 \le m \le M - 1$, then the ray of departure angle reaches the horizon of the minimal $\chi_{0,l}$ sound speed at the angle χ_l, which might be calculated using the linear interpolation :

$$\chi_l = \chi_m + \Delta\chi \frac{J(\chi_{0,l}, 0) - J(\chi_m, r_k)}{J(\chi_{m+1}, r_k) - J(\chi_m, r_k)} \tag{49}$$

and for this ray the cycle length $D(\chi_l, r_k)$ and loss function $\beta(\chi_l, r_k)$ are to be computed. The rays for which $J(\chi_{0,l}, 0) \ge J(\chi_M, r_k)$ do not reach the range r_k so they are not considered in the following computations. Thus, the characteristics of all the rays which reach the horizon of the minimum sound speed at range r_k are determined. Integral of losses in the expression (45) is to be computed for each ray using the trapezoid rule:

$$\int_0^{r+\Delta r} \beta(r)dr = \int_0^{r} \beta(r)dr + \frac{\beta(r) + \beta(r + \Delta r)}{2}. \tag{50}$$

Then from found angles χ_l the angles at the receiver horizon might be calculated using the Snell's law (48). If the ray of departure angle $\chi_{0,0} = 0$ reaches the receiver, then the integration is made over this departure angles (45). Otherwise, the integration is to be made over the angles at the receiver horizon (46). It allows to escape the divergence of integrand. The integration of (45) or (46) are made using the trapezoid rule.

References

[1] Clay C.S., Medwin H. Acoustical oceonography: Principles and applications./ A Wiley-interscience publication. New York - London- Sydney- Toronto, 1977.

[2] Devin C. Survey of thermal, radiation and viscous damping of pulsating air bubbles in water. // J.Acoust. Soc.Amer. 1959. V. 31. N 12. P. 1654-1667.

[3] Brekhovskikh L.M. Waves in layered media. New York: Academic, 1960.

[4] Brekhovskikh L.M., Lysanov Yu.P. Theoretical fundamentals of ocean acoustics. Berlin. Springer, 1982.

[5] Smith P.W.Jr. Averaged sound transmission in range-dependent channels. // J.Acoust.Soc.Am. 1974. V.55. P.1197-1204.

[6] Hall M.H. A comprehensive model of wind-generatad bubbles in the ocean and predictions of the effects on sound propagation at frequencies up to 40 kHz. // J.Acoust.Soc.Amer. 1989. V. 86. N 3. P. 1103-1117.

[7] Thorpe S.A. On the clouds of bubbles formed by breaking wind-waves in deep.waters, and their role in air-sea gas transfer. // Phys. Trans. R.Soc. Lond. 1982. A-304, p.155-210.

[8] Jonson B.D., Cooke R.C. Bubble population and spectra in coastal waters: a photographic approach // J.Geophys. Res. 1979. V. 84. P. 3761-3766.

[9] Ahluwalia D.S., Keller J.B. Exact and asymptotic representations of sound field in stratified ocean. In: Wave propagation and underwater acoustics. / Ed. J.B.Keller, J.S.Papadakis. New York. Springer-Verlag, 1977.

ESTIMATING PARAMETERS OF SIGNAL SOURCES AND CHARACTERISTICS OF NOISE FIELD BY USING SPATIALLY SEPARATED VECTOR – SCALAR MODULES

G. M. Glebova, G. N. Kuznetsov

This paper presents a generalized approach to problems that may be solved with the use of receiving antenna arrays consisting of the vector-scalar modules.

Introduction

Measuring parameters of sources that emit vibrations and outer noise of the systems, which are located under water and incorporate many mechanical components, is a complex and important problem. It may be rather effectively solved with the use of a system of "interior" diagnosing, that is, by means of vibration and noise sensors that are close to the probable sources of intense vibrations. Then, by using statistical correlation processing for instance, one may estimate both power of the single sources and the effect of these sources on the total level of vibrations and noise [1, 2].

Nevertheless, this efficient method is not always feasible and, in principle, sufficient. To this end, in addition to or instead of interior diagnosing, exterior measuring may be carried out, that is, the noise sensors (receiving elements) may be used that are located externally to the noise-emitting system within the waveguide [3]. Such situations are common for both aero- and underwater acoustics (aviation and marine applications are meant). Recently, this problem has become urgent for monitoring the mechanical quality of oil and gas condensate pipelines, compressor and control systems, drilling installations, and so on. It is substantial that the probable noise and vibration sources are of significant spatial extent and may be distributed in both horizontal and vertical directions. For instance, a powerful source of vibrations and noise may be even located within the ground when the drill passes the elastic basic rock.

To monitor the exterior acoustic field and to perform system diagnosing by measuring the noise, one should develop a measuring instrument that incorporates an underwater multi-channel array, a transmission system for data and control signals, and a system for signal processing, visualizing, and storing.

As a rule, to analyze the noise field in both shallow and deep seas, spatially distributed multi-element arrays are used that consist of scalar pressure sensors.

Here, we consider and discuss the advantages of the spatially distributed four-component vector-scalar modules (so called pV-receivers) as applied to the problem at hand. In other words, the systems are considered that measure the three orthogonal components, - V_x, V_y and V_z, of the vibrational velocity in addition to the scalar pressure field p.

A specific measuring scheme depends on technical aspects of the problem to be solved and on conditions under which the measurements are to be carried out. Here, we propose a version of the general computing scheme with reference to both parameters of the receiving system and the waveguide transfer function for the region at hand. Obviously, such measurements are feasible only if the receiving system and waveguide are both acoustically calibrated, this being the necessary condition of creating an adequate model to compute transfer functions for the pressure and vibrational velocity fields.

As a basis for the processing algorithm, the maximum likelihood method is used that yields the optimal estimates for the measured data and/or computed parameters of the noise-emitting object. A sub-optimal method is also considered that is based on measuring the members of the covariance matrix for the signals and interfering noise (so called direct-resolution method [3]).

It is worth mentioning that we solve the problem in the quasi-stationary approximation, that is, the signal is supposed to be stationary at all receivers within the interval of primary estimation (the realization duration τ). This approach allows one to use a well-developed technique, the method being equally valid when the receiving modules and noise sources are fixed and when the receiving array is towed (or drifts) at low speed relative to the fixed noise-emitting installation or object. A large-sized vessel slowly passing over the receiving system fixed within the waveguide (or passing over it at a long range) is just the case.

Here, parameters of the noise sources are considered for a general problem statement when the source coordinates are not known *a priori* (unknown location of the condensate pipeline out-break being the example), and detecting the noise source and estimating its power and coordinates are to be performed simultaneously. For a specific case of measuring the noise field of moving vessel, the use of reference receivers is advantageous, those being fixed at known positions on the vessel and serving as reference points to measure the current distance between the vessel (noise-producing object) and the receiving vector-scalar module. In this case, coordinates of the noise source are to be redetermined relative to those of the reference source, the latter coordinates being treated as known to the required accuracy.

1. Model for measuring procedure

Two problem statements are known to be of practical interest, therefore two versions of the model for measuring procedure are considered here. Figure 1 illustrates a scheme that may be used to monitor noise levels of individual parts of a pipeline. The receiving array and pipeline are close to the sea floor and are separated by at least d = 1 - 5 km in distance. The modules are separated by l = 5 - 7 km. The receiving system and pipeline are supposed to be significantly distant from each other to simplify in-sea arranging the array and maintaining the whole system. The module outputs are digitized and cable-transmitted to the data acquisition and processing station. By signal processing, sources of increased noise are detected and located, coordinates of the sources being related to those of the pipeline.

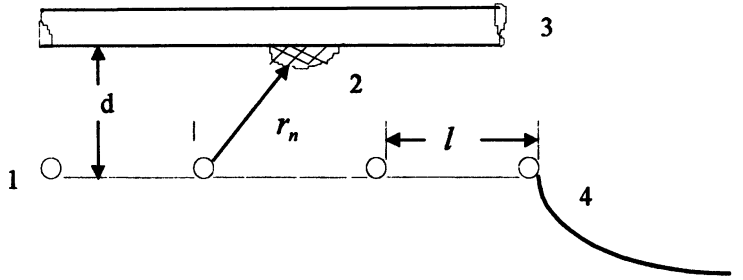

Fig. 1. Acoustic system monitors the noise field of a pipeline: 1 - vector-scalar modules; 2 - probable source location of increased noise; 3 - pipeline; 4 - transmission cable.

Later on, simulations and computations are carried out as applied to marine pipelines and acoustic systems of monitoring and diagnosing the pipeline state. Nevertheless, the general measuring scheme and processing algorithm remain nearly the same if geophones are used instead of hydrophones and the pipeline, along with the receiving system, is located in a marshy region, within ground or eternal frost.

Figure 2 shows the scheme of measurements for a situation when a multi-component distributed source *1* moves relative to the bottom-moored measuring system *2* which consists of M spatially separated vector-scalar modules. Upon being digitized *3*, the signals are cable-transmitted *4* to the data processing station *5* which may be either ship-borne or ahore-mounted.

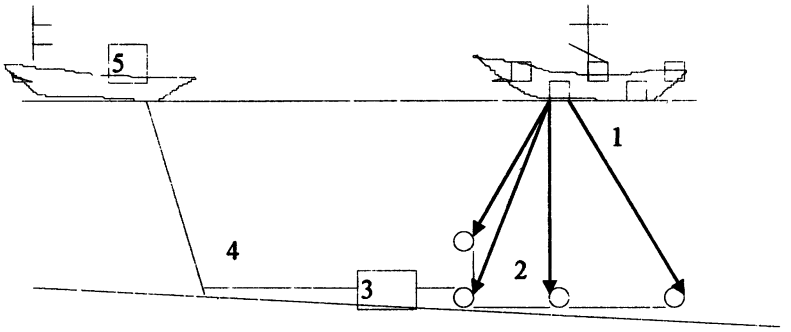

Fig. 2. Acoustic system monitors the noise field of a vessel: 1 - noise-generating vessel; 2 - receiving system; 3 - signal transmitting system; 4 - cable; 5 - data processing computer.

2. Signal and interfering noise representation

The sources are supposed to emit signals that may be treated as Gaussian noise. The source coordinates are denoted by $r_n = (x_n, y_n, z_n), (n = 1,\ldots,N)$ where N is a number of individual signal sources, x_n, y_n, z_n are Cartesian coordinates of the signal source, the coordinate origin is placed to one of the receiving modules in x,y-plane and to the sea surface in z-direction. The receiving array consists of M four-component modules located at points $r_m = (x_m, y_m, z_m), \quad (m = 1,\ldots,M)$.

The module outputs represent a total signal emitted by the sources that compose the noise-producing object and sources of the additive interfering noise which is also supposed to Gaussian. The module outputs $U_m(t)$ are entered to the computer which processes the signals and estimates unknown parameters of the sources, that is, source coordinates, their power levels, and correlation between different sources.

Information on unknown parameters of the sources is contained in the time functions $U_m(t)$ measured by the receiving modules. Suppose that the duration τ of realization is sufficiently small to neglect the signal variability (caused by receiver or source moving, for instance). For fixed sources, the transposed vector U^* may be represented as

$$U^* = U_1(\omega_1)...U_\mu(\omega_1)U_1(\omega_2)...U_\mu(\omega_2)\ldots\ U_1(\omega_I)...U_\mu(\omega_I),$$

where

$$U_m(\omega_i)=\frac{1}{\sqrt{\tau}}\int_{-\tau/2}^{\tau/2}U_m(t)\exp(-j\omega_i t)dt, \quad \omega_i=\frac{2\pi i}{\tau}, m=1,...,\mu. \qquad (1)$$

Here the m-th component of vector U, which corresponds to frequency ω_i, is the expansion of $U_m(t)$ into Fourier series within the measurement duration τ, $\mu = 4 \cdot M$. In (1), the asterisk stands for the matrix complex conjugation and transposing. The main advantage of the signal representation (1) is that the Fourier members which correspond to different frequencies do not correlate if the measurement duration τ does not exceed the correlation interval for each $U_m(t)$ and is less than the maximum cross-correlation interval, including the spatial one, for different signals.

With arrays consisting of pressure sensors, at a fixed frequency, dimensionality of vector (1) is determined by a number of receiving elements of the array: $\mu = M$,

$$U_m(p) = p_m, \quad m = 1,...,\mu \qquad (2)$$

(here and later on, to simplify the notation, we omit the frequency dependence).

With the vector-scalar modules used for measuring the sound field, the maximum dimensionality of vector (1) (at a fixed frequency) is $\mu = 4 \cdot M$ because each output of the M modules contains four measured components of the sound field: the pressure and three projections of the vibrational velocity. Thus, there are several ways to form vector U and to develop algorithms for estimating parameters of the signal sources. We propose to specify the vector of measured data in the form

$$U_k(p,V)=\begin{cases} p_m, & k=m, \\ V_{mx}, & k=M+m, \\ V_{my}, & k=2\cdot M+m, \\ V_{mz}, & k=3\cdot M+m \end{cases} \qquad \begin{matrix} m=1,\ldots,M, \\ k=1,\ldots,4\cdot M, \end{matrix} \qquad (3)$$

where p_m and V_{mr}, $(r=x,y\ z)$, are the sound pressure and projections of the vibrational velocity on the directions *x, y, z*, which are measured by the *m*-th receiving module. In general, components of vector $U(p,V)$, which is measured either at a single point or at several points, are linearly independent characteristics of signal propagation in the medium. Therefore, the jointly measured scalar and vector components yield more full and accurate description of the sound field while the form (2) is a specific case of the general representation (3). If each module measures only the three components of the vibrational velocity, the dimensionality of vector U is $\mu=3\cdot M$, and

$$U_k(V)=\begin{cases} V_{mx}, & k=m, \\ V_{my}, & k=M+m, \\ V_{mz}, & k=2\cdot M+m \end{cases} \qquad \begin{matrix} m=1,\ldots,M, \\ k=1,\ldots,3\cdot M. \end{matrix} \qquad (4)$$

This expression is also a specific case of (3).

By representing the input signals according to (3), one can generalize a well-known theory of signal detection and estimation onto receiving arrays that consist of the vector-scalar receivers. It is also possible to use the developed technique to estimate statistical properties of the noise sources at hand.

For Gaussian processes with a zero expectation, the signal statistics is fully determined by the covariance matrix whose members $\left\langle U_m(\omega_i)\cdot U_k^*(\omega_j)\right\rangle$ may be easily computed for a given model of the signal and interference. Because the Fourier components are independent at different frequencies, the members of the covariance matrix are not equal to zero if only $i=j$. For vector U corresponding to a fixed frequency, the covariance matrix has a dimensionality

of $\mu \cdot \mu$ and may be treated as a sum of the signal matrix S and the interference one Q:

$$K = \langle U \cdot U^* \rangle = S + Q \tag{5}$$

or, equivalently,

$$K_{km} = \langle U_k \cdot U_m^* \rangle = S_{km} + Q_{km}, \quad k,m = 1,\ldots,\mu . \tag{6}$$

Here $\langle \cdots \rangle$ stands for the operator of statistical averaging.

If the vector is formed according to (3) for a fixed frequency, the signal covariance matrix is the block-structured one of dimensionality 4·4:

$$\begin{vmatrix} p_k p_m^* & p_k V_{xm}^* & p_k V_{ym}^* & p_k V_{zm}^* \\ V_{xk} p_m^* & V_{xk} V_{xm}^* & V_{xk} V_{ym}^* & V_{xk} V_{zm}^* \\ V_{yk} p_m^* & V_{yk} V_{xm}^* & V_{yk} V_{ym}^* & V_{yk} V_{zm}^* \\ V_{zk} p_m^* & V_{zk} V_{xm}^* & V_{zk} V_{ym}^* & V_{zk} V_{zm}^* \end{vmatrix}, \quad k,m = 1,\ldots,M . \tag{7}$$

Here p_k and $V_{r,m}$ ($k,m = 1,...,M$, r = x, y, z) are the sound pressure and projections of the vibrational velocity on *x*-, *y*-, and *z*-direction, which are produced by the sound sources at the *k*-th and *m*-th receiving modules.

Up to date, information on the vector field of the interfering noise is insufficient to exactly represent the members of the interference covariance matrix in a general form. This insufficiency is caused by both multi-component character of the interfering noise and their significant variability depending on the sea state, current velocity, and intensity of the ship's traffic in the region. Specific methods of arranging the vector receivers (bottom-mooring or suspending them within the water layer, decoupling the modules from the whole construction) are to be accounted for as well. The used interference model and actual frequency dependence also influence the cross-correlation coefficients for the signals received by the pressure sensor and by the sensor of horizontal and vertical components of the vibrational velocity, even if all signal parameters are measured at the same spatial point. For instance, high-frequency cross-correlation between p and V_z predominates at high sea stares. At low frequencies, if an intense far ship's traffic or storm take place, cross-correlation between p and V_x or between p and V_y is sometimes strong. In addition, the

correlation depends on the sea depth and on the bottom parameters, particularly on stratification of the sediments. To this end, prior to proceeding with the measurements, one should study the interference field in the specific region where the receiving modules are to be mounted, the environmental conditions being also investigated. To be specific without loss of generality, we assume that the interfering noise is spatially incoherent, that is, independent at outputs of adjacent receiving modules (if they are significantly separated in space). With such noise model, the covariance matrix is also block-structured one, 4·4 in dimensionality, each block, both diagonal and side one, being a diagonal matrix:

$$\begin{vmatrix} Q(p) & Q(p,x) & Q(p,y) & Q(p,z) \\ Q(p,x) & Q(x) & Q(x,y) & Q(x,z) \\ Q(p,y) & Q(x,y) & Q(y) & Q(y,z) \\ Q(p,z) & Q(x,z) & Q(y,z) & Q(z) \end{vmatrix} \qquad (8)$$

Here $Q(*)$ are diagonal matrices whose members are $Q_{km}(*) = \sigma^2(*)\delta_{km}$, $(k,m = 1,\ldots,M)$, where $\sigma^2(*)$ is a variance of the noise in a single measuring channel of either pressure or vibrational velocity component, $\delta_{km} = 1$ at $k = m$ and $\delta_{km} = 0$ at $k \neq m$. Quantities $Q(*,*)$ are also diagonal matrices that characterize the noise cross-correlation in the pressure and velocity channels or in channels of different components of the vibrational velocity. All models for the interfering noise imply that the relation

$$\sigma^2(p) = (\rho c)^2 \{\sigma^2(x) + \sigma^2(y) + \sigma^2(z)\} \qquad (9)$$

is valid.

The mentioned assumptions allow one to simplify modeling significantly. In practice, one should obtain the matrix from measurements and use it to estimate parameters of the signal model.

3. Methods of matched space-time processing and efficiency criteria

Consider the maximum likelihood method, the high-resolution method for signals of the form (3), and the sub-optimal algorithm that is based on measuring the covariance matrix for the received signals.

Maximum likelihood method for estimating the parameters

A general problem statement is as follows: the vector of unknown parameters θ is to be estimated from measured values of U. It is supposed that U is a complex vector quantity (of dimensionality μ) which is Gaussian-distributed with a zero mean value, $\langle U \rangle = 0,$, its covariance matrix K having members $K_{ij} = \langle U_i U_j^* \rangle$. The optimal estimates of θ are known to be yielded by roots of the system of equations

$$\beta_i = \frac{\partial}{\partial \theta_i} \ln\{f(U/\theta\} \quad = 0, \qquad i = 1,...,\Theta, \tag{10}$$

where $f(U/\theta)$ is the probability density of the measured vector U, Θ is the dimensionality of vector θ, this dimensionality being equal to the number of unknown parameters. For Gaussian signals, in view of the covariance matrix $K = \langle U \cdot U^* \rangle$, equation (10) may be reduced [5] to

$$\beta_i = U^* K \frac{\partial K}{\partial \theta_i} K^{-1} U - Tr\left(K^{-1} \frac{\partial K}{\partial \theta_i} \right) = 0, \qquad i = 1,...,\Theta, \tag{11}$$

where Tr is the matrix spoor. If the process is stationary and if the measured values may be estimated for several realizations,

$$\beta_i = \frac{1}{T} \sum_{\tau=1}^{T} \beta_i(\tau),$$

the latter relation may be represented

$$\beta_i = Tr\left\{ K^{-1}\frac{\partial K}{\partial \theta_i}\left(K^{-1}\hat{K} - E \right) \right\} = 0, \qquad i = 1,\ldots,\Theta. \quad (12)$$

Here E is the unity matrix, $\hat{K}$ is the estimate of the covariance matrix for the received signal, the members of this matrix being of the form

$$\hat{K}_{lm} = \frac{1}{t}\sum_{t} U_l U_m^{*}, \qquad l,m = 1,\ldots,\mu \quad (13)$$

and K denoting its theoretical value. It can be shown that the requirements for vector U are met for all versions (2) - (4) of the vector-forming procedure. For random acoustic fields that are Gaussin-distributed, relations (11) and (12) are valid, these relations determining the rule for maximum likelihood estimating. If systems of different (vector or vector-scalar) types are used, the method is to be modified by computing matrices K and $\hat{K}$ in view of the established rules (3) - (4) for forming vector U of the measured data.

Estimating algorithm based on measuring covariance matrix

In nearly all problems of underwater acoustics, computing the maximum likelihood estimate is rather intricate procedure. In practice, sub-optimal data processing is often used that relates the measured quantities (or functions of those) to the theoretical models. One of such sub-optimal processing algorithms is a direct consequence of expression (12). By equaling the round-bracketed expression to zero in (12), we obtain:

$$\hat{K} = K \text{ or } \hat{K}_{lm} = K_{l,m}, \qquad l,m = 1,\ldots,\mu. \quad (14)$$

This estimating algorithm may be treated as a specific case of the maximum likelihood method. The algorithm is based on measuring the covariance matrix of the received signals and valid for all types of receiving arrays - scalar, vector, and vector-scalar ones. Expression (14) is a consequence of the fact that the covariance matrix provides a full description for Gaussian signals with a zero mean value. Algorithm (14) is known as the direct-resolution method. It has been studied by Alekseev et al. [4] and Gitel'son et al. [6] as

applied to estimating parameters of both correlating and uncorrelating signals. If arrays of equidistant elements are used and the received signals are produced by uncorrelating sources, the Prony algorithm [7] is well-known to solve the system (14). Gitel'son et al. [8] has modified this method to estimate parameters of correlating signals that propagate from the source to receiver in a waveguide and may be presented as a superposition of rays or normal waves. Here, we propose to use the Prony algorithm for the vector-scalar arrays as well.

The members of matrices $\hat{K}$ and K are complex values except for the diagonal members that are real. Because of symmetry of matrix K ($K_{lm} = K^*_{ml}$), system (14) may be reduced to μ^2 real equations that, in general, may yield μ^2 unknown parameters.

Consider the system of equations as applied to measuring parameters of the signal sources that compose a multi-component noise-generating object (see Figs. 1 and 2). A full description of the sound field may be obtained with the use of the velocity potential for a signal source of unity power:

$$\Phi(t,r_m,r_n) = \Phi(r_m,r_n)\cdot \exp(-j2\pi ft + \gamma_n). \qquad (15)$$

Here r_m and r_n determine the receiver and source positions respectively, γ_n is a random initial phase. For the m-th receiving module, the sound pressure and vibrational velocity projections which are produced by a group of point sources of different powers may be specified in the form

$$p_m(t) = -j2\pi f\rho\sum_{n=1}^{N} a_n\Phi(t,r_m r_n), \qquad m = 1,\ldots,M,$$

$$V_{m,r}(t) = -\sum_{n=1}^{N} a_n \frac{\partial\Phi(t,r_m r_n)}{\partial r}, \qquad r = x,y,z, \qquad (16)$$

where a_n is the random amplitude corresponding to the n-th source, the variance being equal to the source power. Members of the signal matrix may be obtained by Fourier-transforming the correlation matrix of the received signals (if there is no noise) to yield:

$$S_{lm} = \langle U_l U^*_m \rangle = \sum_{n,q=1}^{N} A_{nq}\varphi_{ln}\varphi_{mq}, \qquad l,m = 1,\ldots,\mu, \qquad (17)$$

where, to reduce the notation, we denote:

$$\varphi_{mn} = \begin{cases} -j2\pi f\rho\Phi(r_m r_n) & \text{at } 1 \le m \le M,\ n = 1,\ldots,N \\ \dfrac{\partial\Phi(r_m r_n)}{\partial r}, & r = x \text{ at } M+1 \le m \le 2M \\ & r = y \text{ at } 2M+1 \le m \le 3M \\ & \text{and } r = z \text{ at } 3M+1 \le m \le 4M \end{cases} \tag{18}$$

Here $A_{nq} = \langle a_n . a_q \rangle$ is the complex covariance of the n-th and q-th signal sources at some spatial point, at the coordinate origin, for instance:

$$A_{nq} = a_{nq} \exp(-j\beta_{nq}, \qquad n,q = 1,\ldots,N, \tag{19}$$

where a_{nq} is the mutual power of the sources, β_{nq} is the phase delay for the n-th source relative to the q-th one at frequency ω.

Finally, system (14) takes the form

$$\hat{K}_{lm} = \sum_{n,q}^{N} A_{nq}\varphi_{ln}\varphi_{mq} + Q_{lm}, \qquad l,m = 1,\ldots,\mu, \tag{20}$$

where Q is a matrix that determines space-time characteristics of the noise, particularly, matrix Q has the form (8) for spatially uncorrelating noise.

If there is no correlation between different signal sources, the number of unknown parameters is equal to $4N$. If the correlation exists, the number of unknown (real) parameters is equal to $3 \cdot N + (N^2 + 3N)/2 - 1$ and involves the following terms:

N signal powers a_{nq}, n=q;

$N - 1$ phase delays of the signals relative to a single one which is treated as a reference signal, that is, $\beta_{nq} = \beta_n - \beta_q$, and $\beta_1 = 0$ for the reference one;

$(N^2 - N)/2$ mutual powers a_{nq}, n≠q;

$3N$ spatial coordinates of the sources.

In the aforementioned list, three initial terms characterize cross-correlation relations between the sources if they are specified as $A_{nq}=a_{nq}\exp(-j\beta_{nq})$ (the corresponding number of unknown quantities is $(N^2+3N)/2-1$), the system of equations being nonlinear with respect to a_{nq} and β_{nq}. Because well-developed methods for solving systems of linear equations are preferable, complex quantities A_{nq} are usually treated as unknown ones. As $A_{nq} = A^*_{qn}$ and A_{nn} is a real quantity, the number of unknown parameters that characterize the cross-correlation coupling is increased up to N^2.

Members of the interference matrix Q_{lm} in (20) are to be measured experimentally. On the other hand, if the spatial noise coherence is unknown, power levels of all the components (pressure and projections of the vibrational velocity), along with correlation coefficients between the components, should be also treated as unknown parameters.

High-resolution estimates of source location

With signals of the *pV*-receivers, so called goniometric version of the processing algorithm may be proposed that has asymptotically infinite resolution and is based on algebraic properties of the covariance matrix.

Usually, the problem statement may be formulated as follows: coordinates of *N* uncorrelating point sources are to be found by using an array of *M* perfect pressure receivers. Outputs of the *M* sensors are represented by stationary random processes with zero mean values and the covariance matrix *K*, the latter being obtained by Fourier-transforming the correlation matrix of the received signals. It is supposed that the sources are fully coherent over the array aperture and cross-correlation matrix of the *i*-th source may be specified as a matrix of unity rank:

$$S_i = a_i \varphi_i \varphi_i^* . \qquad (21)$$

Here a_i is a power of the *i*-th source, φ_i is the direction vector that determines a profile of the wave front, components of this vector depending on coordinates of the source and receiving sensors; vector φ_i may be called

«propagation model». It is also supposed that the noise does not correlate with the sources and me be described with matrix $Q = \sigma J$ where J is the spatial coherence matrix, and σ is the noise power. Hence, the cross-correlation matrix of the received signals may be represented as

$$K = \sum_{i=1}^{N} a_i \varphi_i \varphi_i^* + \sigma J. \qquad (22)$$

Thus, the problem is reduced to finding N direction vectors φ_i and the corresponding source coordinates from the measured matrix K. This method known as the goniometer is based on the «classic» relation [9]:

$$KerS = \left|\varphi_i\right|_{i=1,N}^{\perp},$$

where Ker is a kernel of the signal matrix $S = \sum S_i$, and $\left|\varphi_i\right|_{i=1,N}^{\perp}$ is a set of vectors that are orthogonal to all direction vectors. If w is a vector which belongs to $KerS$, $S \cdot w = 0$ and hence

$$J^{-1} \cdot K \cdot w = \sigma \cdot w, \qquad (23)$$

that is, w is the eigenvector $J^{-1} \cdot K$ corresponding to the eigenvalue σ which is a minimum one because S is a positively defined matrix. If matrix J of spatial noise coherence is unknown in practice, the kernel of matrix K may be found instead of that of $J^{-1} \cdot K$ because two symmetric matrices may be diagonalized simultaneously [10]:

$$WJW^* = I \quad \text{and} \quad WKW^* = \Lambda,$$

where A and W are matrices of eigenvalues and eigenvectors of matrix $J^{-1} \cdot K$ respectively. In addition,

$$WJ^{-1}KW^* = \Lambda.$$

As a rule, the kernel cannot be reduced to a single vector corresponding to the minimum value of K because this vector is sensitive to inaccuracy of the measurements. The linear combination of junior eigenvectors for the cross-correlation matrix may serve as the kernel:

$$B = \sum_{i=M=M_0}^{M} \zeta_i \cdot w_i ,$$

where M_0 is a number of the junior eigenvectors that are attributed to the noise sub-space. Choosing the values M_0 and weighting factors ζ_i is governed by a compromise between the robustness and accuracy requirements: at small M_0, the kernel is sensitive to random inaccuracy of the measurements, this leading to poor resultant accuracy; at large M_0, some sources may be lost. Finding the matrix kernel is only the first stage in high-resolution estimating procedure for the source coordinates. Further, one should test orthogonality of the kernel and direction vectors that model the signal propagation:

$$P(x,y,z) = \left\{\varphi^*(x,y,z) \cdot B \cdot B^* \cdot \varphi(x,y,z)\right\}^{-1}. \qquad (24)$$

The above considerations are valid if the receiving array consists of pressure sensors and sensors of the vibratrional velocity components and the received signals are specified according to (3). Actually, for a point source, the rank of the signal matrix is equal to unity, and the noise does not correlate with individual sources. Hence, the cross-correlation matrix may be also represented in the form (22). In this case, the direction vectors φ_i are to be calculated according to (18) in view of the fields of pressure and vibrational velocity components. Further considerations are independent of a specific form of matrices K, S, and J and components of vectors φ that model the propagation channel. Therefore, the high-resolution coordinate-estimating method is applicable to processing signals of vector-scalar arrays and may be matched to signals that propagate in limited or stratified media.

Estimating accuracy of measurements

In inverse problems, a main task is to compensate for the estimate offsets. To this end, a global extremum must be found. Variances of the estimates

obtained with the developed models are also of interest. Because of quasi-deterministic or random character of the signals and interfering noise, along with a finite observation time, the parameter estimates involve errors that may be calculated as follows.

A potential accuracy, which may be attained in estimating θ at given conditions (that is, source and receiver positions, signal-to-noise ratio, and so on), is to be calculated by using the Fisher information matrix [5, 11]:

$$B_{ij} = Tr\left(K^{-1}\frac{\partial K}{\partial \theta_i}K^{-1}\frac{\partial K}{\partial \theta_j}\right), \quad i,j = 1,\ldots,\Theta. \qquad (25)$$

The lower bounds for the covariance of the estimated parameters θ_i and θ_j are known to be members of the matrix that is inverse to the Fisher information matrix. In particular, variances of the unknown parameters are diagonal members of the matrix

$$\sigma^2(\theta_i) = \left(B^{-1}\right)_{ii}. \qquad (26)$$

Now let us derive expressions for estimation accuracy of the parameters corresponding to the solution of system (14). Due to symmetry of the matrices involved into the system $\hat{K} = K$, the matrix members are determined by μ^2 complex values that are within the main diagonal and above it. Values K_{lm} determine both the matrix and vector

$$G = \left| K_{11}, K_{12}, \ldots, K_{1M}, K_{22}, K_{23}, \ldots, K_{MM} \right|, \qquad (27)$$

μ^2 in dimensionality. Components of the vector are members of the covariance matrix that are arranged in an ordered fashion within the rows, starting from the diagonal member in each row. In view of vector G and similar estimate of vector $\hat{G}$, system (14) may be expressed as $\hat{G} = G$. Supposing that this system of equations may be solved by the least-square method, in view of correlation between the measured components of vector $\hat{G}$, one can calculate variances of the parameter estimates as diagonal members of the matrix [12]:

$$C = \left(B^{*} F^{-1} B\right)^{-1}. \qquad (28)$$

Here B is a matrix with members $B_{ip} = \frac{\partial G_i}{\partial \theta_p}$, F is the covariance matrix for the measured values, whose members are $F_{lr} = \operatorname{cov}\left(\hat{G}_l \hat{G}_r\right)$. Matrix F can be found in a following way:

$$F_{lr} = \operatorname{cov}(\hat{G}_l\ \hat{G}_r) = \operatorname{cov}(\hat{K}_{ij} \cdot \hat{K}_{mn}) = \left\langle \hat{K}_{ij} \cdot \hat{K}_{mn} \right\rangle - K_{ij} \cdot K_{mn} = \left\langle U_i U_j U_m U_n \right\rangle - K_{ij} \cdot K_{mn}.$$

By expressing the 4-th order moments of the Gaussian signals in terms of the 2-nd order moments, we obtain

$$F_{lr} = \left\langle U_i U_j^{*} \right\rangle \left\langle U_m U_n \right\rangle + \left\langle U_i U_{jn}^{*} \right\rangle \left\langle U_j U_n \right\rangle - K_{ij} K_{mn} = K_{im} K_{nj},$$

that is, covariance of members of matrix $\hat{K}$ is determined by the expectation of matrix K itself. Then, by substituting the obtained expression into (28), one can express a member of the error covariance matrix as follows:

$$C_{pq} = \left(\sum_{ijmn} \frac{\partial K_{ij}^{*}}{\partial \theta_p} \left(K_{im} K_{nj}\right)^{-1} \frac{\partial K_{mn}}{\partial \theta_q} \right)^{-1} = \left(\sum_{ijmn} \left(K_{nj}\right)^{-1} \frac{\partial K_{ji}}{\partial \theta_p} \left(K_{im}\right)^{-1} \frac{\partial K_{mn}}{\partial \theta_q} \right).$$

In the matrix form, it is equivalent to

$$C_{pq} = \left(Tr\left(K^{-1} \frac{\partial K}{\partial \theta_p} K^{-1} \frac{\partial K}{\partial \theta_q} \right) \right)^{-1}$$

and is the same as the estimate variance in the maximum likelihood method.

Thus, applying the direct-resolution method to estimation of unknown parameters from the investigatig system is a possible way to implement the optimal method.

4. Results of simulation

Algorithms of estimating parameters of the signal sources were simulated as applied to specific problems of underwater acoustics. It is supposed that an array of M modules is bottom-moored and oriented along the x-axis within a waveguide, 100 m in depth, the array being symmetric with respect to the coordinate origin (see Fig. 3). The pass-band of a narrow-band filter and the observation time are specified in a fashion that $\Delta f \cdot T = 1$, with the central frequency $f_0 = 100$ Hz. The signal-to-noise ratio (for sound pressure) is equal to 1 at the reception point. If there are several signal sources, this signal-to-noise ratio correspond to the first source of mentioned ones. The interfering noise is supposed to be uncorrelating.

The signal that propagates from the source to receivers is represented as a sum of several coherent components. The signal was computed with Belov's computer code in an integral representation. The waveguide was specified as a planar stratified medium. The upper layer of the waveguide is water with the sound speed profile $c(z)$ and density $\rho(z) = const$. The water layer overlies a system of water-like layers, H_i in thickness, with densities ρ_i, damping decrements δ_i, and the sound speed that varies linearly in depth. In turn, this system of layers overlies a uniform elastic half-space with density ρ_0, damping decrement δ_0, and speeds c_{0l} and c_{0t} of longitudinal and transversal waves respectively

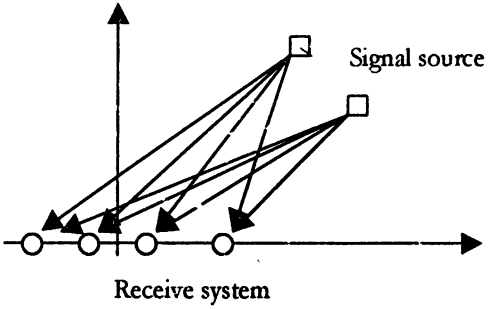

Fig. 3. Sketch of measuring procedure.

Comparison of resolution for arrays of different types

Consider the computed potential accuracy of estimating the source parameters for different types of the used arrays, namely: scalar, vector, and vector-scalar ones. The following coordinates of the point signal source (relative to the receiving modules, see Figs. 1, 3) are specified: x = 100 m, y = 3000 m, z = 70 m.

If the receiving array consists of a single module (that is locats at the coordinate origin), the signal arrives as a single plane or spherical wave, the source coordinates may be found by using only the vector-scalar module. For such situation, Table 1 summarizes rms errors of estimating the source parameter $\sigma(\theta\ )$, $\theta = S, x, y, z$, where S is the source power, x, y, z are the source coordinates.

Table 1

Type receiving modules	$\sigma(s)$ /S	$\sigma(x)$, ì	$\sigma(y)$, ì	$\sigma(z)$, ì
$U(p,V)$	1.003	122.6	82.1	122.7

If the signal propagates as a single plane or spherical wave, unknown source parameters are determined by projection components of the vibrational velocity in a manner that

$$V_x \sim Sx, \quad V_y \sim Sy, \quad V_z \sim Sz. \tag{29}$$

Therefore, with such model of the propagating signal, it is impossible to estimate all the four unknown source parameters by measuring only the vibrational velocity components. Additional information on the sound pressure,

$$p \sim S, \tag{30}$$

allows one to obtain the source parameters, even if the simplest model for sound propagation (3) is used.

If the propagation conditions imply that the signal is a coherent sum of several components (rays or normal waves), expressions (25) that relate the vibrational velocity components fail, and single modules of both vector and

vector-scalar type may be used to detect the source parameters. Table 2 summarizes the estimation accuracies for such propagation model.

Table 2

Type of receiving modules	$\sigma(s)$ /S	$\sigma(x)$,ì	$\sigma(y)$,ì	$\sigma(z)$,ì
$U(V)$	12.1	326.5	9578.7	129.6
$U(p,V)$	1.1	68.3	35.6	34.2

An intricate structure of the wave front at multi-ray or multi-mode propagation is more informative than that of a single propagating wave, either plane or spherical one. That is the reason of higher accuracy in the vector-scalar coordinate estimating for the received signals that are sums of coherent components, in comparison with the aforementioned case (see Table 1).

Consider the computed accuracies of estimating the source parameters by using a receiving array that consists of four equidistant modules located in line. The computations were carried out for different values of module spacing.

Table 3

Type of receiving modules	Intermodule spacing, m	$\sigma(s)$ /S	$\sigma(x)$,ì	$\sigma(y)$,ì	$\sigma(z)$,ì
$U(p)$	20	2,41	71,1	2126,0	-
	25	1,72	45,5	1360,6	-
	50	1,06	11,6	346,7	-
$U(V)$	20	1,03	6,8	45,3	17,1
	25	1,03	5,0	34,8	17,1
	50	1,03	1,8	19,2	17,1
$U(p,V)$	20	1,03	3,64	17,58	17,1
	25	1,03	3,0	17,3	17,1
	50	1,03	1,5	15,5	17,1

Analyzing the error correlation function shows that, with the use of the vector or vector-scalar modules, the estimated source powers nearly do not correlate with the measured x-, y-coordinates, the correlation coefficients being approximately equal to 0.2 - 0.3 in z-direction. This fact allows one to break up the algorithm of estimating the unknown parameters into two independent

procedures (power estimation and coordinate estimation), thereby significantly simplifying the processing software and making the computations faster.

The computations show that the advantage of the vector-scalar receiving modules (in comparison with the scalar ones) is especially high if the aperture is of the same order of magnitude as the distance, or if low-frequency broad-band signals are processed.

Goniometer simulation

To analyze detecting the source coordinates with pV-receivers, we simulated the aforementioned high-resolution method (see section III). In theory, even if the only pV-receiver is used, locations of at least three individual sources can be determined. Therefore, the following situation was simulated. The source coordinates were specified to be (0, 0, 100). Three individual source of equal powers were placed ar the same depths, their coordinates being $r_1 = (100,1200,60)$, $r_2 = (200,1000,60)$ and $r_3 = (300,1100,60)$. The scanning weights were matched to the structure of the propagating signal. Figure 4 shows the output response of a single pV-receiver that scan the x, y-plane, the focal point coinciding with the actual source position in z-direction. Similar output responce is presented in Fig. 5 for a receiving system consisting of two pV-receivers which are 10 m apart from each other on the x-axis. Figure 6 also shows the output response of the two-module receiving system (of two pV-modules) for a situation when there are five individual equal-power sources at points $r_1 = (100,1200,60)$, $r_2 = (200,1000,60)$, $r_3 = (300,1100,60)$, $r_4 = (400,1100,60)$ and $r_5 = (500,1150,60)$. A receiving system that consists of scalar sensors can resolve three individual sources if there are at least four pressure receivers in the array. Figure 7 presents the output response of the 4-element equidistant scalar array located at a depth of 100 m, the interelement spacing being equal to 10 m in x-direction. With the high-resolution signal processing and matching the algorithm to the propagation channel, this system rather well determines the source locations though its near-field radius is only $\cong$120 m. Of course, the pV-array is much more effective because, first, there no false peaks and the number of detected sources corresponds to the true one, and, second, a high resolution of closely located sources is attained, even with a single pV-module rather than with finite-aperture array.

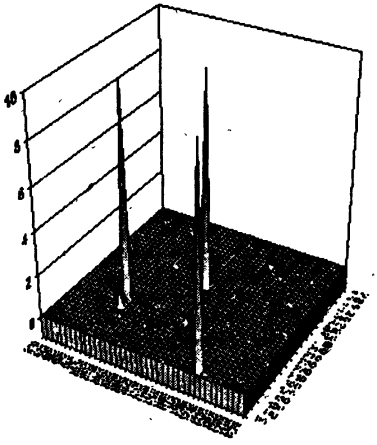

Fig. 4. Output response of single pV-module (3 sources).

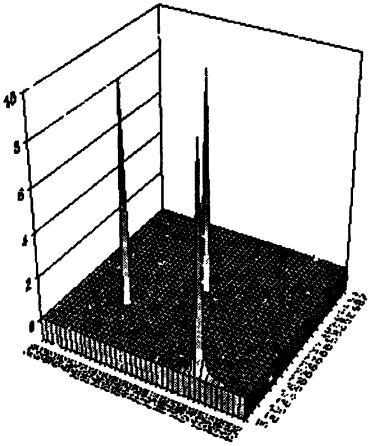

Fig. 5. Output response of receiving array consisting of two pV-modules (3 sources).

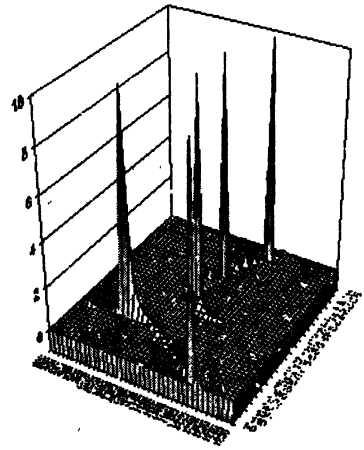

Fig. 6. Output response of receiving array consisting of two pV-modules (5 sources).

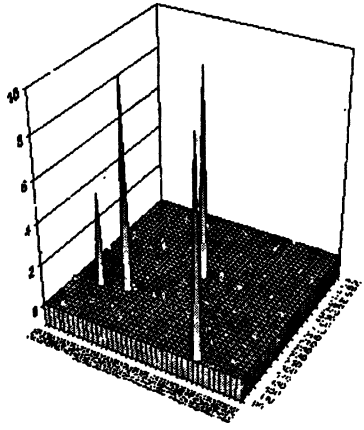

Fig. 7. Output response of receiving array consisting of four pV-modules (3 sources).

According to the computations, when the array aperture increases, the signal-to-noise ratio rapidly decreases for the receivers that are far from the array center. As a consequence, these receivers do not significantly contribute to the source resolution. Thus, the signal processing for detection of the noise source parameters shows that an optimal aperture exists for both scalar and vector-scalar receivers, this aperture yielding the maximum resolution. For the same channel

number of either scalar or vector-scalar array, the latter one exhibits higher resolution and accuracy, especially if low-frequency broad-band signals (broader than a half-octave) are processed.

The output responses shown in Fig. 8 illustrate the effect of changing frequency on the resolution of a single vector-scalar receiver and that of a scalar array consisting of four sensors that are equidistantly spaced by 10 m in line. Two individual sources of equal powers are located at points $r_1 = (100, 1000, 60)$ and $r_2 = (200, 1000, 60)$.

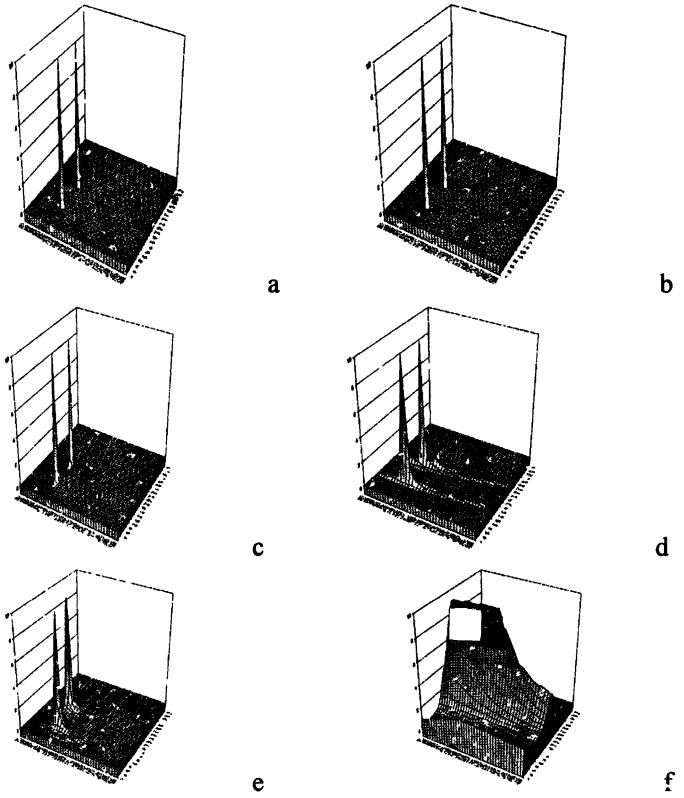

Fig. 8. The goniometer output response (two sources): a) vector-scalar module, f = 100 Hz; b) scalar array, f = 100 Hz; c) vector-scalar module, f = 30 Hz; d) scalar array, f = 30 Hz; e) vector-scalar module, f = 10 Hz; f) scalar array, f = 10 Hz.

Estimating directivity of sound source

If a directivity pattern of the source is to be estimated, a source model is usually specified that is represented by a point multi-component unit consisting of several elementary monopoles, dipoles, quadrupoles, and so on. The directivity pattern depends both on relative power levels of the elementary sources or their orientations in space and on the cross-correlation coefficients or phase shifts between them. If the cross-correlation relations are to be accounted for, a number of unknown source parameters is significantly increased, and hence the problem becomes more intricate, especially at low signal-to-noise ratios. Attempts to suppress the measurement errors by increasing the data acquisition time may not lead to the desired result because of instationarity caused by variations of noise at the source, changes in the transfer functions, instability of relative source and receiver positions, and so on. If vector-scalar receivers are used, the source directivity can be estimated at short observation times because the measurements may be performed at a close vicinity of the receiving array. In this case, the source usually cannot be treated as a point one; it should be rather considered as a system of several individual sources separated in distance. Positions and types of the elementary sources are supposed to be known for physical reasons or from *a priori* data. Another opportunity consists in using the experimental reconstruction [13, 14], further algorithm serving as a starting point for this approach.

We has shown that the accuracy of parameter estimating from the system of equations (20), of the form $\hat{K} = K$, is the same as that potentially attained. In addition, analyzing the Fisher information matrix show that estimating the source coordinates and power may be broken up into two independent computing procedures, this break up having nearly no effect on the accuracy of parameter estimates. Therefore, to estimate the source directivity, we use the system of equations

$$\hat{K}_{lm} = \sum_{n,q}^{N} A_{nq} \varphi_{ln} \varphi_{mq}$$

as a basis. If the source coordinates are known, this system may be rewritten in more "traditional" form that corresponds to the system of linear equations:

$$G = B\theta . \qquad (31)$$

Here, vector column G is obtained from the measured sound field, B is a matrix of coefficients, $\mu^2 \cdot N^2$ in dimensionality, which relates the μ^2 measured data (members of the covariance matrix) to N^2 unknown source parameters. Matrix

B is to be calculated with the use of the waveguide transfer function that depends both on its parameters (including the sea-floor ones) and on geometrical characteristics of the system layout (coordinates of the sources and receiving modules).

With the least-square method used relative to the parameters to be found, solution of equation (31) may be obtained in the form

$$\hat{\theta} = (B^* B)^{-1} B^* \hat{G} \ , \qquad (32)$$

if $(B^* B)$ is a full rank matrix. This matrix may be singular in the only case when a redundant parameter is being estimated. For instance, if linear form $G(\theta) = f_0 + f_1\theta + f_2\theta$ is used instead of $G(\theta) = f_0 + f_1\theta$. In general, redundancy takes place if the columns of matrix B are linearly dependent. For the problem at hand, closely located signal sources may also result in a weakly detemined matrix $(B^* B)$, the solution being inaccurate in this case. To provide robustness of the solution, additional limitations should be imposed on values of the vector θ of unknown parameters. The solution is regularized by adding the equations

$$\varepsilon\theta_i = 0, \quad i = 1,...,N,$$

where N is the number of unknown parameters. Constant ε is called the regularization parameter, and solving relative to the desired parameters yields:

$$\hat{\theta} = \left(B^* B + \varepsilon^2 \mathrm{E}\right)^{-1} B^* \hat{G} \ . \qquad (33)$$

The regularization provides that no singular value of matrix B can be less than ε and hence the least-square solution exists always. A choose of the regularization parameter depends on the noise level. At low signal-to-noise ratios, the noise level increase at singular values. In practice, it is advantageous to specify ε to be equal to the maximum singular value which is supposed to be determined mainly by the noise in free-space far zone.

Figures 9 and 10 show the computed directivity patterns for the source whose model coresponds to three point monopoles arranged in line and separated by 5 m. The receiving array is supposed to consist of four equidistant *pV*-receivers, 50 m apart from each other. The center of a multi-component source lies at point $r = (0,100,60)$. Belov's integral-form computer code was used to

calculate the acoustic field that is produced by each source at the receivers. System (20) was used to find members of the covariance matrix for individual sources. The found members are nearly the same as the theoretical ones. Therefore, the directivity patterns, which were computed for the theoretical data and for those yielded by simulations of the measurements, nearly coincide (curves *1* and *2* nearly cannot be distinguished from each other in figures). To calculate the directivity pattern of the multi-component source for standard free-space conditions, the following formular was used:

$$L(\theta) = \sum \varphi_n^*(\theta) A_{nq} \varphi_q(\theta),$$

where $\varphi(\theta)$ is the transfer function for an infinite homogeneous medium. In addition to the estimated unknown parameters and computed directivity patterns, the accuracy was calculated for estimating the covariance matrix of the individual sources according to (25). In computing directivity patern $L(\theta)$ according to (28), the accuracy was also recalculated to estimate rms erors of the patterns. In Figs. 9 and 10, 66% confidence intervals are shown for values $L(\theta)$ (curves *3* and *4*). In both figures, a direction of 0^0 corresponds to the x-axis along which the sources are located. The phase shifts between the sources were specified by using a generator of random numbers.

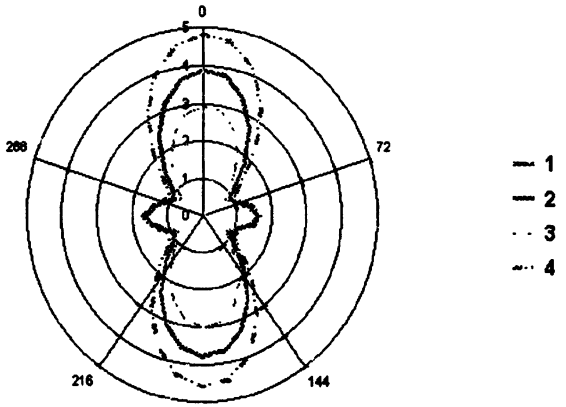

Fig. 9. Directivity pattern of 3-component sound source. It is obtained from measurements by normalizing to free space conditions. Waveguide depth is 100 m. Correlation coefficients between the sources are ρ = 0.7; phase shifts are $\beta_{12} = 180.7^0$, $\beta_{23} = 1{,}4^0$.

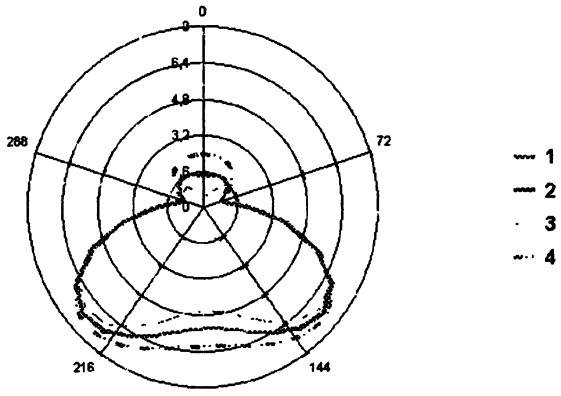

Fig. 10. Directivity pattern of 3-component sound source. It is obtained from measurements by normalizing to free space conditions. Waveguide depth is 100 m. Correlation coefficients between the sources are $\rho = 0.7$; phase shifts are $\beta_{12} = 80.7^0$, $\beta_{13} = -18.6^0$.

Conclusion

The proposed method of forming the vector of measured quatities allows one to apply the well-developed efficient algorithms to processing and analyzing the data when vector-scalar receiving arrays are used. It is shown that the system of equations $\hat{K} = K$ may serve to implement the optimal processing method and may be treated as a basis for solving a number of practical-purpose problems. The presented calculations illustrate a high resolution of the vector-scalar receivers, especially if finite-aperture arrays are used. The advantage of the vector-scalar receivers is most pronounced when broad-band signals are received within the near zone. It is shown that a group of vector-scalar receivers spatially resolves components of a complex source and yields the correlation coeficients and phase shifts between the individual sources, this serving as a basis for prognosticating directivity patterns of the complex sources in free space. The developed technique and computer software allows one to solve a number of applied problems in underwater acoustics and hydrophysics.

References

1. *Novikov A. K.* Correlation Measurements in Acoustics of Ships. Leningrad, Sudostroenie, 1971.
2. *Bobber R. J.* Underwater Electroacoustic Measurements. Naval Research Laboratory. Orlando, Florida, Washington D. C., 1970.
3. *Urick R. J.* Principles of Underwater Sound. 3rd ed. McGraw-Hill, New York, 1983.
4. *Alekseev V. I.* et al. Parameter Estimation Accuracy for Sources of Random Sound Signals by Using the Direct Resolution Method // Akust. Zhurn. 1981. V. 27. № 1. P. 30–35.
5. *Bangs W. J., Shultheiss P. M.* Space-Time Processing for Optimal Parameter Estimation // Signal Processing. London, 1973.
6. *Gitel'son V. S., Glebova G. M., Tikhonravov B. N.* Potential Accuracy in Parameter Determination for Correlating Signals // Vychislitel'nye sistemy i algoritmy. Rostov-na-Donu, 1989. P. 116–123.
7. *Bucker H. P.* Comparison of FFT and Prony Algorithm for Bearing Estimation of Narrow-Band Signals in a Realistic Ocean Environment // J. Acoust. Soc. Am. 1977. V. 61, № 3. P. 756–762.
8. *Gitel'son V. S., Glebova G. M., Kuznetsov G. N.* Parameter Determination for Correlating Signals by the Use of Prony Method // Akust. Zhurn. 1988. V. 34. P. 170–172.
9. *Reddy S. S.* // IEEE Trans., 1979. V. AES-15, № 1. P. 95.
10. *Fukunaga Keinosuke.* Introduction to Statistic Pattern Recognition // School of electrical engineering Purdue University< Indiana. Academic Press, New York and London, 1972.
11. *Van Trees H. L.* Detection, Estimation, and Modulation Theory. In 3 vols. John Wiley and Sons, Inc., New York - London - Sydney - Toronto, 1971.
12. *Hudson D. J.* Lectures on Elementary Statistics and Probability // Statistics. Geneva, 1964.
13. *Kendall M. G., Stuart.* Multi-Dimensional Statistic Analysis and Time Sequences // Moscow: Nauka, 1976.
14. *Fedorov V. V.* The Theory of Statistical Interference. Wiley, New York, 1971.

EMISSION TOMOGRAPHY RECONSTRUCTION OF BUBBLE PLUMES ENTRAINED BY BREAKING WIND WAVES

I.P. Smirnov, J.W. Caruthers, A.I. Khil'ko, and P.A. Elmore

INTRODUCTION

The goal of this article is to offer some ideas and schemes for estimating parameters related to localized distributions of point noise sources. The example system of noise sources envisioned in this work is a collection of individually oscillating bubbles which were produced at the sea surface by breaking waves and entrained to some distance below the surface. This collection having thereby formed a cloud of tiny sound sources whose characteristics we wish to determine. The method developed here for accomplishing this we will call *emission tomography*. Emission tomography involves the passive observation of a localized collection of sound sources using a complex system of linear antennae. The system provides a series of two-dimensional projections of the noise distribution.

From a physical point of view, the indicated process is reduced to a solution of an inverse problem consisting of the reconstruction of an extended inhomogeneous, non-stationary noise acoustical source in a randomly inhomogeneous refractive oceanic waveguide. This problem is closely associated with observations of broadband acoustical noise point sources. However, such problems are usually formulated for moving low-frequency point sources, so that a central use of this problem consists of separation of distortions, which are introduced by oceanic multi-wave oceanic environment.

We shall begin with a discussion of the current understanding the characteristics of bubble plumes entrained by breaking wind waves, and their numerical simulations appropriate for our application will be presented. This will be followed by the development of the principles of emission tomography in a form applicable to reconstruction of some of the characteristics of the plumes. Finally, their tomographic reconstruction is

1. BUBBLE PLUMES IN THE OCEAN

A large portion of intensively fluctuating and oscillating bubbles are just under a breaking wave on the surface of ocean. Some fluctuating bubbles rise to the surface [1,2]. This process produces broadband acoustic noise in the ocean. On the one hand, such noise can mask desired signals for passive and active acoustical image systems. On the other hand, such noise can be the signal of interest. It may be necessary, for example, to estimate parameters of a cloud of bubbles arising due to engineering activities or hydrophysical processes on the ocean surface. In such cases there is the problem of remote diagnostics of noise sources associated with clouds of bubbles, in particular, those arising from the breaking surface wind waves.

Two factors compound the problem of tomographical reconstruction of noise-source parameters associated with cloud of bubbles produced by breaking wind waves: multi-channel propagation caused by the influence of the refractive nature of the inhomogeneous oceanic environment and non-stationarities of noise acoustical sources which limit the time available for averaging. The existence of inhomogeneities results in additional decreasing of the coherence of radiated noise that limits the effectiveness of reconstruction of the noise-source characteristics [3]. In addition to volume random inhomogeneities, the rough surface plays a role; however, we shall not consider surface-wave effects.

The inversion of received noise-source signals has been investigated in terms of reconstruction of their location and signal characteristics in a homogeneous waveguide [4]. Other aspects of the formulated problem have also been investigated [5-11]. In particular, some were: (a) Coherence of bubble-plume noise were investigated experimentally [5], (b) Phenomena associated with the low-frequency bubble-plume oscillation as the collective oscillation [8], (c) Analysis of various aspects of underwater sound generation by breaking wind waves [9], and (d) development of physical models to describe the bubble-plume noise generation by different types of breaking wind waves [10,11].

Our present effort will attempt to reconstruct the noise-source location, size, and evolution in an inhomogeneous refractive oceanic waveguide with additive noise. We shall also investigate the influence of randomly distributed oceanic inhomogeneities on the reconstruction efficiency of the bubble-plume parameters.

1.1. Characteristics of bubble plumes

As follows from both theoretical considerations and experimental measurements, weak and moderate spilling as well as plunging breaking wind waves can exist. Noise generation is a complex phenomenon which is developed in space and time domains. Acoustical sources associated with noise radiating of by bubble plumes are localized in regions limited by depth and width in the order 1.5 - 2 *m* [12,13]. The length of a noise source is close to the breaking area of the wind wave, that is approximately 4 - 6 *m*. The density of bubbles are distributed nonuniform within this regions: the major part of bubbles are situated near the surface of the ocean. Thus, the high density region of bubbles in a plume can be in a layer with a depth about 20 - 40 *cm*. The void fraction in this region can be more than 15 - 20% in the bubble plumes. The average sizes of bubbles is about 0.2 - 0.4 *mm*; while the range of sizes is from 0.05 - 2 *mm*. The duration of the noise radiation is of the order of 1 - 5 *s* [12,13] and is broadband (10^1 - 10^5 *Hz*) [1,8,14,15] and partially coherent [21].

A dominant source of the noise is now understood to be bubble related. Individual damped bubble oscillations create higher frequency noise (above 500 *Hz*) at sound pressure levels of 75 - 80 *dB* relatively 1 μPa at one meter. The acoustic frequency that each bubble produces is inversely proportional to its radius [18]. Since a range of frequencies radiates from the cloud, a distribution of bubble sizes populates the cloud (for a review of bubble distribution measurements in bubble plumes, see [19]). In addition to individual bubble oscillations, the bubble cloud often undergoes a collective oscillation [1,8,17]. This mode of oscillation radiates low-frequency (tens of *Hz*) acoustical noise at sound pressure levels of 100 - 110 *dB* (collective oscillations seem to occur only with plunging breakers [1]). Higher frequency noise is observed to be continuous throughout the air entrainment process. Low-frequency noise, however, is observed to occur only during the middle of the entrainment process [8]. Laboratory experiments [10, 20] seem to indicate that many of the detectable individual bubble and collective oscillations probably are close to the surface.

1.2. Modeling bubble-plume acoustics

We may consider the characteristics of a bubble plume to be the set $\chi=\{\bar{r}, f(r), N, \Psi(\tau,r)\}$, where $\bar{r}$ is the plume's central position, $f(r)$ is a

function describing the geometric form of the plume in a fixed coordinate system with origin at r , N is the number of actively oscillating bubbles in the plume, and $\Psi(\tau,r)$ is the autocorrelation function of a pulse radiated by a bubble at the point r .

Consider a system of $N \gg 1$ bubbles in the region Ω forming the plume. Let the bubbles have random positions, r_i, $i=1,N$, within the region, so that the plume's form is specified as a statistical variable with $f(r)$ the probability density function of the bubbles within Ω . The mean number of bubbles, n, in any subregion, Ω', can be found by integration of this function over the subregion:

$$n = N \iiint_{\Omega'} f(r)\,dr \ .$$

We develop the form of the plume as both a Gaussian and a non-Gaussian model. However, only the Gaussian form will be carried forward in subsequent development. An ellipsoidal geometric shape for the plume is considered.

We assume that each bubble, once excited, will produce a damped oscillatory impulse specified by $\xi(t,r_i)=\xi_i(t)$. Let $\Psi(\tau,r_i)=\Psi_i(\tau)$ be the temporal autocorrelation function for each impulse. Then,

$$\Psi_i(\tau) = \int_{-\infty}^{+\infty} \xi_i(t)\,\xi_i(t+\tau)\,dt \approx \int_0^T \xi_i(t)\,\xi_i(t+\tau)\,dt \ ,$$

where T is the observation interval. The energy emitted by each impulse is $W_i=\Psi_i(0)$. For later reference, we note here that $\Psi_i(\tau)$ is a deterministic function for a given bubble, but that the bubble positions and initiation times are random. So that, the set $\{\Psi_i(\tau), i=1,N\}$ is a random function.

Initially, we follow a single-ray approach in which it is assumed that the impulse from any bubble arrives at an observation point, R , (assumed to be large compared to the dimensions of the plume) through only a single unique ray. We later generalize this to a multi-ray approach. The total signal, $\eta(t,R)$, received from the plume at the observation point and over the observation interval $[0,T]$ can be written in the form

$$\eta(t,R) = \sum_i A_i \xi_i(t-T_i)+n(t,R) \approx A\sum_i \xi_i(t-T_i)+n(t,R)\,, \qquad (1)$$

where $n(t,R)$ is the random stationary background noise field and A_i and T_i are the propagation amplitude and time, respectively, from the ith bubble to the receiver. Although the individual bubble pulses are damped oscillators, the received field, $\eta(t,R)$, is stationary on the observation interval. An exact expression for the impulse time delay has the form

$$T_i = \bar{T} + \frac{(r_i;\bar{e})}{\bar{c}} + \frac{(r_i;\bar{e}_\perp)}{2\bar{c}}\varphi_i + O(\varphi_i),$$

-where $\bar{T}$ is the time delay for the central point, $\bar{r}$, of the region Ω, $(\cdot;\cdot)$ is the scalar product of vectors, $\bar{e}$ and $\bar{c}$ are the direction of the ray and the sound speed at the central point, respectively, with $e_\perp$ defined by $(\bar{e};\bar{e}_\perp)=0$, φ_i is the angle between directions to central and ith points of the bubble plume, and $O(\varphi_i)$ represents higher order terms. Since we have assumed large propagation distances, the amplitude is approximately independent of the bubble position in the plume and its propagation time is approximated by

$$T_i \approx \bar{T} + \frac{(r_i - \bar{r};\bar{e})}{\bar{c}}.$$

Figure 1 shows these parameters graphically.

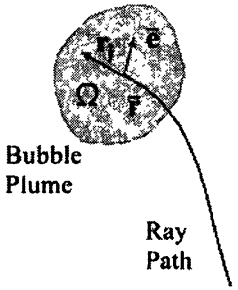

Figure 1. Sketch showing bubble plume spatial variables.

Writing signals in the form of (1), for two observation points, $R_p, p=1,2$, we have

$$\tilde{\eta}(t,R_p) = A_p \sum_i \tilde{\xi}_i\left(t - T_i^{(p)}\right) + \tilde{n}(t,R_p), \quad p=1,2.$$

For the above equation, we have also assumed the signals are linearly filtered as the first step in processing, and denoted them by $(\tilde{\cdot})$.

The cross-covariance function between the received, filtered, random signals (assumed to be stationary) at the two points is

$$
\begin{aligned}
k(\boldsymbol{R}_1,\boldsymbol{R}_2,\tau) &\equiv \left\langle \tilde{\eta}(t_1,\boldsymbol{R}_1)\tilde{\eta}(t_2,\boldsymbol{R}_2)\right\rangle = \int_0^T \tilde{\eta}_1(t)\tilde{\eta}_2(t+\tau)dt = \\
&= A_1A_2\sum_i\sum_{i'}\int_0^T \tilde{\xi}_i(t-T_i^{(1)})\tilde{\xi}_{i'}(t+\tau-T_{i'}^{(2)})\,dt + \left\langle \tilde{n}(t_1,\boldsymbol{R}_1)\tilde{n}(t_2,\boldsymbol{R}_2)\right\rangle = \\
&= A_1A_2\sum_i\int_0^T \tilde{\xi}_i(t-T_i^{(1)})\tilde{\xi}_i(t+\tau-T_i^{(2)})\,dt + \int_0^T \tilde{g}(\tau,|\boldsymbol{R}_1-\boldsymbol{R}_2|)\,dt = \\
&= A_1A_2\sum_i \tilde{\Psi}_i(\tau-T_i^{(12)}) + T\tilde{g}(|\boldsymbol{R}_1-\boldsymbol{R}_2|)\ ,
\end{aligned}
\tag{2}
$$

where T is the integration time of the filter, $\langle\cdot\rangle$ denotes statistical averaging, and the form of the filtered noise is prescribed by the equation. Finally, we write this as

$$
k(\boldsymbol{R}_1,\boldsymbol{R}_2,\tau) = k_{12}(\tau)+k_n(\tau)\ , \tag{3}
$$

where the definition of the two terms on the right is specified by inspection of (2).

In the above development the integration time, T, is presupposed to be sufficiently large in comparison with correlation time of the partial pulse[1], then

$$
T_i^{(12)} \equiv T_i^{(2)}-T_i^{(1)} \approx \bar{T}_2-\bar{T}_1+\frac{(\boldsymbol{r}_i-\boldsymbol{r};\bar{\boldsymbol{e}}_2-\bar{\boldsymbol{e}}_1)}{\bar{c}} \equiv \bar{T}_{12}+\frac{(\boldsymbol{r}_i-\boldsymbol{r};\bar{\boldsymbol{e}})}{\bar{c}}\ ,
$$

$\bar{T}_1$, $\bar{T}_2$, $\bar{\boldsymbol{e}}_1$, $\bar{\boldsymbol{e}}_2$ are the corresponding parameters for central point of region, $\bar{\boldsymbol{e}} = \bar{\boldsymbol{e}}_{12} \equiv \bar{\boldsymbol{e}}_2-\bar{\boldsymbol{e}}_1$, $\bar{T}_{12} \equiv \bar{T}_2-\bar{T}_1$.

As the number of bubbles becomes large (i.e., $N\to\infty$), then, according to Bernoulli's theorem, we can replace the sum of independent random variables in (2) by their mathematical expectation. We also re-insert the explicit dependence of $\tilde{\Psi}_i$ on $\boldsymbol{r}_i$ to get

---

[1] But less than the duration of the plume's existence and sufficiently small so that the second (noise) term in Eq. (2) remains less than the first (informative) term.

$$k_{12}(\tau)=A_1A_2\sum_i \tilde{\Psi}\left(\tau-T_i^{(12)},r_i\right) \approx A_1A_2N\iiint_\Omega\left\langle\tilde{\Psi}\left(\tau-\bar{T}_{12}-\frac{(r-\bar{r};e)}{\bar{c}},r\right)\right\rangle f(r)\,dr = \\ = A_1A_2N\iiint_\Omega\left\langle\tilde{\Psi}\left(\tau-\bar{T}_{12}-\frac{(r-\bar{r};\bar{e})}{\bar{c}},r\right)\right\rangle f(r)\;dr\;. \tag{4}$$

The above procedure, in effect, takes the discrete noise sources in the region Ω and smears them over the region into a continuum . We define the following quantity

$$K(\tau,r)\equiv A_1A_2N\left\langle\tilde{\Psi}\left(\tau-\bar{T}_{12}-\frac{(r-\bar{r};\bar{e})}{\bar{c}},r\right)\right\rangle \tag{5}$$

and substitute it into (3) to get

$$k_{12}(\tau)=\iiint_\Omega K(\tau,r)f(r)\,dr\;.$$

Substituting this into (3) we get

$$k(R_1,R_2,\tau) \approx \iiint_\Omega K(\tau,r)f(r)\;dr+k_n(\tau)\;, \tag{6}$$

which is a Fredholm integral equation of the first kind. Equation (6) will be the basis for the development of emission tomography as developed in the Section 2.

1.2.1. Gaussian temporal model for individual bubble statistics

Let us assume the following Gaussian model for the autocorrelation function of a single pulse, $\tilde{\xi}(t,r)$:

$$\left\langle\tilde{\Psi}(\tau,r)\right\rangle = \tilde{W}(r)\exp\left(-\frac{\tau^2}{\tau_\xi^2}\right)\cos\omega_0\tau\;, \tag{7}$$

where ω_0 is the central frequency, τ_ξ is the correlation time, $\tilde{W}(r)$ is the filtered energy of the impulse (corresponding to the previously defined discrete energy W_i). As follows from (7), the statistics of all bubbles pulses is assumed to be the same, except the full energy, that may depend of the bubble radiation point, r . If the passband of the filter is sufficiently small

in comparison with the original bubble-pulse bandwidth, then the form of (7) is really defined by the transition function of the linear filter, so it may be considered to be known, and its parameters, ω_0 and τ_ξ, can be changed by the observer.

1.2.2. Gaussian spatial model of a bubble plume

Let the probability density function, $f(\boldsymbol{r})$, of the source spatial distribution have the form

$$f(\boldsymbol{r}+\bar{\boldsymbol{r}}) = \frac{1}{\sqrt{(2\pi)^3 \det\Lambda}} \exp\left(-\frac{1}{2}(\boldsymbol{r};\Lambda^{-1}\boldsymbol{r}) \right) , \tag{8}$$

where the symmetrical, positive semi-definite matrix Λ describes the spatial form of the plume which we chose to be an arbitrarily oriented ellipsoid $(\boldsymbol{r};\Lambda^{-1}\boldsymbol{r}) \le 1$ with the center in the origin of the coordinate system

Suppose also, that full energy of pulse depends on the point of emission by analogous formula

$$W(\boldsymbol{r}+\bar{\boldsymbol{r}}) = W_0 \exp\left(-\frac{1}{2}(\boldsymbol{r};G\boldsymbol{r}) \right) , \tag{9}$$

where G is a positive semi-definite matrix. Matrices Λ and G may depend on the each other. For an example, the case of the similar matrix, $G = \lambda\Lambda^{-1}$ may be considered. When $\lambda=0$, the energies of all pulses are equal.

If the distributions, Eqs. (7,8,9), are substituted into (4), then the following expression for the correlation moment is obtained (see Appendix A):

$$k_{12} = k_{12}^{(0)} \sqrt{\beta\gamma} \exp\left(-\beta q^2 - (1-\beta)p^2\right) \cos 2\beta pq , \tag{10a}$$

where

$$k_{12}^{(0)} \equiv A_1 A_2 N W_0$$

$$\begin{aligned} p &\equiv \frac{\omega_0 \tau_\xi}{2}, \quad l_\xi \equiv \bar{c}\tau_\xi, \quad \nu \equiv L(\bar{e})/l_\xi, \\ q &\equiv \frac{\tau - \bar{T}_{12}}{\tau_\xi}, \quad \vartheta \equiv \|e\| \equiv \left| 2\sin\frac{\varphi}{2} \right|, \\ \gamma &\equiv \det(I+\Lambda^{-1}G), \quad \beta^{-1} \equiv 1+\nu^2\vartheta^2 \end{aligned} \tag{10b}$$

The above parameters have the following meanings: p is the *base of*

impulse; q is the *relative delay*, i.e., the difference between pulse travel times to the hydrophones from center of the plume in units of τ_ξ ; l_ξ is the *scale of coherence of pulse*; v is the *relative generalized size of the plume* in direction of vector e in units of l_ξ ; $\hat{v}$ is the *angular size of the antenna base* from center of the plume; and φ is the *angle between vectors* $\bar{e}_1$ and $\bar{e}_2$.

Graphs of $k_{12}/k_{12}^{(0)}\sqrt{\gamma}$ as functions of $v\hat{v}$ for given values p and q are represented in Fig. 2. For fixed values of the parameters p and β the mutual correlative moment, $k_{12}^{(0)}$, is maximal:

$$k_{12}^{\max} = k_{12}^{(0)}\sqrt{\frac{\gamma}{1+v^2\hat{v}^2}}\exp\left(-\frac{v^2\hat{v}^2p^2}{1+v^2\hat{v}^2}\right) = k_{12}^{(0)}\sqrt{\beta\gamma}\exp\left(-(1-\beta)p^2\right), \qquad (11)$$

when $q = 0$ (i.e., $\tau=\bar{T}_{12}$). For a fixed position of the antenna, we can change the relative delay, q, artificially in an electronic manner and get maximum value of the moment.

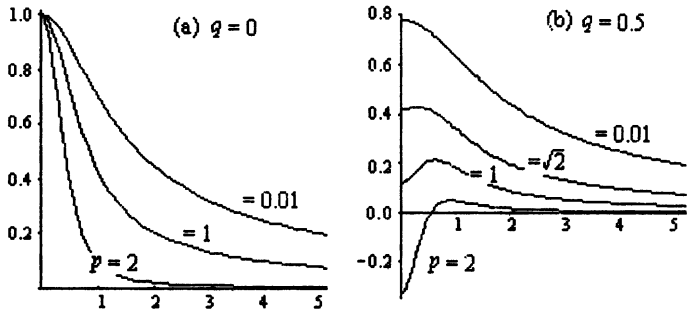

Figure 2. Plots of $k_{12}/k_{12}^{(0)}\sqrt{\gamma}$ of as a function of $(v\hat{v})$ for (a) q=0 and (b) q=0.5.

From the last remark the possibility of measurement of the parameter l_ξ follows. For this purpose we can measure the dependence of the electronic delay that maximize the moment on the angle α between the line of hydrophones and the direction to the plume. This dependence has the form $\Delta\tau=(2d/l_\xi)\cos\alpha$. Measuring this function, we can find the relative size, $\mu \equiv d/l_\xi$, and the direction angle to the plume. Also note, that for given

values of the base, p, and the relative delay, q, the maximal value of the correlative moment depends only on the product $v\vartheta$.

In limiting cases it is possible to derive from (10) an approximate formulas for the integral correlative moment:

if $v\vartheta \ll 1$, then $k_{12} = k_{12}^{(0)} \exp(-q^2 - v^2\vartheta^2 p^2)\cos 2pq$

if $v\vartheta \gg 1$, then $k_{12} = k_{12}^{(0)} \exp(-p^2)/v\vartheta$.

1.2.3. Non-Gaussian spatial model of a bubble plume

Let the plume's probability density function be

$$f(\boldsymbol{r}) = \tilde{C}(\boldsymbol{r};Q\boldsymbol{r}) \exp\left(-\frac{1}{2}(\boldsymbol{r};C^{-1}\boldsymbol{r}) \right) , \tag{12}$$

where $\tilde{C} = \left(\mathrm{Tr}CQ\sqrt{(2\pi)^3 \det C}\right)^{-1}$ is the normalizing constant[2], Tr(.)is the trace of the matrix (.).

In describing the plume form, matrices C, Q are assumed symmetrical, positive definite. In particular, for $Q=I$, $C^{-1} = 2r_0^{-2}I$ the plume of spherical-shell form can be obtained from (12). The equation for the correlation moment in this case is derived in Appendix B:

$$k_{12} = \frac{1}{3}k_{12}^{(0)}\sqrt{\beta}\exp(-\beta q^2 - (1-\beta)p^2) \times$$
$$\times \left((2+\beta+2(\beta-\beta^{-1})(p^2-q^2))\cos 2\beta pq - pq(\beta-\beta^{-1})\sin 2\beta pq\right) . \tag{13}$$

In the particular case when $q=0$, i.e. $\tau=\bar{T}_{12}$, the maximal value of the moment $k_{12}^{(0)}$ is

$$k_{12}^{\max} = \frac{1}{3}k_{12}^{(0)}\sqrt{\beta}\exp\left(-(1-\beta)p^2\right)\left(2+\beta+2(\beta-\beta^{-1})p^2\right) .$$

---

[2] The condition of normalization for the density function $f(\boldsymbol{r})$ is

$$\int_{R^3} f(\boldsymbol{r})\,d\boldsymbol{r} = \tilde{C}\int_{R^3}(\boldsymbol{r},Q\boldsymbol{r})\exp\left(-\frac{1}{2}(\boldsymbol{r},C^{-1}\boldsymbol{r}) \right) d\boldsymbol{r} = \tilde{C}\mathrm{Tr}Q^T C\sqrt{(2\pi)^3 \det C} = 1 .$$

The results of comparative calculations of the correlative moments (Eqs. (10) and (13)) as functions of ν and ϑ for given values of p and q are represented in Fig. 3.

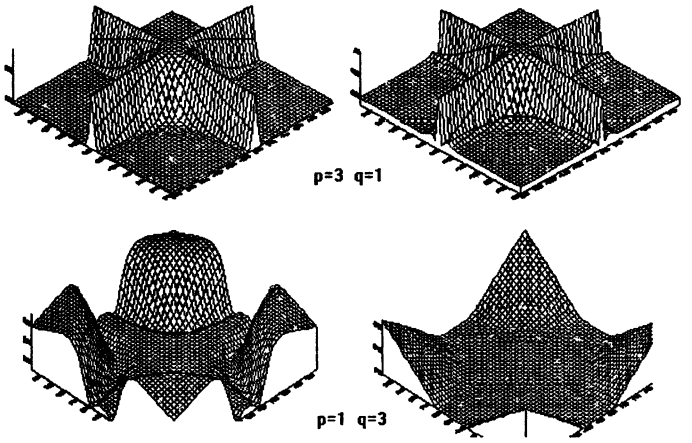

Figure 3. Correlation moments as function of ν and ϑ for an ellipsoid (left column) and for a spherical shell (right column).

Plots of the function $f(\beta,p) \equiv \sqrt{\beta}\,(2+\beta+2(\beta-1/\beta)p^2)\exp(-(1-\beta)p^2)$ for different values of the parameter p are represented in Fig. 4. Let us note in that figure that for any fixed $p>2$ the function $f(\beta,p)$ has the local minimum at some $\beta^* \in (0,1)$ which is the root of the cubic equation

$$2p^2(1+2p^2)\beta^3+(3+10p^2)\beta^2+2(1-2p^4)\beta+2p^2 = 0 .$$

For this root we can derive the asymptotic (for $p \gg 1$) expression

$$\beta_1 \simeq \frac{2p^4-1}{p^2(2p^2+1)} \simeq 1-\frac{1}{2p^2} .$$

This fact can be used for the experimental estimation of the plume size. While increasing the angle size of the base ϑ, the moment first decreases then begin to increases. The minimum point corresponds to

$$\nu\vartheta_{min} = \sqrt{\frac{1}{\beta_1^2} - 1} \approx \frac{\sqrt{2p^2+1}}{2p^2-1} .$$

So, if we know ϑ_{min} we can estimate the relative size of the plume ν.

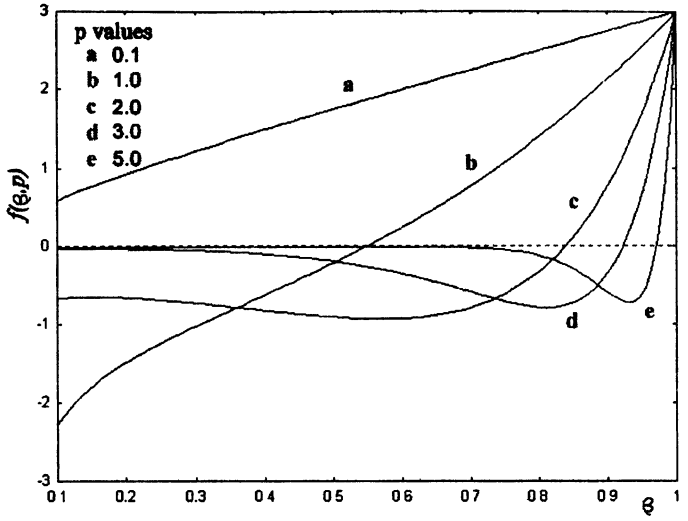

Figure 4. Plot of function f(β,*p*) for several values of *p*.

1.3. The case of small antenna size

For small sizes of the plume (in comparison with radii of curvature of the phase front) and the base, *d*, of the receiving system, taking into account the theorem of duality for the geometrical acoustics approach, we can write

$$d_{\perp} \approx R\sqrt{F}\varphi$$
$$L(\tilde{e}) \approx R\sqrt{F}\psi ,$$

where $d_{\perp}=d\sin\alpha$ is the cross size of the antenna, ψ is the angular size of the plume from the central point of the antenna, R is the distance to the plume, F is vertical focusing factor of horizontal-layered medium. So,

$$\nu\vartheta \equiv \frac{L(\tilde{e})}{l_\xi}\|e\| \approx \frac{L(\tilde{e})}{l_\xi}\varphi \approx \frac{d_{\perp}}{l_\xi}\psi \equiv \mu_{\perp}\psi ,$$

where $\mu_\perp \equiv d_\perp / l_\xi$ is the relative cross size of the antenna base.

Hence, for small plumes and receiving systems we can also use instead of (10) more simple and convenient formula

$$k_{12} = k_{12}^{(0)} \frac{1}{\sqrt{1+\mu_\perp^2\psi^2}} \exp\left(-\frac{q^2+p^2\mu_\perp^2\psi^2}{1+\mu_\perp^2\psi^2} \right) \cos\frac{2pq}{1+\mu_\perp^2\psi^2} . \qquad (14)$$

As function of the product $\mu_\perp\psi$

$$k_{12}(0) = k_{12}^{(0)} \frac{1}{\sqrt{1+(\mu_\perp\psi)^2}} \exp\left(-\frac{(\mu_\perp\psi)^2 p^2}{1+(\mu_\perp\psi)^2} \right) , \qquad (15)$$

is strictly monotonically decreasing, taking its maximal value for zero value of the argument. It decreases for three times when $\mu_\perp\psi \approx \exp(1-p^2)$. So, the condition of high correlation in two points can be written in the form

$$\mu_\perp\psi \le \exp(1-p^2) . \qquad (16)$$

From this, we see that correlation is large for a small angular size of a plume and small size of an antenna. When time of correlation, τ_ξ , increases, the base of impulse, p, increases also, and this can lead to a conclusion about decreasing correlation. This conclusion is wrong, however, because the condition (16) by itself is correct only for bounded values of p. Actually, the correlation (11) is small for small values of τ_ξ because, in this case, the base of the receiving system exceeds the spatial scale of the correlation of the impulse, and for large values of τ_ξ, the correlation becomes large, independent of this parameter.

1.4. The multi-ray approach

The results of the above sections can be simply generalized for the case of multi-ray type of pulse propagation. Let signals in two receivers be

$$\eta(t,\boldsymbol{R}_p) = \sum_j A_{pj} \sum_i \xi_i\left(t-T_{ij}^{(p)},\boldsymbol{r}_i\right)+n(t,\boldsymbol{R}_p) , \quad p=1,2 ,$$

where index j marks rays connecting the receiver with the plume. The mutual correlation moment of signals after linear filtering is

$$k(\boldsymbol{R}_1,\boldsymbol{R}_2) \equiv \int_0^T \tilde{\eta}_1(t)\,\tilde{\eta}_2(t+\tau)\,dt =$$

$$= \sum_j \sum_{j'} A_{1j}A_{2j'} \sum_i \sum_{i'} \int_0^T \tilde{\xi}\left(t-T_{ij}^{(1)},\boldsymbol{r}_i\right)\tilde{\xi}\left(t-T_{i'j'}^{(2)},\boldsymbol{r}_{i'}\right)dt =$$

$$= \sum_j \sum_{j'} A_{1j}A_{2j'} \sum_i \tilde{\Psi}\left(T_{ij'}^{(12)},\boldsymbol{r}_i\right) + T\tilde{g}\left(|\boldsymbol{R}_1-\boldsymbol{R}_2|\right),$$

where $T_{ij'}^{(12)} \equiv T_{ij}^{(2)} - T_{ij'}^{(1)} = \bar{T}_{12}^{(jj')} + (\boldsymbol{r}_i;\boldsymbol{e}_{jj'})/\bar{c}$, $\bar{T}_{12}^{(jj')} \equiv \bar{T}_2^{(j)} - \bar{T}_1^{(j')}$, $\boldsymbol{e}_{jj'} \equiv \bar{\boldsymbol{e}}_2^{(j)} - \bar{\boldsymbol{e}}_1^{(j')}$.

For pulses with correlation function (7), equal energies, W_0, and Gaussian form of the plume (8), we can derive (see Appendix C) the following formula for the moment:

$$k_{12} = NW_0 \sum_{jj'} A_{1j}A_{2j'} \frac{1}{\sqrt{1+\mathrm{v}_{jj'}^2\vartheta_{jj'}^2}} \exp\left(-\frac{q_{jj'}^2+p^2\mathrm{v}_{jj'}^2\vartheta_{jj'}^2}{1+\mathrm{v}_{jj'}^2\vartheta_{jj'}^2}\right) \cos\frac{2pq_{jj'}}{1+\mathrm{v}_{jj'}^2\vartheta_{jj'}^2},$$

where $\vartheta_{jj'} \equiv \|\boldsymbol{e}_{jj'}\|$, $q_{jj'} \equiv \bar{\tau}_{12}^{(jj')}/\tau_\xi$, $p \equiv \omega_0\tau_\xi/2$, $\mathrm{v}_{jj'} \equiv L(\bar{\boldsymbol{e}}_{jj'})/l_\xi$.

If the size of the antenna array is small in comparison with the scale of ray map, then sets of rays connecting the plume with different hydrophones can be considered as similar in the sense that, for any ray for the first receiver, there exists a close one for the second receiver. Neglecting correlation among pulses from different sets of rays[3] and differences in amplitudes of pulses in different receivers, we obtain the following simple representation for the mutual correlative moment:

$$k_{12}(\tau) = NW_0 \sum_j A_j^2 \frac{1}{\sqrt{1+\mathrm{v}_{jj}^2\vartheta_{jj}^2}} \exp\left(-\frac{q_{jj}^2+p^2\mathrm{v}_{jj}^2\vartheta_{jj}^2}{1+\mathrm{v}_{jj}^2\vartheta_{jj}^2}\right) \cos\frac{2pq_{jj}}{1+\mathrm{v}_{jj}^2\vartheta_{jj}^2}.$$

[3] Assume, for example, that the difference in impulse delays for different rays are much more τ_ξ.

2. THE APPROACH OF EMISSION TOMOGRAPHY

A set of unknown characteristics of a bubble plume, $\chi = \{\bar{r}, f(r), N, \Psi(\tau,r)\}$, was defined in Section 1.2. Let us assume that we have some indirect knowledge of χ based on a measured set of data, u, from which we seek to understand some of those characteristic. In general, the problem is stated in the form of an integral equation, i.e.,

$$u = A\chi , \tag{17}$$

where integral operator A describes the properties of the transmitting medium and the receiver system. Symbolically, the problem reduces to the solution, $\chi = A^{-1} u$. Practically, however, (17) is ill-posed, and, therefore, can be solved only with the use of additional information about the bubble plume. A means of solving such an inverse problem can be based on computerized tomography [22].

2.1. Multi-element array of receivers

In the capacity of the indirect available information, u, about bubble plume, we could use the matrix $k(\tau) = \{k_{ij}(\tau)\} = \{k(R_i, R_j, \tau)\}$ of the mutual correlation moments of signals received on pairs of hydrophones of an antenna system and passed through preliminary filters. We now have a matrix of Fredholm integral equations of the first kind representing all pairs corresponding to the single pair represented in (6):

$$k_n(\tau) + \iiint K(\tau,r) f(r)\, dr = k(\tau) . \tag{18}$$

The noise correlation is a matrix of values representing all the hydrophone pairs, i.e., $k_n(\tau) \equiv \{k_{n,ij}(\tau)\}$.

Other parameters in the equations of the previous section must be subscripted with ij as well. We repeat those here for completeness. The kernel (5) takes the form

$$K(\tau,r) = \{K_{ij}(\tau,r)\} = A_i A_j N \left\langle \tilde{\Psi}\left(\tau - \bar{T}_{ij} - (r - \bar{r}; \bar{e}_{ij}\bar{c}), r\right)\right\rangle =$$

$$= A_i A_j N \tilde{W}(r) \exp\left[-\left(\tau - \bar{T}_{ij} - (r - \bar{r}; \bar{e}_{ij}/\bar{c})\right)^2 / \tau_\xi^2\right] \cos\omega_0\left(\tau - \bar{T}_{ij} - (r - \bar{r}; \bar{e}_{ij}/\bar{c})\right) .$$

Since the parameters, $A_{i,j}$, $\bar{e}_{ij}$, $\bar{T}_{ij}$, N, $\tilde{W}(r)$, are not known *a priori*, we restrict the set of possible solutions of (18) to a set of Gaussian functions (8). We

also consider only the case of equal energy pulses, i.e., $\tilde{W}(r) = \tilde{W}_0$.

2.2. Plume parameter estimation

In this section, the possibilities of reconstructing the forms of bubble plumes are considered. A geometrical acoustics approach for describing sound propagation in a waveguide is used. A plume is presupposed to situate under the free surface in the search region Ω at the vertical distance H to the antenna system know *a priori* (see Fig. 5). The receiving antenna system is assumed to be a collection of linear hydrophones antennae situated on the bottom in a symmetrical form about their geometric center. For every pair of hydrophones, the mutual correlation moment of the received, prefiltered signals, $k_{ij}(\tau)$, are measured.

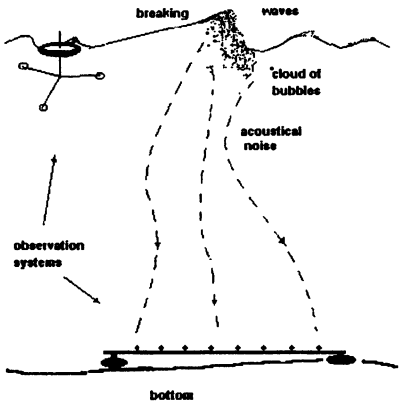

Figure 5. Scheme of the experimental system.

As a method of regularization, the reduction of (18) to nonlinear algebraic system is used. For this, we restrict the set of possible solutions of the integral equation to the parametric one, using appropriate information about plume's form (e.g., ellipsoidal as use here). Now one can converge (18) to the system of nonlinear algebraic equations

$$k_{n,ij}(\tau) + k_{ij}^{(0)} \sqrt{\beta_{ij}} \exp\left(-\beta_{ij} q_{ij}^2 - (1-\beta_{ij}) p^2\right) \cos 2\beta_{ij} p q_{ij} = k_{ij}(\tau) \qquad (19)$$

with respect to the unknown values $\bar{r}$ and Λ defining the position and form of the plume, respectively. Some of the quantities defined in (10b) must now be subscripted as follows:

$$\beta_{ij}^{-1} \equiv 1+\nu_{ij}^2\vartheta_{ij}^2 ,$$
$$\nu_{ij} \equiv L(\vec{e}_{ij})/l_\xi, \quad \vartheta_{ij} \equiv \|\boldsymbol{e}_{ij}\| , \quad q_{ij} \equiv \left(\tau-\bar{T}_{ij}\right)/\tau_\xi .$$

The reconstructed parameters are of a geometrical type. Because of the multi-extremality feature of such functions, global searching of the parameters, minimizing a residual function, is not the best way to solve the problem. So, we split the procedure into a sequence of sub-procedures (steps). Each step to the definite group of parameters estimation is defined. The method of choosing a group is the minimal dependence of it determination with respect to other groups. The received estimations in the next steps may be used. Such an approach makes it possible to take into account the specifics of a problem and the roles of different parameters in the correlation function.

First group of reconstructed parameters is the coordinates of the plume center, $\bar{r}$. Plume dimensions, Λ , forms the second group. As established in Section 1, for small plume-angle size, the maximum of the correlation moment approaches the artificial time delay (the same for all plume sizes), that compensates the time delay for the plume center. This allows for finding the plume center with high accuracy for unknown plume dimensions. Conversely, it allows the possibility for artificial compensation of the time delay for increasing the accuracy of determining plume dimensions in the next stage.

2.3. Bubble plume form reconstruction with a triangular receiver array

Let us consider an antenna array in the form of a triangle, i.e., three linear arrays of hydrophones. The plane of the triangle is assume to be the horizontal *xy*-plane. The center of the plume, *O*, is disposed at some unknown point, $(\bar{x},\bar{y},\bar{z})$, with relative linear dimensions $L_{1,2,3}$; the centers of the linear antennas (1,2,3) are disposed at known points, O_1, O_2, O_3 (see Fig. 6). Let the coordinates of hydrophones on linear antenna arrays be $\bar{x}_{1,2,3}(l)$, $\bar{y}_{1,2,3}(l)$, $l=\overline{1,2k}$. The hydrophone pairs l and $2k+1-l$ are symmetrical about the center of each antenna.

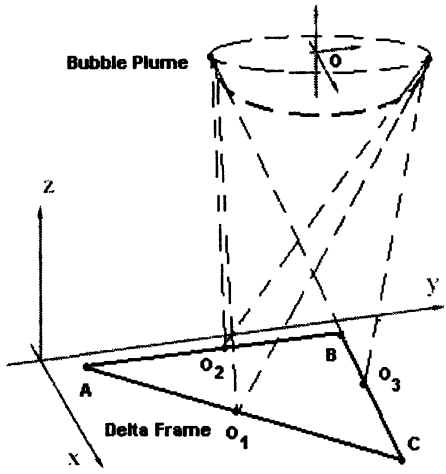

Figure 6. Delta-Frame antenna system for observing bubble plumes.

The plan of reconstruction of the plume parameters includes the four steps shown in Table I. We consider the four steps in detail in the following:

Table I: Procedures for reconstruction of plume parameters

Step	Procedure
1	Determination of the coordinates, $(\bar{x},\bar{y},\bar{z})$, of the plume center, O.
2	Estimations of relatives linear sizes of the plume $L_{1,2,3}$ in common planes of the plume center and linear antennas 1, 2, and 3, respectively.
3	Reconstruction of the original sizes and space orientation of the plume.
4	Correction of the plume parameter.

Step 1. *Determination of the coordinates,* $(\bar{x},\bar{y},\bar{z})$, *of the plume center, O.*

The time delays from the plume center, $\bar{r}_{1,2,3}(l)$, to the l hydrophone of this pair is

$$\Delta T_{1,2,3}(\bar{x},\bar{y},\bar{z};l) = \frac{\bar{r}_{1,2,3}(l)-\bar{r}_{1,2,3}(2k+1-l)}{\bar{c}} =$$

$$= \frac{1}{\bar{c}}\left(\sqrt{(\bar{x}-x_{1,2,3}(l))^2+(\bar{y}-y_{1,2,3}(l))^2+\bar{z}^2}-\sqrt{(\bar{x}-x_{1,2,3}(2k+1-l))^2+(\bar{y}-y_{1,2,3}(2k+1-l))^2+\bar{z}^2}\right).$$

We seek to minimize the function

$$F(x,y,z) =$$

$$= \sum_{l=1}^{k}\left[\left(\Delta T_1(x,y,z;l)-\Delta T_1^{(e)}(l)\right)^2+\left(\Delta T_2(x,y,z;l)-\Delta T_2^{(e)}(l)\right)^2+\left(\Delta T_3(x,y,z,l)-\Delta T_3^{(e)}(l)\right)^2\right],$$

where $\Delta T_{1,2,3}^{(e)}$ the measured (electronic) maximal time delays from the hydrophone pairs moment is maximal. This, of course, is possible only if the plume life is much greater than the integration time, T. The minimum value of this function provides the estimated location of the plume's center point, (x^*,y^*,z^*).

These measurements should be made in a wide band (for small value p), since, for narrowband measurements, the dependence of the correlative moment of q has multi-extremal character that leads to problems in measuring time delays.

Step 2. *Estimations of relatives linear sizes of the plume* $L_{1,2,3}$ *in common planes of the plume center and linear antennas 1, 2, and 3, respectively.*

Consider one of the linear antennas. Use the previously measured time delay, $\Delta T^{(e)}$, for *electronic steering* of antenna into its traverse planes. Then consider the pair of hydrophones with maximal base, $(1,2k)$. As follows from equations (2) and (11) for the respective time delays, the maximal value of the correlative moment is

$$k_{12k}^{\max} = k_{12k}^{(0)}\frac{1}{\sqrt{1+\nu^2\theta_{\max}^2}}\exp\left(\gamma_{\max}p^2\right)+Tg(d), \qquad (20)$$

where d is the antenna length, ν is the relative generalized size of the

plume in the plane of linear antenna and the plume center, $\gamma_{max} = -\nu^2\theta^2_{max}/(1+\nu^2\theta^2_{max})$, and θ_{max} is the angular size of antenna from the plume center. The angular size for the antenna can be can be determined from

$$\theta^2_{max}/2 = 1-\frac{(x^*-x_1)(x^*-x_{2k})+(y^*-y_1)(y^*-y_{2k})+z^{*2}}{r_1 r_{2k}},$$

$$r_1 = \sqrt{(x^*-x_1)^2+(y^*-y_1)^2+z^{*2}},$$
$$r_{2k} = \sqrt{(x^*-x_{2k})^2+(y^*-y_{2k})^2+z^{*2}},$$

once the center position of the plume is estimated (step 1).

Measuring values of k^{max}_{12k} for different p (by receiving signals through narrowband filters of width $1/\tau_\xi$ at different central frequencies, ω_0) we can estimate the informative parameter, $\nu\theta_{max}$. However, $k^{(0)}_{12}$ and $Tg(d)$ are unknown, and must be eliminated. In the case $\left|Tg(d)\sqrt{1+\nu^2\theta^2_{max}}\right| \ll k^{(0)}_{12}$ the function

$$\frac{k^{max}_{12k}(p)}{k^{max}_{12k}(p_1)} = \frac{\exp\left(\gamma_{max}p^2\right)+T\sqrt{1+\nu^2\theta^2_{max}}\,g(d)/k^{(0)}_{12}}{\exp\left(\gamma_{max}p_1^2\right)+T\sqrt{1+\nu^2\theta^2_{max}}\,g(d)/k^{(0)}_{12}} \approx \exp(\gamma_{max}(p^2-p_1^2)), \qquad (21)$$

where p_1 is a fixed value of p, may be considered. The coefficient γ_{max} can be determined by the method of least squares. If the correlation moment of the background noise, $Tg(d)$, can be measured, then greater accuracy can be obtained by the function

$$\frac{k^{max}_{12k}(p)-Tg(d)}{k^{max}_{12k}(p_1)-Tg(d)} = \exp(\gamma_{max}(p^2-p_1^2))$$

From this formula we find a generalized size

$$\nu\theta_{max} = \sqrt{-\frac{\gamma_{max}}{1+\gamma_{max}}},$$
$$L = \nu l_\xi .$$

Accordingly, the generalized sizes $L_{1,2,3}$ are found in this step.

Step 3. *Reconstruction of the original sizes and space orientation of the plume.*

In this step, plume dimensions and spatial orientation are determined. The general formulation of the problem is: For m given unit vectors (i.e., antennas orientations, three in our case), $e_i, i=\overline{1,m}$ and corresponding generalized dimensions, $L(e_i)$, the original dimensions of the plume (the diagonal of matrix C_0) and the plume's orientation in the space (matrix U) are to be determined. (See Appendix A for $C=U^*C_0U$.)

The problem may be transformed to solving of nonlinear algebraic system (Appendix A, Eq. (A.2))

$$\begin{cases} \langle Ue_1, C_0Ue_1 \rangle = L^2(e_1)/2 \\ \langle Ue_2, C_0Ue_2 \rangle = L^2(e_2)/2 \\ \dots \\ \langle Ue_m, C_0Ue_m \rangle = L^2(e_m)/2 \end{cases}$$

with respect to six unknown values, the ellipsoid axes and angles of its orientation. Here m is the number of the observations of the plume dimensions.

Denote $L^2(e_i)/2 \equiv l_i^2$ we then have for $m \geq 3$ the system for ellipsoid semi-axis, $\sigma_1, \sigma_2, \sigma_3$, given by

$$\begin{cases} \sigma_1^2 e_{11}^2 + \sigma_2^2 e_{12}^2 + \sigma_3^2 e_{13}^2 = l_1^2 \\ \sigma_1^2 e_{21}^2 + \sigma_2^2 e_{22}^2 + \sigma_3^2 e_{23}^2 = l_2^2 \\ \sigma_1^2 e_{31}^2 + \sigma_2^2 e_{32}^2 + \sigma_3^2 e_{33}^2 = l_3^2 , \end{cases} \tag{22}$$

where $e_{ij}, j=\overline{1,3}$ are coordinates of vector Ue_i in the fixed basis associated with the antenna.

Main determinant of the system is

$$\Delta = \begin{vmatrix} e_{11}^2 & e_{12}^2 & e_{13}^2 \\ e_{21}^2 & e_{22}^2 & e_{23}^2 \\ e_{31}^2 & e_{32}^2 & e_{33}^2 \end{vmatrix} = \begin{vmatrix} e_{11}^2 & e_{12}^2 & 1 \\ e_{21}^2 & e_{22}^2 & 1 \\ e_{31}^2 & e_{32}^2 & 1 \end{vmatrix} ,$$

and, for given coordinates e_{ij}, it is possible to find ellipsoid sizes from (23) by Cramer's rule:

$$\sigma_i^2 = \frac{\Delta_i}{\Delta}, \; i = \overline{1,3} \; . \tag{23}$$

In general case, however, the orientation of the ellipsoid, U, is not fully known, so the righthand parts of (23) depend on unknown parameters of matrix U. In this case (23) may be used for obtaining partial information of the ellipsoid parameters. Let us, for example, consider a horizontally oriented ellipsoid (i.e., two of its axis are situated in the horizontal plane). In this case operator U is a rotation in horizontal plane. It may be defined by a single parameter, for example e_{11} .

- Let $m=2$ and unit vectors $e_{1,2}$ are orthogonal to each other and lay in horizontal plane. These conditions is fulfilled for cross antenna, when the angle between axe OO_1 and vertical is small enough. Then $e_{13} \simeq 0$, $e_{23} \simeq 0$, so from (22) we receive the system

$$\begin{cases} \sigma_1^2 e_{11}^2 + \sigma_2^2 e_{12}^2 \simeq l_1^2 \\ \sigma_1^2 e_{21}^2 + \sigma_2^2 e_{22}^2 \simeq l_2^2 \end{cases} \tag{24}$$

Lengths and orthogonality of vectors Ue_1, Ue_2 is retained, then

$$e_{11}^2 = e_{22}^2 \; , \quad e_{21}^2 = e_{12}^2 \; ,$$
$$e_{11}^2 + e_{21}^2 = e_{12}^2 + e_{22}^2 = 1$$

and from (24) it follows

$$\sigma_1^2 \simeq \frac{l_1^2 - t l_2^2}{1-t} \; ,$$
$$\sigma_2^2 \simeq \frac{l_2^2 - t l_1^2}{1-t} \; , \tag{25}$$

where unknown parameter $t = 1/e_{11}^2 - 1$ defines ellipsoid turn in horizontal plane.

By summation of expressions in (25) we receive the estimations of ellipsoid sizes

$$\sigma_1^2+\sigma_2^2 \simeq l_1^2+l_2^2 ,$$

so

$$\sigma_{1,2}^2 \le l_1^2+l_2^2 .$$

As right parts of (25) must be positive, then we can do the following estimations of unknown parameter t also

$$t \le t^* \text{ or } t \ge 1/t^* ,$$

where $t^* = \min(l_1^2,l_2^2)/\max(l_1^2,l_2^2)$. For the angle of ellipsoid rotation φ ($e_{11}=\cos\varphi$) we receive the respective inequalities

$$\cos\varphi \ge \sqrt{\frac{l_{\max}^2}{l_1^2+l_2^2}} \quad \text{or} \quad \cos\varphi \le \sqrt{\frac{l_{\min}^2}{l_1^2+l_2^2}} .$$

- Let m=3 and units vectors $e_{1,2,3}$ lay nearly in horizontal plane. These conditions is fulfilled for any antenna of triangle form, when the angle between axes O_iO and vertical is small enough. As $e_{i3} \simeq 0$ for all i, then (22) transforms to

$$\begin{cases} \sigma_1^2 e_{11}^2+\sigma_2^2 e_{12}^2 \simeq l_1^2 \\ \sigma_1^2 e_{21}^2+\sigma_2^2 e_{22}^2 \simeq l_2^2 \\ \sigma_1^2 e_{31}^2+\sigma_2^2 e_{32}^2 \simeq l_3^2 \end{cases}$$

or

$$\begin{cases} \Delta\sigma^2 e_{11}^2+\sigma_2^2 = l_1^2 \\ \Delta\sigma^2 e_{21}^2+\sigma_2^2 = l_2^2 \\ \Delta\sigma^2 e_{31}^2+\sigma_2^2 = l_3^2 , \end{cases} \qquad (26)$$

where $\Delta\sigma^2 \equiv \sigma_1^2-\sigma_2^2$. Let

$$\begin{aligned} e_{11} &= \cos\varphi \\ e_{21} &= \cos(\varphi+\alpha) \\ e_{31} &= \cos(\varphi-\beta) , \end{aligned}$$

where the parameter φ defines the ellipsoid orientation with respect to antenna, α, β are closed to external angles of the antenna triangle.

Excluding unknowns $\Delta\sigma^2, \sigma_2^2$ from (26), we receive the equation

$$t^2 - t\frac{(l_3^2-l_1^2)\sin 2\alpha+(l_2^2-l_1^2)\sin 2\beta}{(l_3^2-l_1^2)\sin^2\alpha+(l_1^2-l_2^2)\sin^2\beta} - 1 = 0$$

for $t = \mathrm{tg}\varphi$. So,

$$\mathrm{tg}2\varphi = \frac{2\mathrm{tg}\varphi}{1-\mathrm{tg}^2\varphi} = 2\frac{(l_3^2-l_1^2)\sin^2\alpha+(l_1^2-l_2^2)\sin^2\beta}{(l_3^2-l_1^2)\sin 2\alpha+(l_2^2-l_1^2)\sin 2\beta}$$

The solution of this equation is

$$\varphi = \frac{1}{2}\mathrm{arctg}\left[2\frac{(l_3^2-l_1^2)\sin^2\alpha+(l_1^2-l_2^2)\sin^2\beta}{(l_3^2-l_1^2)\sin 2\alpha+(l_2^2-l_1^2)\sin 2\beta}\right]+\frac{\pi}{2}m ,$$

where m is an integer number for which φ belongs to the interval $\left(-\frac{\pi}{2}, \frac{\pi}{2}\right)$. Then from (26)

$$\begin{aligned}\sigma_1^2 &= l_1^2 - \frac{l_2^2-l_1^2}{\sin(2\varphi+\alpha)\sin\alpha}\sin^2\varphi ,\\ \sigma_2^2 &= l_1^2 + \frac{l_2^2-l_1^2}{\sin(2\varphi+\alpha)\sin\alpha}\cos^2\varphi .\end{aligned} \qquad (27)$$

If, for example, $l_1^2 = l_2^2$, then $\varphi = \alpha/2$. So, one of horizontal ellipsoid axes is directed along bisectrix of the external angle α of antenna triangle.

In particular case, for antenna in right triangle form, when $\alpha = \beta = 2\pi/3$, formulas (27) are simplified:

$$\varphi = \frac{1}{2}\operatorname{arctg}\left[\sqrt{3}\frac{l_3^2-l_2^2}{l_2^2+l_3^2-2l_1^2}\right]+\frac{\pi}{2}m\ ,$$

$$\sigma_1^2 = l_1^2-\frac{2}{\sqrt{3}}\frac{l_2^2-l_1^2}{\sin\left(2\varphi+\frac{2\pi}{3}\right)}\sin^2\varphi\ ,$$

$$\sigma_2^2 = l_1^2+\frac{2}{\sqrt{3}}\frac{l_2^2-l_1^2}{\sin\left(2\varphi+\frac{2\pi}{3}\right)}\cos^2\varphi\ .$$

So, reconstruction of the horizontal ellipsoid sizes is possible with triangle antenna system.

Step 4. *Correction of the plume parameter.*

In this step we can do a local search of the plume parameters in the neighborhood of the acquired approximations. This gives next approximation to the plume parameters. A schema for a possible receiving system is presented in Fig. 7.

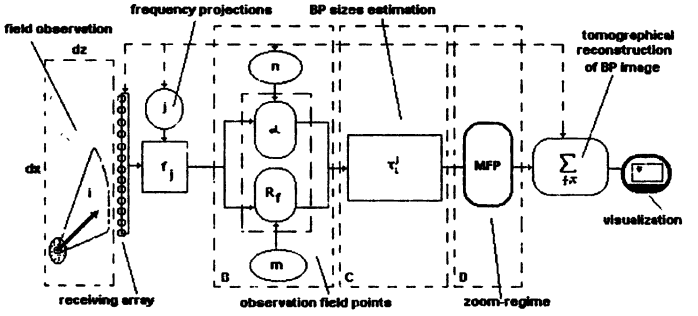

Figure 7. Schema of bubbles plume reconstruction.

2.4. Numerical simulation of plume reconstruction

Numerical simulations were made for realizing the above multi-step process of plume reconstruction. A equilateral triangular array of three linear antenna with 10-m side was considered. One of it sides was parallel to the *x*-axis of the coordinate system with the origin at the triangle center.

The plume was of ellipsoid form with axes $\sigma_1 = 1.5, \sigma_2 = 0.3, \sigma_3 = 0.3$. The angle between the plume's first axis and the x-axis is denoted by φ. The correlation function of random background noise was assumed to be of the form

$$g(|\boldsymbol{R}_1 - \boldsymbol{R}_2|) = \sigma_{bn} \exp(|\boldsymbol{R}_1 - \boldsymbol{R}_2| / l_{bn}) ,$$

where σ_{bn} is the intensity and l_{bn} is the spatial scale of the noise.

Some results of the simulation are represented in the following figures. Two pairs of positions and orientations, ($\bar{x}$=0, $\bar{y}$=0) , φ=π/7(=0.449) and ($\bar{x}$=3, $\bar{y}$=−3), φ=π/6(=−0.524), respectively, were considered. In both cases the plume center is 20 m above the frame. Images of the original two plumes in the xy-plane are shown in Fig. 8. Figures 9 to 13 show the reconstructions under various specified parameters for given intensities and noise scales along with the resulting estimated values of the plume axes and orientation.

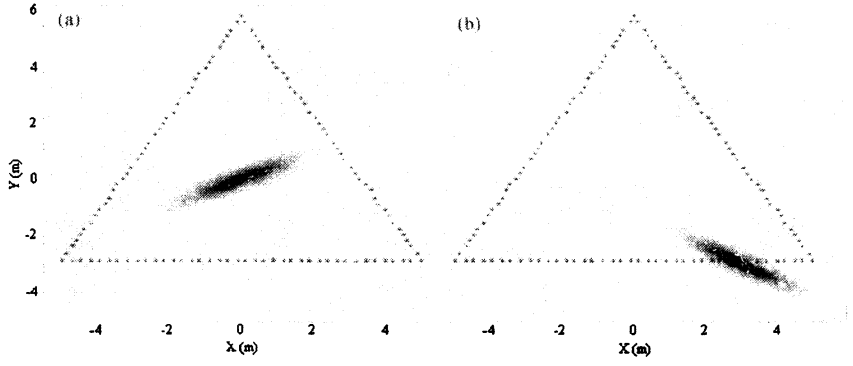

Figure 8. The original plumes defined by the parameters:
(a) $\bar{x}$=0, $\bar{y}$=0, φ=π/7(=0.449) and (b) $\bar{x}$=3, $\bar{y}$=−3, φ=−π/6(=−0.524) .

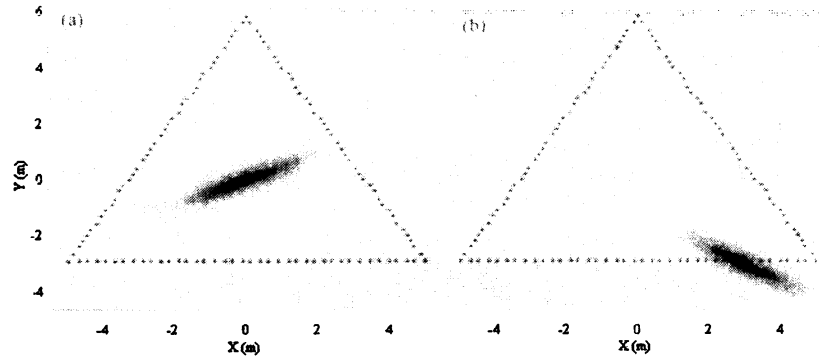

Figure 9. Plume reconstructions intensity and noise scale σ_{bn} = 0, l_{bn} = 1 with the resulting determined plume parameters: (a) σ_1=1.5, σ_2=0.3, φ=0.449 (b) σ_1=1.499, σ_2=0.310, φ=−0.538 .

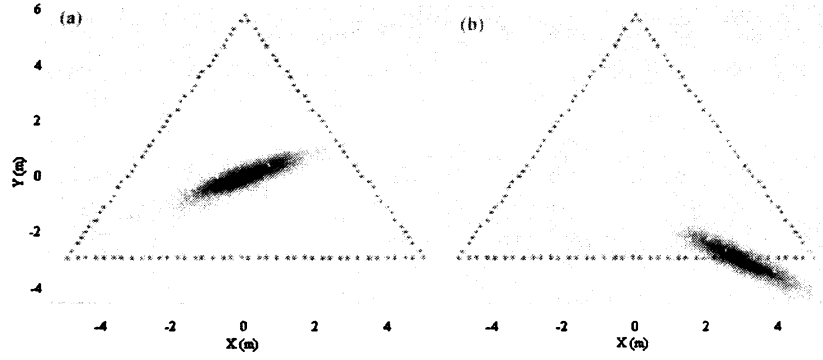

Figure 10. Plume reconstructions intensity and noise scale σ_{bn} = 1, l_{bn} = 1 σ_{bn} = 0, l_{bn} = 1 with the resulting determined plume parameters: (a) σ_1=1.481, σ_2=0.297, φ=0.449 (b) σ_1=1.480, σ_2=0.307, φ=−0.537 .

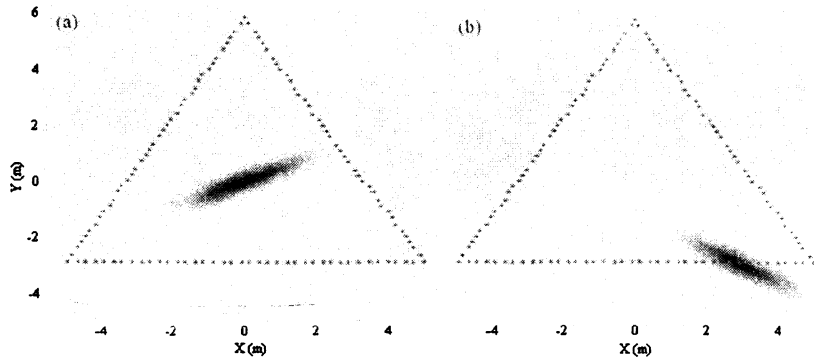

Figure 11. Plume reconstructions intensity and noise scale $\sigma_{bn} = 5$, $l_{bn} = 1$ with the resulting determined plume parameters: (a) $\sigma_1 = 1.411$, $\sigma_2 = 0.288$, $\varphi = 0.451$ (b) $\sigma_1 = 1.408$, $\sigma_2 = 0.295$, $\varphi = -0.534$.

When background noise was small the accuracy of reconstructing plume parameters was very high, especially over the center of the antenna. The inclination of the $e_{1,2,3}$ -plane to the plume (see Section 2.3) tends to decreasing the accuracy of (27) when the plume is not over the center of the triangle. When background noise was high the accuracy of reconstructing plume parameters was poor. Most of all the accuracy relates to the plume generalized sizes, that were determined by formula (21). At the same time the accuracy of the plume center and orientation determination was very high for all levels of noise.

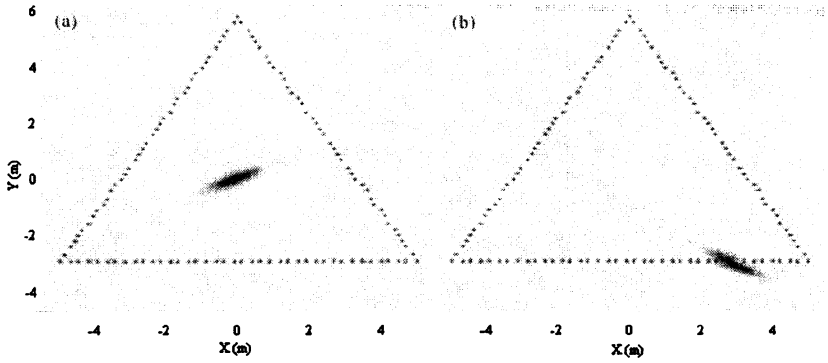

Figure 12. Plume reconstructions intensity and noise scale $\sigma_{bn} = 1$, $l_{bn} = 2$ with the resulting determined plume parameters: (a) σ_1=0.685, σ_2=0.155, φ=0.461 (b) σ_1=0.676, σ_2=0.154, φ=−0.507 .

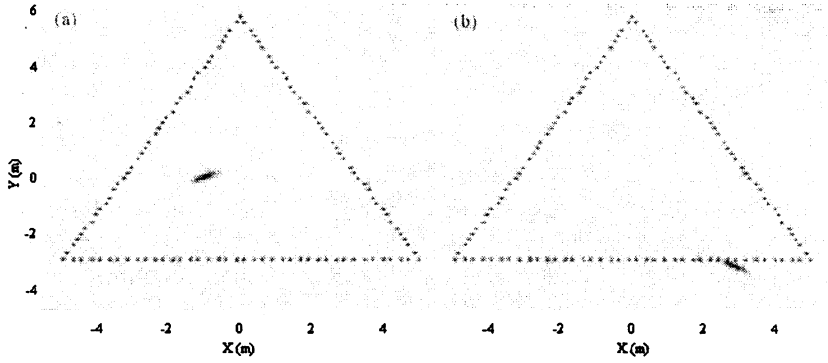

Figure 13. Plume reconstructions intensity and noise scale $\sigma_{bn} = 5$, $l_{bn} = 2$ with the resulting determined plume parameters: (a) σ_1=0.340, σ_2=0.774, φ=0.463 (b) σ_1=0.335, σ_2=0.770, φ=−0.504 .

2.5. Bubble Plume Size Determination with a Linear Array

Let the antenna line (x-axis) be orthogonal to OO_1, where O_1 and O are central points of the antenna and the plume, respectively, and the π-plane contain the x-axis and the line OO_1 (cf. Fig. 14). Let ϑ_i be the angle in the π-plane subtending the ith pair of hydrophones $(-x_i, x_i)$ as seen from the center of the plume. The angle ϑ_i takes on the discrete values

$\vartheta_i = \vartheta_{min} + i\Delta\vartheta$, $(\vartheta_{min} < \vartheta_i < \vartheta_{max})$.

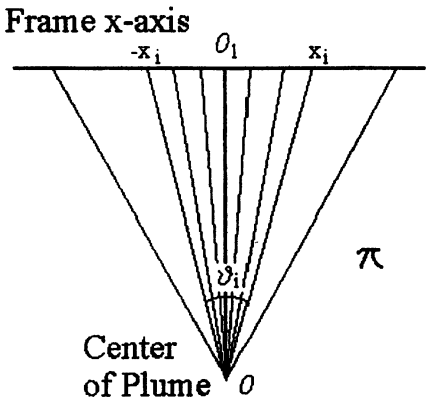

Figure 14. Observation of the bubble plume from the receivers on the x-axis.

Assuming $v\vartheta_{min} \ll 1$, we obtain from (11) the relative value of the correlative moment for the ith pair,

$$g(\vartheta_i^2) \equiv k_{12}^{max}(\vartheta_i)/k_{12}^{max}(\vartheta_{min}) \simeq \frac{1}{\sqrt{1+v^2\vartheta_i^2}} \exp\left(-\frac{v^2\vartheta_i^2 p^2}{1+v^2\vartheta_i^2}\right) .$$

After summing these values weighted by $2\vartheta_i\Delta\vartheta$ we obtain

$$\sum_i 2\vartheta_i g(\vartheta_i^2)\Delta\vartheta \simeq \int_{\vartheta_{min}}^{\vartheta_{max}} \frac{2\vartheta}{\sqrt{1+v^2\vartheta^2}} \exp\left(-\frac{v^2\vartheta^2 p^2}{1+v^2\vartheta^2}\right) d\vartheta = e^{-p^2} \int_{\vartheta_{min}^2}^{\vartheta_{max}^2} \frac{1}{\sqrt{1+v^2 u}} \exp\left(\frac{p^2}{1+v^2 u}\right)$$

$$= \frac{2pe^{-p^2}}{v^2}\left(\Phi\left(\sqrt{\frac{1+v^2\vartheta_{max}^2}{p^2}}\right) - \Phi\left(\sqrt{\frac{1+v^2\vartheta_{min}^2}{p^2}}\right)\right) = \tag{28}$$

$$= \frac{2p^3 e^{-p^2}}{\varpi^2}\left(\Phi\left(\sqrt{\frac{p^2+a_{max}^2}{p^4}}\right) - \Phi\left(\sqrt{\frac{p^2+a_{min}^2}{p^4}}\right)\right) ,$$

where

$$\varpi \equiv \frac{\omega_0 L}{2\bar{c}}, \quad a_{\min,\max} = \varpi \vartheta_{\min,\max},$$

$$\Phi(s) = \int_1^s \exp\left(\frac{1}{w^2}\right) dw .$$

Plots of the special functions $\Phi(s)$ and

$$f(p) = p^3 e^{-p^2}\left(\Phi\left(\sqrt{\frac{p^2+a_{\max}^2}{p^4}}\right) - \Phi\left(\sqrt{\frac{p^2+a_{\min}^2}{p^4}}\right)\right) \tag{29}$$

for given values $a_{\max} \gg a_{\min}$ are represented in Figs. 15 and 16.

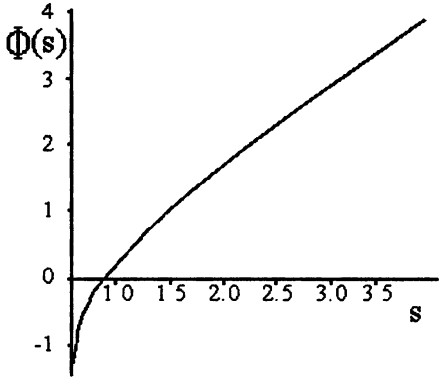

Figure 15. Plot of the special function defined in Eq. (28).

Then taking into account real estimations of parameters

$$\varpi = \frac{\omega_0 L}{2\bar{c}} \simeq 1 ,$$

$$a_{\max} = \varpi \vartheta_{\max} \simeq 1 ,$$

$$p = \frac{\omega_0 \tau_\xi}{2} \simeq 1$$

we can replace (29) with its limit for $p \to \infty$ (see plots).

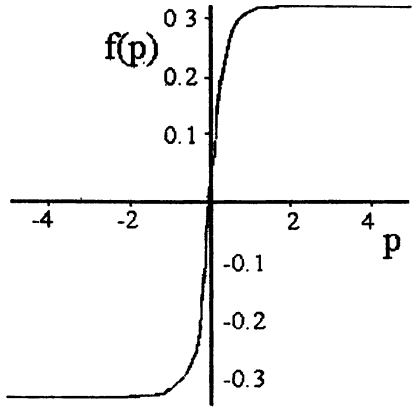

Figure 16. Plot of the special function defined in Eq. (29) for $a_{max}=1$, $a_{min}=0.01$.

For any fixed value a^2 we can obtain the limit by the L'Hopital rule

$$\lim_{p\to\infty}\frac{p^3\Phi\left(\sqrt{\frac{p^2+a^2}{p^4}}\right)}{e^{p^2}} = \lim_{p\to\infty}\frac{3p^2\Phi\left(\sqrt{\frac{p^2+a^2}{p^4}}\right)-p^3\exp\left(\frac{p^4}{p^2+a^2}\right)\frac{(p^2+2a^2)}{p^3\sqrt{p^2+a^2}}}{2pe^{p^2}} =$$

$$= -\frac{1}{2}\lim_{p\to\infty}\frac{1+2(a/p)^2}{\sqrt{1+(a/p)^2}}\exp\left(p^2\left(\frac{p^2}{p^2+a^2}-1\right)\right) = -\frac{\exp(-a^2)}{2} .$$

So for $p\gg 1$

$$f(p) \approx p^3 e^{-p^2}\left(\Phi\left(\frac{\sqrt{p^2+a_{max}^2}}{p^2}\right)-\Phi\left(\frac{\sqrt{p^2+a_{min}^2}}{p^2}\right)\right) \simeq \frac{\exp\left(-a_{min}^2\right)-\exp\left(-a_{max}^2\right)}{2} .$$

$$G \sim \frac{\exp\left(-\varpi^2\vartheta_{min}^2\right)-\exp\left(-\varpi^2\vartheta_{max}^2\right)}{\varpi^2} \equiv f_1(\varpi) \qquad (30)$$

As $f'_1<0$, then the function $f_1(x)$ is monotone decreasing for $x>0$, so it is invertible, and we can write

$$\varpi = f_1^{-1}(G) ,$$
$$L = \frac{2\bar{c}}{\omega_0} f_1^{-1}(G) ,$$

where f_1^{-1} is the inverse function.

When $\varpi^2 \vartheta_{min}^2 \ll 0$, $\varpi^2 \vartheta_{max}^2 > 1$ and $G \approx 1/\varpi^2$, we have the simple formula, $L \approx 2\bar{c}/(\omega_0 \sqrt{G})$, for the size of the plume.

ACKNOWLEDGMENTS

This work was supported, in part, by the Ocean Acoustics Program (Code 321), by the European Office of the US Office of Naval Research and by Russian Foundation for Basic Recearch under Grant № 97-02-17536.

APPENDICES

A. Mutual Correlation Moment for a Bubble Plume of Gaussian Form

After substitution (7) and (8) to (4), we shall obtain

$$k_{12}(0) \approx k_{12}^{(0)} \sqrt{\frac{1}{8\pi^3 \det\Lambda}}\, \Re \iiint \exp\left(-\left(\frac{\bar{T}_{12}}{\tau_\xi} + \frac{(r;e)}{l_\xi} \right)^2 + i\omega_0 (\bar{T}_{12} + \frac{(r;e)}{\bar{c}}) - \frac{1}{2}(r;(\Lambda^{-1}+G)r) \right)$$

$$= k_{12}^{(0)} \sqrt{\frac{1}{8\pi^3 \det\Lambda}}\, \Re \exp\left(-\frac{\bar{T}_{12}^2}{\tau_\xi^2} + i\omega_0 \bar{T}_{12} \right) J \,, \qquad \text{(A.1)}$$

$$J \equiv \iiint \exp\left(\left(i\omega_0 - \frac{2\bar{T}_{12}}{\tau_\xi^2} \right) \frac{(r;e)}{\bar{c}} - \frac{(r;e)^2}{l_\xi^2} - \frac{1}{2}(r;(\Lambda^{-1}+G)r) \right) dr \,,$$

where $k_{12}^{(0)} \equiv A_1 A_2 N W_0$, $l_\xi \equiv \bar{c}\tau_\xi$.

For integral J calculation let introduce matrixes

$$E \equiv 2 l_\xi^{-2} e e^* \,,$$
$$C^{-1} \equiv \Lambda^{-1} + G \,,$$
$$D \equiv (C^{-1} + E)^{-1} \,,$$

where e^* is the transposed row vector e . Note, that matrixes C and D are symmetrical, positive definite (so, are invertible). Symmetrical, non negative definite matrix E has the single rank.

Then, $2 l_\xi^{-2}(r;e)^2 + (r;(\Lambda^{-1}+G)r) = (r;Er) + (r;C^{-1}r) = (r;D^{-1}r)$ and using of Poisson integral we obtain

$$J = \iiint \exp(i(r;k)) \exp\left(-\frac{1}{2}(r;D^{-1}r) \right) dr = \bar{f}(k)\sqrt{(2\pi)^3 \det D},$$

where

$$k \equiv \left(\frac{\omega_0}{\bar{c}} + i\frac{2\bar{\tau}_{12}}{\bar{c}\tau_\xi^2} \right) e \,,$$

$$\bar{f}(k) \equiv \exp\left(-\frac{1}{2}(k;Dk) \right) = \exp\left(-\frac{1}{2}\left(\frac{\omega_0}{\bar{c}} + i\frac{2\bar{\tau}_{12}}{\bar{c}\tau_\xi^2} \right)^2 (e;De) \right).$$

After substitution of the found value J to (A.1) and some simple calculations we have the next expression for the moment k_{12} :

$$k_{12}(0) = k_{12}^{(0)}\sqrt{\frac{\det D}{\det\Lambda}}\exp\left(-\frac{\bar{\tau}_{12}^2}{\tau_\xi^2}-\frac{\omega_0^2\kappa}{2\bar{c}^2}(e;De)\right)\cos\left(\omega_0\bar{\tau}_{12}-2\omega_0\bar{\tau}_{12}l_\xi^{-2}(e;De)\right),$$

where $\kappa \equiv 1-4(\bar{\tau}_{12}/\tau_\xi)^2(\omega_0\tau_\xi)^{-2}$.

With a view of further simplification of the received expression for the correlative moment let use the next formula (see [23, p. 33 number 4.61])

$$D = (C^{-1}+E)^{-1} = C-\beta CEC ,$$
$$\beta \equiv (1+2l_\xi^{-2}(e;Ce))^{-1} ,$$

(it is implemented for any positive definite matrix C and for any matrix E of special above described type).

Fulfilling transformations, we receive

$$(e;De) = (e;Ce)-\beta(e;CECe) = (e;Ce)-\frac{1}{1+2l_\xi^{-2}(e;\tilde{N}e)}(Ce;Ece) =$$
$$= (e;Ce)-\frac{2l_\xi^{-2}(e;Ce)^2}{1+2l_\xi^{-2}(e;Ce)} = \frac{(e;Ce)}{1+2l_\xi^{-2}(e;Ce)} = \beta(e;Ce) .$$

Hence,

$$\frac{\bar{\tau}_{12}^2}{\tau_\xi^2}+\frac{\omega_0^2\kappa}{2\bar{c}^2}(e;De) = \frac{\bar{\tau}_{12}^2}{\tau_\xi^2}+\frac{\omega_0^2}{2\bar{c}^2}\left(1-4(\bar{\tau}_{12}/\tau_\xi)^2(\omega_0\tau_\xi)^{-2}\right)\beta(e;Ce) =$$
$$= \beta\left(\frac{\bar{\tau}_{12}^2}{\tau_\xi^2}+\frac{\omega_0^2}{2\bar{c}^2}(e;Ce)\right) ,$$

$$\omega_0\bar{\tau}_{12}-2\omega_0\bar{\tau}_{12}l_\xi^{-2}(e;De) = \omega_0\bar{\tau}_{12}\left(1-2l_\xi^{-2}\beta(e;Ce)\right) = \omega_0\beta\bar{\tau}_{12} ,$$

$$\frac{\det D}{\det \Lambda} = \det(C-\beta CEC)\det(\Lambda^{-1}) = \det(C-\beta CEC)\det(C^{-1})\det(\Lambda^{-1}C) =$$
$$= \det(I-\beta EC)\det(C\Lambda^{-1}) = \gamma\det(I-\beta EC) ,$$

where I is the identity matrix,

$$\gamma \equiv \det(\Lambda^{-1}C) = 1/\det(I+\Lambda G) .$$

Let calculate determinant $\det(I-\beta EC)$. Omitting signs of summation with respect to repeating indexes symbol, we have

$$\det(I-\beta EC) = \det(I-\sigma ee^T C) = \begin{vmatrix} 1-\sigma e_1 e_k C_{kl} & -\sigma e_1 e_m C_{m2} & -\sigma e_1 e_{jC_{j3}} \\ -\sigma e_2 e_k C_{kl} & 1-\sigma e_2 e_m C_{m2} & -\sigma e_2 e_j C_{j3} \\ -\sigma e_3 e_k C_{kl} & -\sigma e_3 e_m C_{m2} & 1-\sigma e_1 e_j C_{j3} \end{vmatrix} ,$$

where $\sigma \equiv 2\beta l_\xi^{-2}$. And, finally,

$$\det(I-\beta EC) = 1-\sigma(e_1 e_k C_{kl}+e_2 e_m C_{m2}+e_3 e_j C_{j3}) = 1-\sigma(e;Ce) = \beta ,$$

Now the expression for integral correlative moment become rather simple:

$$k_{12}(0) = k_{12}^{(0)}\sqrt{\beta\gamma}\exp\left(-\beta\left(\frac{\bar{\tau}_{12}^2}{\tau_\xi^2}+\frac{\omega_0^2}{2\bar{c}^2}(e;Ce)\right)\right)\cos\omega_0\beta\bar{\tau}_{12} .$$

Let represent (see [23]) symmetric positive definite matrix C in the form $C=U^*C_0U$, where C_0 is a diagonal matrix with eigenvalues $\sigma_1^2,\sigma_2^2,\sigma_3^2$ of matrix C_0 in diagonal, and U^* is orthogonal matrix of rotation to coordinate system with axes, directed along eigenvectors of matrix C. Then $(e;Ce)$ can be then represented in the form

$$(e;Ce) = \|e\|^2(\tilde{e};C\tilde{e}) = \|e\|^2(\tilde{e};U^TC_0U\tilde{e}) = \|e\|^2(U\tilde{e};C_0U\tilde{e}) .$$

The value

$$L(\tilde{e}) \equiv \sqrt{2(U\tilde{e};C_0U\tilde{e})} \qquad (A.2)$$

belongs to segment $[\sigma_{min},\sigma_{max}]$, where

$$\sigma^2_{min} \equiv 2\min\{\sigma_1^2,\sigma_2^2,\sigma_3^2\} ,$$
$$\sigma^2_{max} \equiv 2\max\{\sigma_1^2,\sigma_2^2,\sigma_3^2\} ,$$

and (in case $G=0$) characterizes the magnitude of the plume in direction of unit vector $\tilde{e}$ [4] . In particular, when this vector is parallel with principal axis of the ellipsoid, (A.2) is equal to the length of corresponding semi-axis. Granting this we call $L(\tilde{e})$ by *generalized size of the plume* in direction of vector $\tilde{e}$. For example for sphere with $\sigma_1^2 = \sigma_2^2 = \sigma_3^2 = 2r_0^2$ we have $L(\tilde{e}) \equiv 2r_0$ for any unit vector $\tilde{e}$.

Introducing parameters

$$p \equiv \frac{\omega_0\tau_\xi}{2}, \; l_\xi \equiv \bar{c}\tau_\xi ,$$
$$\nu \equiv \frac{L(\tilde{e})}{l_\xi}, \; q \equiv \frac{\bar{\tau}_{12}}{\tau_\xi} ,$$
$$\vartheta \equiv \|e\| \equiv \left|2\sin\frac{\varphi}{2}\right|,$$

and taking into account the equality

$$\beta \equiv \frac{1}{1+\nu^2\vartheta^2} ,$$

we obtain the final representation for integral correlative moment

---

[4] In the small angles approach we can assume that vector $\tilde{e}$ is directed along traverse line, i.e. is orthogonal to the line connecting central points of the plum and antenna and lying in common plane of center and hydrophones.

$$k_{12}(0) = k_{12}^{(0)}\sqrt{\beta\gamma}\exp\left(-\beta\left(\frac{\bar{\tau}_{12}^2}{\tau_\xi^2}+\frac{\omega_0^2 L^2(\bar{e})}{4\bar{c}^2}\|e\|^2\right)\right)\cos(\omega_0\beta\bar{\tau}_{12}) =$$

$$= k_{12}^{(0)}\sqrt{\frac{\gamma}{1+v^2\vartheta^2}}\exp\left(-\frac{q^2+p^2v^2\vartheta^2}{1+v^2\vartheta^2}\right)\cos\frac{2pq}{1+v^2\vartheta^2} = \qquad (A.3)$$

$$= k_{12}^{(0)}\sqrt{\beta\gamma}\exp(-\beta q^2-(1-\beta)p^2)\cos 2\beta pq\ .$$

B. Mutual Correlation moment for Bubble plume of non-Gaussian Form

Consider only the case G=0 in formula (9), that corresponds to pulses with equal energies, let calculate the integral moment for function (13):

$$k_{12}(0) \sim k_{12}^{(0)}\tilde{C}\,\Re\iiint(r;Qr)\exp\left(-\left(\frac{\bar{\tau}_{12}}{\tau_\xi}+\frac{(r,e)}{l_\xi}\right)^2+i\omega_0\left(\bar{\tau}_{12}+\frac{(r,e)}{\bar{c}}\right)-\frac{1}{2}(r;C^{-1}r)\right)dr =$$

$$= k_{12}^{(0)}\tilde{C}\,\Re\,\exp\left(-\frac{\bar{\tau}_{12}^2}{\tau_\xi^2}+i\omega_0\bar{\tau}_{12}\right)J\ , \qquad (B.1)$$

$$J \equiv \iiint(r;Qr)\,\exp\left(\left(i\omega_0-\frac{2\bar{\tau}_{12}}{\tau_\xi^2}\right)\frac{(r,e)}{\bar{c}}-\frac{(r,e)^2}{l_\xi^2}-\frac{1}{2}(r;C^{-1}r)\right)dr\ .$$

For calculation of integral J let (by analogy with Appendix A) introduce symmetrical matrixes $E = 2l_\xi^{-2}ee^*$ and

$$D = (C^{-1}+E)^{-1} = C-\beta CEC\ ,$$

$$\beta \equiv \frac{1}{1+2l_\xi^{-2}(e;Ce)}\ ,$$

where e^* is the transposed row vector e. Then the integral can be written in the form

$$J \equiv \iiint(r;Qr)\exp\left((r;v)-\frac{1}{2}(r;D^{-1}r)\right)dr\ ,$$

$$v \equiv \left(i\frac{\omega_0}{\bar{c}}-\frac{2\bar{\tau}_{12}}{\bar{c}\tau_\xi^2}\right)e\ .$$

Introducing the vector

$$v_1 \equiv \left(\frac{D^{-1}+D^{-1T}}{2}\right)^{-1} v = Dv, \quad t \equiv r - v_1 ,$$

we have

$$(r;v) - \frac{1}{2}(r;D^{-1}r) = -\frac{1}{2}(t;D^{-1}t) + \frac{1}{2}(v_1;D^{-1}v_1)$$

and

$$J\exp\left(-\frac{1}{2}(v;Dv)\right) = \iiint (r;Qr)\exp\left(-\frac{1}{2}(r-v_1;D^{-1}(r-v_1))\right)dr =$$

$$= \iiint (t;Qt)\exp\left(-\frac{1}{2}(t;D^{-1}t)\right)dt - (v_1;Qv_1)\iiint \exp\left(-\frac{1}{2}(t;D^{-1}t)\right)dt =$$

$$= \left(\mathrm{Tr}(DQ) - (Dv;Qdv)\right)\sqrt{(2\pi)^3 \det D} .$$

So,

$$J = \left(\mathrm{Tr}(DQ) - (Dv;Qdv)\right)\sqrt{(2\pi)^3 \det D}\exp\left(\frac{1}{2}(v;Dv)\right) =$$

$$= \sqrt{(2\pi)^3 \det D}\left(\mathrm{Tr}(Q^{*}D) - (Dv;QDv)\right) .$$

Substituting this value to (B.1), we'll find the integral correlative moment. Taking into account awkwardness of this expression in common case we consider the case $C = r_0^2 I/2$ only. In this case

$$k_{12}(0) = k_{12}^{(0)}\frac{2\sqrt{\beta}}{r_0^2 \mathrm{Tr}Q}\exp\left(-\beta\left(\frac{\bar{\tau}_{12}^2}{\tau_\xi^2} + \frac{\omega_0^2 r_0^2}{4c^2}\|e\|^2\right)\right) \times$$

$$\times \left(\left(\mathrm{Tr}(DQ) + \delta\left(\frac{\omega_0^2}{c^2} - \frac{4\bar{\tau}_{12}^2}{l_\xi^2 \tau_\xi^2}\right)\right)\cos\omega_0\beta\bar{\tau}_{12} - \frac{\omega_0\bar{\tau}_{12}\delta}{l_\xi^2}\sin\omega_0\beta\bar{\tau}_{12}\right) ,$$

$$\delta = (De;Qde) .$$

If besides $Q=I$, then

$$\mathrm{Tr}(DQ) = \mathrm{Tr}D = \frac{r_0^2}{2}\mathrm{Tr}\left(I-\beta v^2 ee^*\right) = \frac{r_0^2}{2}(2+\beta)\ ,$$

$$\delta = (De;De) = \frac{r_0^4}{4}\left\|\left(I-\beta v^2 ee^*\right)e\right\|^2 = \frac{r_0^4}{4}\beta^2\|e\|^2\ ,$$

$$k_{12}(0) = \tfrac{1}{3}k_{12}^{(0)}\sqrt{\beta}\exp\left(-\beta q^2-(1-\beta)p^2\right)\times$$
$$\times\left((2+\beta+2(\beta-\beta^{-1})(p^2-q^2))\cos 2\beta pq\ -\ pq(\beta-\beta^{-1})\sin 2\beta pq\right)\ .$$

Parameters $p, q, \beta, v, \vartheta$ are the same as in Appendix A.

C. Mutual Correlation Moment for Multi-Ray Approach

Replacing, as in Appendix A, statistical averaging by mathematical form, we obtain formula

$$k_{12}(0) \sim N\sum_j\sum_{j'}A_{1j}A_{2j'}\iiint\left\langle\Psi_i\left(\bar{\tau}_{12}^{(jj')}+\frac{(r;e_{jj'})}{\bar{c}}\right)\right\rangle f(r)\,dr.$$

For pulses with equal energies, correlation function (7) and Gaussian form of the plume (8) we can receive the formula

$$k_{12}(0) = NW_0\sum_j\sum_{j'}A_{1j}A_{2j'}\upsilon_{jj'}\cos\left(\omega_0\bar{\tau}_{12}^{(jj')}+2\omega_0\bar{\tau}_{12}^{(jj')}l_\xi^{-2}(e_{jj'};D_{jj'}e_{jj'})\right)\ ,$$

where

$$\upsilon_{jj'} \equiv \sqrt{\frac{\det D_{jj'}}{\det C}}\exp\left(-\left(\bar{\tau}_{12}^{(jj')}/\tau_\xi\right)^2-\frac{\omega_0^2\gamma_{jj'}}{2\bar{c}^2}(e_{jj'};D_{jj'}e_{jj'})\right)\ ,$$
$$\gamma_{jj'} \equiv 1-4\left(\bar{\tau}_{12}^{(jj')}/\tau_\xi\right)^2(\omega_0\tau_\xi)^{-2}$$

$$D_{jj'} = (C^{-1}+E_{jj'})^{-1} = C-\beta_{jj'}CE_{jj'}C\ ,$$
$$\beta_{jj'} \equiv (1+2l_\xi^{-2}(e_{jj'};Ce_{jj'}))^{-1}\ .$$

After calculations we have

$$k_{12}(0) = NW_0 \sum_j \sum_{j'} A_{1j} A_{2j'} \sqrt{\beta_{jj'}} \times$$

$$\times \exp\left(-\beta_{jj'} \left(\left(\bar{\tau}_{12}^{(jj')} / \tau_\xi \right)^2 + \frac{\omega_0^2 L(\vec{e}_{jj'})}{4c^2} \|e_{jj'}\|^2 \right) \right) \cos\omega_0 \beta_{jj'} \bar{\tau}_{12}^{(jj')} =$$

$$= NW_0 \sum_j \sum_{j'} A_{1j} A_{2j'} \frac{1}{\sqrt{1+v_{jj'}^2 \vartheta_{jj'}^2}} \exp\left(-\frac{q_{jj'}^2 + p^2 v_{jj'}^2 \vartheta_{jj'}^2}{1+v_{jj'}^2 \vartheta_{jj'}^2} \right) \cos\frac{2pq_{jj'}}{1+v_{jj'}^2 \vartheta_{jj'}^2}$$

where $\vartheta_{jj'} \equiv \|e_{jj'}\|$, $q_{jj'} \equiv \bar{\tau}_{12}^{(jj')} / \tau_\xi$, $p \equiv \omega_0 \tau_\xi / 2$, $v_{jj'} \equiv L(\vec{e}_{jj'}) / l_\xi$.

REFERENCES

1. Kolaini, A.R. and Crum, L.A. Observation of underwater sound from laboratory breaking waves and the implications concerning ambient noise in the ocean // *J. Acoust. Soc. Am.* 1994. vol. 96(3). PP 1755-1765.
2. Farmer, D.M. and Ding, L. Coherent acoustical radiation from breaking waves // *J. Acoust. Soc. Am.*1992.vol. 92(1). PP.397-402.
3. Smirnov, I.P., Khil'ko, A.I. and Caruthers, J.W. Multiscale coherence of acoustical field of noise source in randomly inhomogeneous ocean // in *The Forming of Acoustical Fields in Oceanic Waveguides. Coherence Effects.* 1997. IAP RAS: Nizhny Novgorod. PP.150-193.
4. Yang, T.C..Broadband source localization and signature estimation.// *J. Acoust. Soc. Am.*1993. Vol. 93, PP.1797-1806,
5. Prosperetti, A. ,Lu, N.Q. and Kim, H.S..Active and Passive behavior of bubbles clouds at the ocean's surface.// *J. Acoust. Soc. Am.* 1993. Vol. 93. PP. 3117-3127.
6. Finette, S. and Heitmeyer, R.M Angle-time-frequency resolution of the noise field generated by wind-induced breaking waves.// *J. Acoust. Soc. Am.* 1996. Vol. 99(1). PP. 209-222.
7. Oguz, H.N. A theoretical study of low frequency oceanic ambient noise. // *J. Acoust. Soc. Am.*1994 Vol. 95. PP.1895-1912..
8. Loewen, M.R. and Melville, W.K. An experimental investigation of the collective oscillations of bubble plumes entrained by breaking waves // *J. Acoust. Soc. Am.*1994. Vol. 95(3). PP. 1329-1343.
9. Kerman, B.R. Underwater sound generation by breaking wind waves. // *J. Acoust. Soc. Am.*1984. Vol. 75(10). PP. 149-165.
10. Lamarre, E. and Melville, W.K..Void-fraction measurements and sound-speed fields in bubble plumes generated by breaking waves // *J. Acoust. Soc. Am.*1994. Vol. 95(3). PP. 1317-1328.
11. Oguz, H.N. Emission of sound by semi-submerged object in shallow water // *J. Acoust. Soc. Am.*1996. Vol. 100(1). PP.253-261.
12. Farmer, D.M. and Vagle, S. Waveguide propagation of ambient sound in the ocean-surface bubble layer // *J. Acoust. Soc. Am.*1989. Vol. 86(5). PP. 1897-1908.
13. Crowther, P.A. and Hansla, A. The lifetimes. velocities and probable origin of sonic and ultrasonic noise sources on the sea surface // in *Natural Physical Sources of Underwater Sound.* Kluwer: Netherlands.1993. PP. 379-392.

14. Updergraf, G.E. and Anderson, V.C.Bubble noise and wavelet spills recorded 1m below the ocean surface // *J. Acoust. Soc. Am.*1991. Vol. 89(5). PP. 2264-2279.
15. Dahl, P.H. High frequency noise emitted from breaking waves in sea surface sound // *1994: Third international Meeting on Natural Physical Processes Related to Sea Surface Sound.* World Scientific Press.1995. PP. 174-184.
16. Medwin, H. and Beaky, M.M. Bubble source of the Knudsen Sea noise spectra // *J. Acoust. Soc. Am.*1989. Vol. 86(3). PP. 1124-1130.
17. Carey, W.M. et. al. Measurements of the sound produced by a tipping through with fresh and salt water // *J. Acoust. Soc. Am.*1993. Vol. 93(6) PP. 3176-3192.
18. Minneart, M. On musical air-bubbles and the sounds of running water // *Phil. Mag.*1933. Vol. 16. PP. 235-248.
19. Haines, M.A. and Johnson, B.D. Injected bubble populations in seawater and fresh water measured by a photographic method // *J. Geophy. Res.*1995. Vol. 100(C4). PP. 7057-7068.
20. Pumphrey, H.C. and Elmore, P.A. The entrainment of bubbles by drop impacts // *J. of Fluid Mech.* 1990. Vol. 220. PP. 539-567.
21. Deane, G.B. Sound generation and air entrainment by breaking waves in the surf zone // unpublished.
22. Tihonov, A.N., Arsenin, V.Ja. and Timonov, A.A. *Mathematical Problems of Computerized Tomography* (in russian).1987.
23. Voevodin, V.V. and Kuznetsov, Yu.A. *Matrix Calculations.* Moscow: Nauka (in Russian). 1984.
24. Baggeroer, A.B., Kuperman, W.A. and Mikhalevsky, P.N. An overview of matched field methods in ocean acoustics // IEEE. J. Ocean. Eng. 1993. Vol. 18. PP. 401-424.

ABSTRACTS

Volume 1

E. Yu. Gorodetskaya (NN University), A. I. Malekhanov (IAP RAS), A. G. Sazontov (IAP RAS), N. K. Vdovicheva (IMS RAS). **Acoustic coherence effects on signal processing in shallow water channels.**

This paper presents the results on shallow water acoustic coherence and its effects on large array beamforming and temporal pulsed signal processing. The focus is to incorporate the realistic calculations of the mutual coherence function of space, time, and frequency for comparative analysis of the linear and quadratic signal processors, spatial and temporal ones included. The numerical simulations are carried out for the typical shallow water environments from the Barents Sea where the effects of rough surface scattering and bottom interactions are significant. It is shown distinctly that both the acoustic coherence and sea noise mutually affect the processor performance. It is concluded that the adequate predictions of the signal processing performances are more difficult as compared with the deep water channels and require a much more detailed incorporation of the environmental conditions for a given set of source parameters.

A. V. Lebedev (IAP RAS), B. M. Salin (IAP RAS). **The investigation of acoustic fluctuations in a lake environment.**

This paper is concerned with investigations of acoustic fluctuations in a lake environment. Some peculiarities in the fluctuations which are observed in experiments are discussed.

V. P. Antonov (AKIN), V. V. Borodin (AKIN), G. N. Kuznetsov (Altair),
A. A. Kuz'menko (AKIN), V. P. Tebyakin (AKIN). **Parameter estimation for upper layers of multi-layered bottom in shallow sea.**

This paper contributes to reconstruction of the bottom structure in a shallow sea, that is, to estimation of a number of layers, their thicknesses, and acoustic parameters: sound speed, density, and attenuation.

S. N. Gurbatov (NN University), B. Kerman (Lake Metereology Laboratory AES-CCIW), N. V. Pronchatov-Rubtsov (NN University), O. V. Lebedev (NN University). **Acoustic methods for determining bubble concentrations in subsurface layers.**

The acoustic methods for the distant diagnostics of air bubbles in shallow water is developed in this paper. The features of resonant nature of the (including nonlinear) scattering and absorption of propagating wide frequency band signals in environment with air bubble clouds were used for this aims.

G. M. Glebova (Rostov-na-Donu University), G. N. Kuznetsov (Altair). **Estimating parameters of signal sources and characteristics of noise field by spatially separated vector-scalar modules.**

This paper presents a generalized approach to problems that may be solved with the use of receiving antenna arrays consisting of the vector-scalar modules.

I. P. Smirnov (NN University), J. W. Caruthers (NRL), A. I. Khil'ko (IAP RAS), P. A. Elmore (NRL). **Emission tomography reconstruction of the bubble plumes entrained by breaking wind waves.**

Bubble plumes created near the sea surface in shallow water are anisotropic in three-dimensional space and are temporally variable. In addition, they emit sound in a broad range of frequencies. The applicability of using an inverse method associated with emission tomography for reconstructing the space/time distribution of a bubble plume are investigated. Based on the spatial and temporal characteristics of the sounds they emit, reconstruction of the distribution and evolution of the plumes may be possible using time segments of sound received at separated hydrophone arrays. The necessary space/time apertures for reconstruction are estimated based on the coherence function of the radiated noise. It is shown that random inhomogeneities of the oceanic medium reduce the spatial resolution of the tomographic reconstruction.

Volume 2

I. P. Smirnov (NN University), J. W. Caruthers (NRL), A. I. Khil'ko (IAP RAS). **Bubbles cloud tomographical reconstruction in random inhomogeneous oceanic enviornment.**

The possibilities of estimation of location and spatial parameters of the refractive index local random parturbations by measuring of pulse signals time delays fluctuations are discussed. The mutual coherence function of the received and probing signals for delays is used for tomographical reconstruction procedure. Computer simulations were conducted for realistic scenario in the refractive oceanic waveguide.

V V. Borodin (AKIN), M. Yu. Galaktionov (AKIN). **Fundamentals of the high-frequency forward-scattering sonar.**

The investigation of the efficiency of high-frequency forward-scattering sonar is conducted using an real models refractive oceanic waveguides in present of surface and volume random inhomogeneities.

A. L. Matveyev (IAP RAS), A. G. Sazontov (IAP RAS), N. K. Vdovicheva (IM RAS). **Data analysis of acoustic transmission fluctuations from the Barents sea and its comparison with theory of surface scattering.**

Theoretical predictions of the vertical coherence based on wind seas scattering are compared with the observed spatial coherence of the signals received by vertical arrays operating in realistic shallow water environments. It has been established that vertical coherence function predicted from a wind seas model is in good qualitative agreement with the presented measurements.

B V. Kerzhakov (IAP RAS), V. V. Kulinich (IAP RAS), M. A. Raevskii (IAP RAS), A. A Stromkov (IAP RAS). **Experimental chek of the mode theory of sound scattering in an ocean waveguide with rough surface.**

The prognosis of frequency spectra of the tone signals for an acoustical range in the Okhotsk sea is made in a framework of the mode theory of sound scattering. The results of numerical simulation are compared with experimental data obtained in various seasonal and meteorological conditions. The transformation of energy of modes in a coastal shelf is taken into account in modelling. It is shown that the conclusions of the theory are in reasonable agreement with observations data.